THESIS FOR THE DEGREE OF DOCTOR OF PHILOSOPHY

Advanced EM Modeling and Its Applications

A Journey from BioEM to Surface Electromagnetics for Communication

Morteza Ghaderi Aram

Department of Electrical Engineering
Chalmers University of Technology
Gothenburg, Sweden, 2026

Advanced EM Modeling and Its Applications

A Journey from BioEM to Surface Electromagnetics for Communication

Morteza Ghaderi Aram
ISBN 978-91-8103-407-3

Acknowledgements, dedications, and similar personal statements in this thesis, reflect the author's own views.

Selected material from the author's licentiate thesis: Morteza Ghaderi Aram, "Antenna Design, Radiobiological Modelling, and Non-invasive Monitoring for Microwave Hyperthermia", *Chalmers Reproservice*, Gothenburg, Sweden, Feb. 2022, is republished in this Ph.D. thesis.

Doktorsavhandlingar vid Chalmers tekniska högskola
Ny serie nr 5864
ISSN 0346-718X

Department of Electrical Engineering
Chalmers University of Technology
SE-412 96 Gothenburg, Sweden
Phone: +46 (0)31 772 1000

Cover:
In 6G, reconfigurable intelligent surfaces (RISs) will help transform the wireless environment from something we endure to something we design. Shown on the cover is the concept of non-specular reflection from such an RIS, which was designed to be a holographic-inspired beamforming panel in Chapter 3.

Printed by Chalmers Digital Printing
Gothenburg, Sweden, May 2026

In the Name of Allāh, the Most Gracious, the Most Merciful.

Abstract

Electromagnetics (EM) underpins a broad spectrum of scientific and engineering applications, ranging from life sciences to telecommunications. Centered on advanced EM modeling and its practical use cases, this thesis presents a chronological compilation of the author's contributions across two major domains: Bio-Electromagnetics (BioEM) and surface Electromagnetics (SEM).

The BioEM part focuses on radiative hyperthermia (HT) for head-and-neck cancer treatment. It introduces a new antenna model tailored for hyperthermic applications, followed by the design of an annular phased-array applicator. Building on this hardware foundation, a hybrid beamforming strategy is proposed to accelerate convergence and avoid local minima, together with a versatile thermal solver capable of handling complex anatomical scenarios. These components are integrated into a unified HT treatment-planning workflow aimed at concentrating EM energy within the tumor while minimizing unintended heating of surrounding healthy tissue.

The SEM part of the thesis shifts toward next-generation wireless communications and the emerging role of engineered metasurfaces in shaping the propagation environment. With reconfigurable intelligent surfaces (RIS) gaining traction as a key enabler of 6G technology, there is a growing need for EM-compliant modeling frameworks that remain accurate, efficient, and computationally tractable. To address this, the thesis proposes a hybrid domain decomposition method (H-DDM) for the synthesis and analysis of open-cavity-based RIS beamforming panels. H-DDM is employed to study over-the-air mutual coupling, compared against Macromodeling as a representative surrogate technique from the literature, and benchmarked against commercial full-wave solvers. The promising results highlight H-DDM's potential as a foundation for systematic modeling of emerging holographic beamforming panels and motivate further development of the framework.

Keywords: Electromagnetics, Surface EM, Metasurface, EM-compliant Modeling, BioEM, UWB Antennas, Phased-array Applicator, Holographic MIMO, Wireless Communication.

List of Publications

This thesis is based on the following publications:

[A] **Morteza Ghaderi Aram**, Hadi Aliakbarian, Hana Dobšíček Trefná, "An Ultra-Wideband Compact Design for Hyperthermia: Open Ridged-Waveguide Antenna". Published in IET Microwaves, Antennas & Propagation, Jan. 2022.

[B] **Morteza Ghaderi Aram**, Hadi Aliakbarian, Hana Dobšíček Trefná, "A Phased Array Applicator based on Open Ridged-Waveguide Antenna for Microwave Hyperthermia". Published in Microwave and Optical Technology Letters, Sep. 2021.

[C] **Morteza Ghaderi Aram**, Özlem Tuğfe Demir, Tommy Svensson, Emil Björnson, "Holographic MIMO and Near-Field-Compliant Channel Modeling". Wiley Book Chapter, 2025, in press.

[D] **Morteza Ghaderi Aram**, Fitim Maxharraj, Rob Maaskant, Tommy Svensson, "On RIS Macromodeling of a Large Holographic-Inspired Beamforming Panel". Proc. IEEE 20th European Conference on Antennas and Propagation (EuCAP), 2026.

[E] **Morteza Ghaderi Aram**, Tommy Svensson, Fitim Maxharraj, Rob Maaskant, "DDM-Based Accurate and Efficient RIS Modeling for Over-the-Air Mutual Coupling Analysis and Comparison vs Macromodeling". Invited Paper to a Special Section of the IEEE Open Journal of Antennas and Propagation, 2026.

Other publications by the author, not included in this thesis, are:

[F] B. Elling, **M. G. Aram**, S. LIacer, H. D. Trefná, "The UWB phased array applicator: novel cooling solutions". *33rd Annual Meeting of the European Society for Hyperthermic Oncology (ESHO)*, Warsaw, Poland, May 2019.

[G] **M. G. Aram**, L. Beilina, H. D. Trefná, "Microwave thermometry with potential application in non-invasive monitoring of hyperthermia". *Journal of Inverse and Ill-posed Problems*, De Gruyter, vol. 28, no. 5, pp. 739–750, Oct. 2020.

[H] **M. G. Aram**, M. Zanoli, H. Nordström, I. Toma-Dasu, K. Blomgren, H. D. Trefná, "Radiobiological Evaluation of Combined Gamma Knife Radiosurgery and Hyperthermia for Pediatric Neuro-Oncology". *Cancers*, MDPI, vol. 13, no. 13, pp. 3277, Jun. 2021.

[I] **M. G. Aram**, H. Nordström, I. Toma-Dasu, K. Blomgren, H. D. Trefná, "Radiobiological modeling of hyperthermia combined with Gamma Knife radiosurgery in pediatric brain cancer". *13th International Congress of Hyperthermic Oncology (ICHO)*, Digital, Oct. 2021.

[J] L. Beilina, **M. G. Aram**, E. M. Karchevskii, "An adaptive finite element method for solving 3D electromagnetic volume integral equation with applications in microwave thermometry". *Journal of Computational Physics*, Elsevier, vol. 459, pp. 111122, Jun. 2022.

[K] **M. G. Aram**, H. Guo, M. Yin, T. Svensson, "Site-Specific Outdoor Propagation Assessment and Ray-Tracing Analysis for Wireless Digital Twins". *IEEE 19th European Conference on Antennas and Propagation (EuCAP)*, Stockholm, Sweden, April 2025.

[L] R. Maaskant, D. Lin, F. Maxharraj, **M. G. Aram**, L. Manholm, P. Y. Aghdam, G. Gerini, T. Svensson, M. Ivashina, "Domain Decomposition Analysis of Open-cavity-based Array Elements-Roadmap Toward Analyzing Large-Scale Reflectarrays and Reconfigurable Intelligent Surfaces". *IEEE International Conference on Electromagnetics in Advanced Applications (ICEAA)*, Palermo, Italy, September 2025.

Contents

Acknowledgments

I thank God for showering me with his constant grace and mercy, and I hereby dedicate the work to my parents, Fathhollah and Zahra, and my sister, Fatemeh. This work would not have been possible without the support of many supervisors, mentors, collaborators, and colleagues, to all of whom I extend my heartfelt gratitude. I would like to especially thank Professor Tommy Svensson for his guidance and generosity with the financial support of the study. My deepest appreciation goes to Professor Rob Maaskant for his dedication, his willingness to share knowledge, and the countless enthusiastic discussions that shaped much of this work. Finally, a warm shout-out to all my friends at Chalmers who have been an important part of this journey. I am truly grateful for the moments we shared and the lessons we learned together.

The work was financially supported in part by the Advanced Digitalization program at the WiTECH Centre (DisCourSe & DigiArray projects), and in part by the SNS JU project Hexa-X-II (Grant Agreement No. 101095759) under the EU's Horizon Europe Research and Innovation Programme.

Acronyms

EM:	Electromagnetics
CEM:	Computational Electromagnetics
MTS:	Metasurface
RIS:	Reconfigurable Intelligent Surface
MoM:	Method of Moment
FEM:	Finite Element Method
FDTD:	Finite Difference Time Domain
DDM:	Domain Decomposition Method
PLD:	Power Loss Density

SAR:	Specific Absorption Rate
HT:	Hyperthermia
HTP:	Hyperthermia Treatment Planning
ORWG:	Open Ridged-Waveguide Antenna
CAD:	Computer Aided Design

Part I

Overview

CHAPTER 1

Introduction to EM Application Tracks

The inclusion of a short prelude here is justified by the diversity of the subject areas covered in this thesis. The research track of the thesis targets two application areas: while the first half of the thesis may find readership in the therapeutic branch of biomedical engineering, the second half appeals more to a wider research branch of antenna, propagation, and communication societies. Although the two areas may seem separate at first glance, they both fall under the same big umbrella of electromagnetic research, albeit for different applications. Chronologically speaking, the author's journey started within the biomedical community but over time evolved and morphed more into the Telecommunications society, while keeping electromagnetic research in its core throughout. The order of the upcoming chapters, as well as the included research papers, is to reflect this chronology and the developmental stages of the author's post-graduate journey.

1.1 Introduction

Electromagnetics (EM), which describes the temporal and spatial behaviors of electric and magnetic fields, is a key branch of science and engineering. Char-

acterization and study of all macroscopic EM phenomena are performed based on a unified and fundamental theorem, known as Maxwell's equations [1], [2]. From the temporal viewpoint and based on the fields' oscillation frequency, EM phenomena can be classified into different categories such as direct current (DC), radio frequency (RF), microwaves, terahertz (THz), optics, X-rays, and beyond. From the spatial point of view, the physical dimensions of EM field oscillations can be used as a measure to categorize different electromagnetic phenomena, as depicted in Figure 1.1 [3].

When the spatial variations of an electromagnetic device or phenomenon are much smaller than the wavelength (λ) in all three directions ($L_x, L_y, L_z \ll \lambda$), the behavior falls into what is commonly referred to as a zero dimensional (0D) regime. Within this limit, circuit theory provides an accurate and computationally efficient description, effectively serving as a simplified representation of Maxwell's equations. Electronic circuits in this category are typically modeled using lumped elements—resistors (R), inductors (L), and capacitors (C)—together with lumped voltage and current sources [4]. As the next spatial category, one notices that the transverse dimensions in microwave circuits and optical waveguides are much smaller than the wavelength, whereas the longitudinal dimension is on the order of the wavelength ($L_x, L_y \ll \lambda,\ L_z \sim \lambda$). Systems with this geometric scaling are therefore treated as one dimensional (1D) electromagnetic phenomena. In this regime, conventional circuit theory no longer provides an adequate description, while a full solution of Maxwell's equations is often unnecessarily complicated and computationally demanding. This gap motivated the development of transmission line theory—now a cornerstone of microwave engineering—which offers an efficient and accurate framework for analyzing such structures [5]. Within this theory, the characteristic impedance (Z_0) and the propagation constant (β) serve as the key parameters governing 1D electromagnetic behavior.

Over the years, general electromagnetic theory, depicted as the fourth class in the figure, has been developed to address 3D cases where the spatial field variations become comparable to the wavelength in all three directions ($L_x, L_y, L_z \sim \lambda$). Because of their complexity, analytical solutions are available only for a limited set of canonical geometries in this category. Nevertheless, with the continual improvement of computational resources, it has become feasible to solve Maxwell's equations numerically [6] for complex media characterized by (ε, μ), arbitrary geometries, and diverse boundary con-

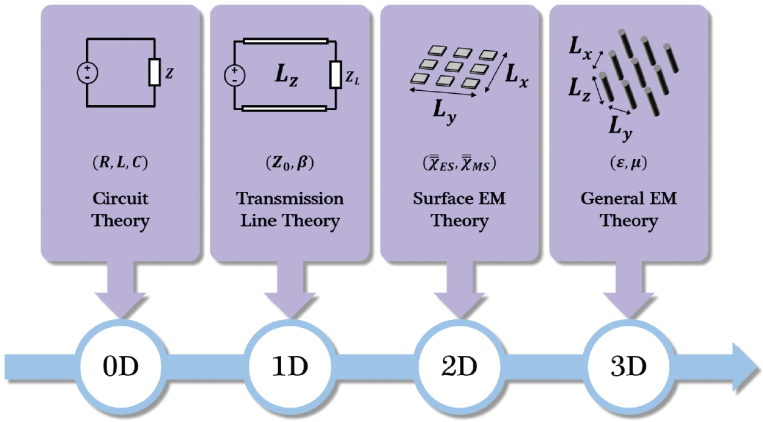

Figure 1.1: Spatial domain classification of EM phenomena based on their electric sizes (taken and reprinted from [3]).

ditions. On the other hand, surface electromagnetic theory—concerned with 2D EM behavior ($L_x, L_y \sim \lambda,\ L_z \ll \lambda$) in Figure 1.1—is still far from fully mature because (a) a general framework for defining the eigen-parameters of arbitrary surfaces remains to be established and (b) simplified theorems from Maxwell's equations still need to be derived for this category.

Electromagnetics underpins a wide spectrum of modern engineering technologies, spanning fields from telecommunications to the life sciences. Within this broad landscape, the main theme of this thesis revolves around two EM application areas, namely Bio-Electromagnetics (BioEM) and surface Electromagnetics (SEM). Temporally speaking, both applications are examined here within the microwave frequency range. However, spatially, they are not in the same category, with the former belonging to a three dimensional (3D) family of EM problems while the latter falls more into the two dimensional (2D) spatial category. With this brief introduction in place, let us now turn to a closer examination of these two key application areas.

1.2 Application Track I: BioEM

Cancer, the uncontrolled growth of abnormal cells in the body, is among the leading causes of death worldwide [7]. Cancers have been classified into

100 different types depending on the type of primary cell from which the uncontrolled growth starts. The cancerous cells can move and form malignant tumors which, if not diagnosed and treated timely, can further spread to other parts of the body through a process known as metastasis. This stage of the disease may lead to a serious and life-threatening condition [8].

Surgery, radiotherapy, and chemotherapy are the standard cancer treatment modalities that can be used alone or in combination with adjuvant methods. Tumor site and stage are the deciding factors in choosing the appropriate type of therapy. Surgery is the longest-standing therapy for cancer but cannot be performed for non-resectable tumors. Moreover, since the simple excision of tumors in some patients is not sufficient to prevent a relapse, surgery usually needs to be accompanied by other modalities to improve the tumor control probability. For radiotherapy (RT), there are limitations regarding the dose tolerance of critical organs. In many cases and particularly in recurrent tumors, these limitations on the admissible level of the dose can make RT treatments ineffective. RT can further lead to late complications and an increased risk of developing secondary cancers. Utilizing one or more anti-cancer drugs, chemotherapy (CT) may eradicate cancer, but its efficacy varies largely depending on the type and stage of the cancer. CT exhibits its best performance if administered in the early stage of the disease when the metastasis is undetectable [9].

Human Head Cancers

Human head cancers, usually classified separately into Head&Neck (H&N) and brain cancers, are one of the most common cancer categories worldwide [10]. Global incidence of H&N cancers, occurring in regions shown in Figure 1.2, has been estimated to be between 400 000 and 600 000 new cases each year, resulting in a mortality rate of between 223 000 and 300 000 deaths per year [11], [12]. Unfortunately, the number of patients dying from cancers in the regions of body reported in Table 1.1 is increasing each year. The table shows the cancer statistics in human head both globally and in Sweden while Figure 1.3 visualizes the percentage of each type of head cancer in 2020 [13]. The situation nationwide in Sweden is similar to the global cancer figures and according to the Swedish Head and Neck Cancer Register (SweHNCR), H&N cancer in Sweden constitutes 2.3% of all cancer incidences, comprising nine different sites reported in the table.

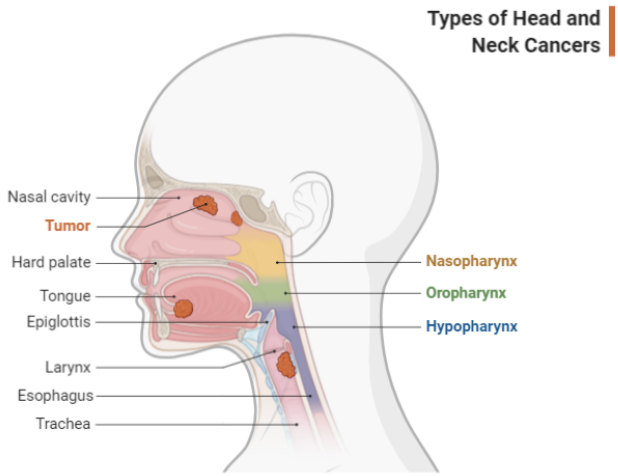

Figure 1.2: Head and neck cancer sites.

Table 1.1: Incidence, Mortality, and Prevalence by cancer site in the head for all ages (Extracted from Globocan 2020 [14])

Cancer Sites	Worldwide			In Sweden		
	Number of New Cases	Number of Death	5-year prevalence	Number of New Cases	Number of Death	5-year prevalence
Esophagus	604 100	544 076	666 388	589	545	721
Thyroid	586 202	43 646	1 984 927	747	78	2 922
Lip, Oral Cavity	377 713	177 757	959 248	687	231	2 279
Brain, CNS	308 102	251 329	837 152	841	752	2 595
Larynx	184 615	99 840	518 380	154	64	561
Nasopharynx	133 354	80 008	382 507	31	7	113
Oropharynx	98 412	48 143	258 543	445	77	1 412
Hypopharynx	84 254	38 599	132 717	54	41	114
Salivary Glands	53 583	22 778	160 292	118	47	427
All Sites	2 430 335	1 306 176	–	3 666	1 842	–

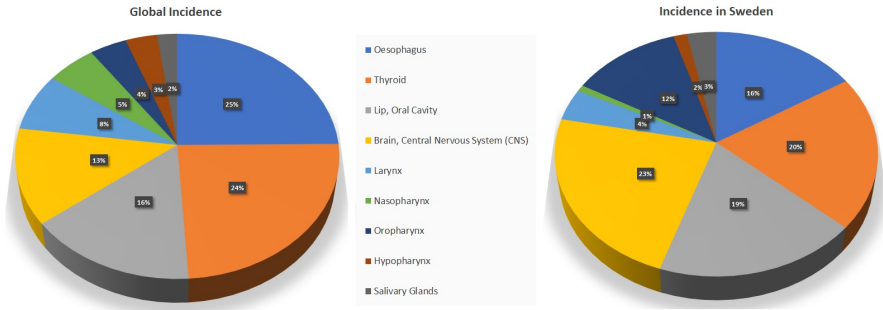

Figure 1.3: Incidence rate percentage of each type of cancer in human head based on Globocan Statistics in 2020.

During the ten-year period of 2008-2017, SweHNCR reports 25% increase in the incidence of H&N cancer in Sweden by summarizing the number of cancer cases per diagnosis group in Figure 1.4. The relative 5-year survival rate for all patients with H&N cancer in the SweHNCR has been reported to be 67%, while the overall survival rate was 59% [15]. As can be seen from Figure 1.5, there are large differences in the relative survival rates between the different diagnosis groups, with hypopharyngeal patients having the lowest relative survival rate of 25%. Except lip patients, all the other categories have an average survival rate between 50 to 75%.

Despite all the advancements in the treatment of cancers in general, brain cancer management still remains challenging with a low chance of long-term survival. In many cases, Glioblastoma multiforme (GBM) is the most aggressive malignant type in adults with the tendency of a quick relapse after surgery. The average survival for patients with malignant gliomas is only 17 weeks which can be extended to 30 weeks after surgery and chemotherapy [16]. In children younger than 15 years old, brain tumors are the second most common cancer type, representing $20 - 30\%$ of all childhood cancers. Medulloblastoma is the most common type in children for which treatments usually begin with surgical excision, followed by the addition of radiotherapy or chemotherapy to increase the disease-free survival rate. For these patients, overall survival reported in population-based studies [17] is roughly 50% to 60%. However, radiation often triggers late complications and severe side effects which is more consequential in children since even low doses of ionizing

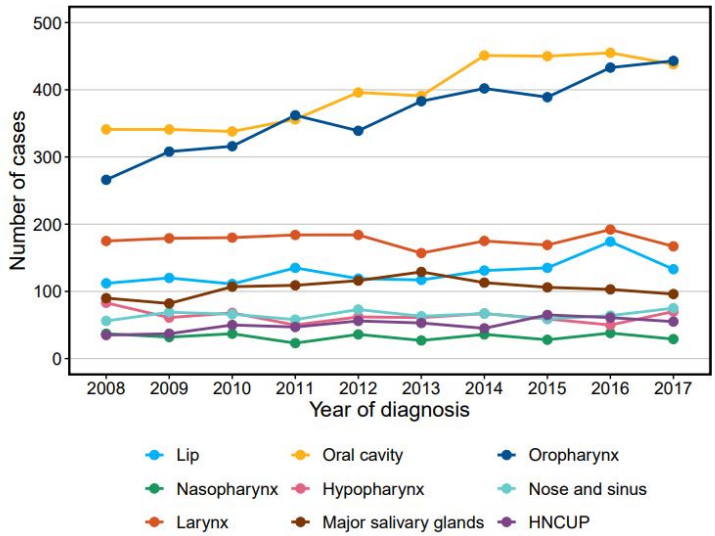

Figure 1.4: Number of cancer cases per diagnosis group during the years 2008-2017 in Sweden [15]

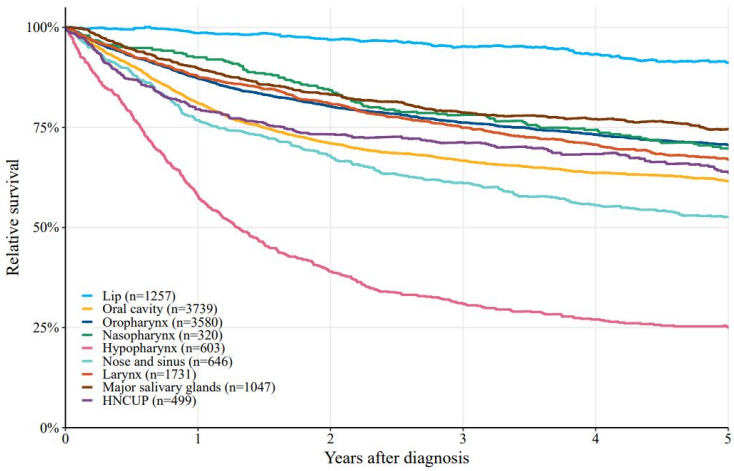

Figure 1.5: Five-year relative survival rates per diagnosis group in the SweHNCR, 2008-2017 [15]

radiation to their brain can cause perturbed growth/ puberty [18], [19] as well as intellectual impairment [20].

Hyperthermia

Hyperthermia (HT) is a therapeutic modality that can be part of a multimodal oncological strategy when combined with radio- or chemotherapy. The aim of HT is to raise tumor temperature to supraphysiological levels between 40°C and 44°C. Studies show that the mild increase in temperature enhances the concentration of oxygen in the tumor, therefore improving the effectiveness of radiotherapy [21], [22]. It also increases the blood flow in the heated area leading to increased perfusion which improves the drug absorption in cells for chemotherapy [23], [24].

The biological rationale for the use of hyperthermia is not completely understood. However, the proven mechanisms, as summarized in [25], include the inhibition of different DNA repair processes, direct/ indirect reduction of the hypoxic tumor cell fraction, increased perfusion and oxygen levels, and enhanced drug uptake. The clinically observed biological effects over HT temperature range are the following [26]. During HT, blood flow is increased by the tissue metabolism to counteract the temperature rise. When heated, the blood vessels in healthy tissues can vasodilate, to facilitate an increased blood flow. This process acts as a heat sink and reduces the temperature. In contrast to healthy tissues, tumorous tissues are far less capable of increasing the blood flow due to a chaotic vasculature which gives rise to regions suffering from improper perfusion and hypoxia. Therefore, the heat dissipation is slower in tumors, and during HT heating their temperature tends to rise higher than that of the normal tissue.

The addition of hyperthermia to the routine cancer therapies increases the tumor response rate by typically about 20% [27]. This happens while the radiation- or chemotherapy-related toxicity to the healthy tissue is not intensified because the effect of HT will be tumor-selective when heat delivery is confined to the tumor site [28]. Therefore, for the same therapeutic outcome without any reduction of the effect on the tumor, HT allows for a lower radio or cytotoxic dose which will eventually result in a lower risk of treatment-related side effects. For primary tumors, HT can be added to the full dose radiotherapy or chemotherapy treatment scheme to enhance tumor management. Efficacy of the method has been demonstrated through randomized trials for

cervical, bladder, and H&N cancers as well as for soft tissue sarcomas [29], [30], [31]. In case of recurrence of a tumor after previous treatments where a higher risk of side effects is associated with re-treatments, the addition of HT can result in a good tumor control allowing for a lower level of dose with a minimal risk of side effects. Low dose re-irradiation combined with HT is a proven treatment method for recurrent breast cancer and recurrent malignant melanoma [32], [33].

Electromagnetic (EM) radiation at either radiofrequency (RF) or microwave frequencies (MW) [34], [35] and the mechanical energy in form of ultrasound (US) [36], [37] are widely used in deep HT systems. Chapter 2 of this thesis focuses on microwave hyperthermia, while the readers interested in US-based systems may consult the relevant literature [38].

1.3 Application Track II: SEM

The second application area of the thesis revolves around surface Electromagnetics (SEM) which is an EM sub-discipline with plenty of specialized and exciting research initiatives yet to be explored. Leaky wave antennas [39], transmitarrays [40], orbital angular momentum (OAM) beam generation [41], and mantel cloaking [42] are but a handful of examples of a plethora of SEM applications, spanning widely from microwave to terahertz to optical spectra.

Historically speaking, though, SEM is not a brand new topic. Instead, it has a rich history of fascinating discoveries dating back to as early as the sixteenth century as portrayed in Figure 1.6. Explaining the bend of light at the interface between air and water, SEM starts with uniform surfaces, and a milestone here is Snell's law, whose simple yet elegant mathematical formula has provided a sound and pragmatic foundation for many subsequent discoveries such as the critical angle for total reflection as well as Brewster's angle for total transmission. For instance, optical fibers, a key component of today's telecommunication infrastructure, are built based on the concept of total reflection. On the other hand, recent discoveries such as anomalous reflection and refraction [43] attest to the fact that SEM is far from being mature and is still an exciting frontier full of new breakthroughs and directions to be explored.

The demand for periodic surfaces originated in the 1950's when the invention of frequency selective surfaces (FSS) [44], also known as optical grating

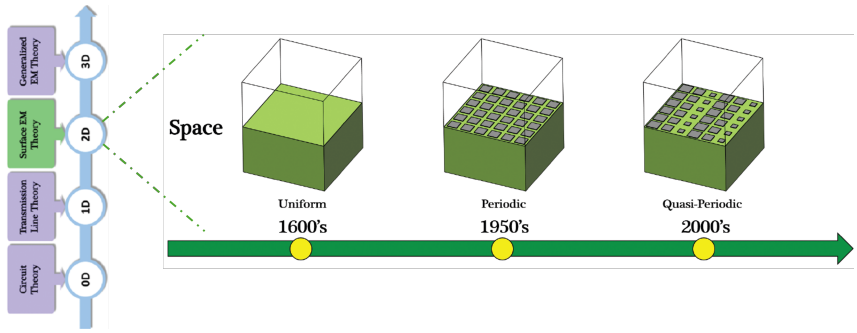

Figure 1.6: Chronological evolution of surface electromagnetics: from uniform surfaces to periodic and then quasi-periodic surfaces (taken and reprinted from [3]).

in the optics community, brought about a giant leap in SEM research. Known as spatial filters, FSSs are analogous to an LC filter from the circuit point of view, but with the distinction that instead of dealing with voltages and currents, FSSs essentially deal with plane waves where the field viewpoints also start to become important in analyzing such design parameters as angular stability and co-polarization purity. Intensive research on FSSs, especially their utilization in stealth technology and radar-centric equipment, eventually paved the way for the introduction of various periodic surfaces with exciting features such as soft/hard surfaces [45], artificial magnetic conductors (AMC), and electromagnetic band gap (EBG) structures [46]. Focusing mainly on the resonant curve of the transmission or reflection magnitude, early studies on FSSs motivated the research community to look not only at the amplitude but also to consider the phase response of a surface where the notion of having an artificial surface engineered with a reflection coefficient response opposite to that of PEC (i.e. $\Gamma = +1$) eventually led to the introduction of AMC. Through lifting the limit of plane wave illumination as had been the primary source of excitation in early FSS studies, further investigations later on utilized surface wave propagation to study the dispersion diagrams of soft/hard surfaces, as well as high impedance surfaces. Along this long continuum of SEM research on periodic structures stands the notion of EBG, which resembles the concept and terminology of energy band gap in semiconductors, and has been indeed another important breakthrough that enables one to engineer

the dispersion diagram of a surface so that no surface wave regardless of its direction can propagate along the surface thereby exhibiting a distinct band gap for all propagation modes in all directions.

As shown in Figure 1.6, it was not, however, until the change of the millennium at around 2000 that a new tide for quasi-periodic surfaces arrived and pushed the SEM research into a new era full of great challenges and novel opportunities. In fact, what turns a collection of elements arranged in a periodic lattice into a quasi-periodic structure is but small geometrical variations in, for instance, scatterers' size or orientation angle. Although these slight spatial modulations in quasi-periodic arrangements might have seemed inconsequential at first, they proved to have far-reaching impacts on the response of this family by allowing for anomalous EM wave reflection or refraction to arbitrary angles which in the end took the Snell's law to a whole lot new level coined as generalized law of reflection and refraction as will be the subject of further discussion in Section 3.5. Reflectarray (RA) [47] and transmitarray (TA) [40] antennas are the most prominent examples of early developments of quasi-periodic structures in this family.

Over the past couple of decades, parallel developments on chiral and bi-media, as well as the surge of interest in composite materials with exotic EM properties not typically found in nature, have given birth to an active field of research widely known as metamaterials (MTM) [48]. Metasurfaces (MTS), which are the 2D counterparts of MTMs, are at the heart of modern SEM research. While the focus of the metamaterial community is mostly drawn towards the constitutive relations, namely the macroscopic tensorial form of permittivity and permeability of bulk 3D composite materials, the metasurface community of SEM mainly focuses on the study of boundary conditions, as will be further elaborated upon in Chapter 3 of the thesis.

In recent years, the fields of MTMs and MTSs have witnessed remarkable growth and advancements among which reconfigurable/tunable meta-devices stand out for their dynamic nature and their ability to revolutionize various applications across the EM spectrum and beyond. To gain insights into how this active area of research has evolved over time, relevant publication trends and statistics were extracted from the Web of Science database[1] and reported in Figure 1.7. To this end, an advanced search in the database on published articles between 2006 and 2025 was conducted to identify the number of indexed

[1] https://www.webofscience.com

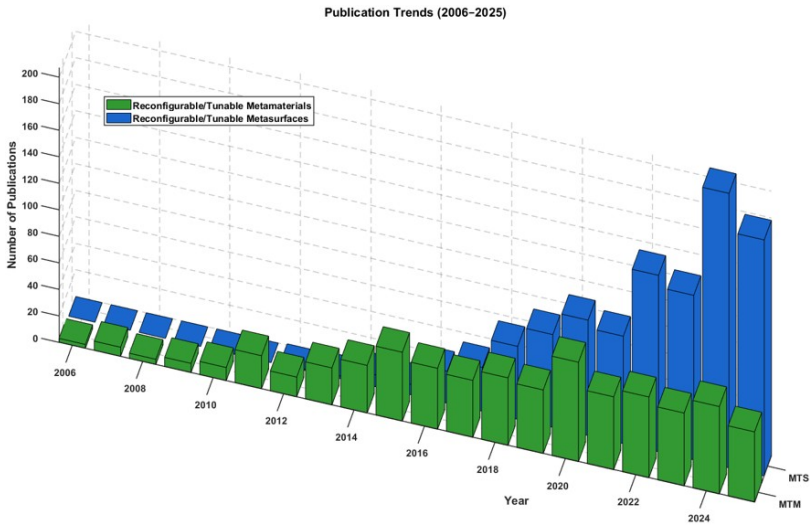

(a)

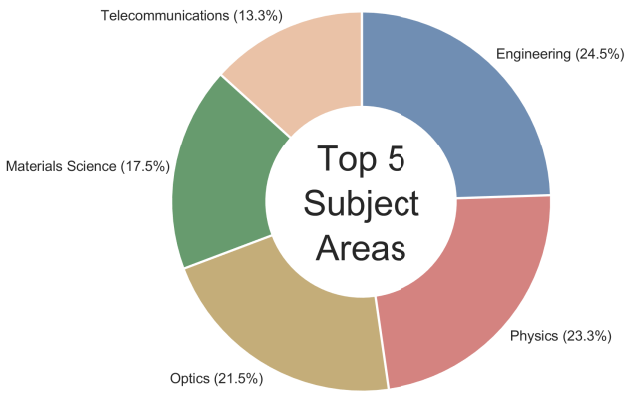

(b)

Figure 1.7: Publication numbers and trends in reconfigurable metamaterials and/or reconfigurable metasurfaces over a 20-year period extracted from Web of Science.

publications mentioning "reconfigurable/tunable metamaterials" or "reconfigurable/tunable metasurfaces" in their titles, abstracts, and/or full-text. As the two bar charts of Figure 1.7(a) reveal, both aforementioned categories have witnessed a tangible growth over the recent years. Interestingly, reconfigurable MTSs have overtaken their bulk 3D counterparts, most likely thanks to their low-profile structural texture and lower dissipation losses at resonance. When it comes to application areas, Figure 1.7(b) shows the top 5 engineering and/or science disciplines benefiting most from these tunable meta-devices. As can be seen from this Pie chart, Telecommunications, which is also the target application area of the SEM research in this thesis, is among the trending subject areas utilizing the concept of reconfigurable metasurfaces.

EM-compliant Communication Systems

Since the Telecom sector is the targeted application market for the SEM research of this thesis, it may prove beneficial at this stage to have a preliminary look at the role SEM plays in today's state-of-the-art wireless communication as follows. Three key technologies have driven 5G performance gains: massive MIMO (mMIMO), which deploys base stations with very large antenna arrays; millimeter wave (mmWave) communications, which exploit a large amount of unoccupied spectrum resources at mmWave frequencies; and ultra-densification, achieved by densely deploying small cells. 5G and beyond are built around three service pillars—enhanced mobile broadband (eMBB), ultra reliable low latency communications (URLLC), and massive machine-type communications (mMTC)—each targeting distinct requirements: eMBB for high throughput services, URLLC for mission critical, low latency tasks, and mMTC for massive IoT connectivity. The explosive growth in data demand and the emergence of applications with extreme performance needs are pushing networks toward a new generation, 6G. Projections for the 6G era foresee data traffic surpassing 5000 exabytes by 2030, service coverage extending across space, air, ground, and sea to realize an Internet of Everything, and the rise of demanding applications such as holographic communications, tactile/haptic Internet, fully autonomous driving, and precision manufacturing. Under these expectations, 6G aims to deliver deeply immersive experiences, full dimension coverage, ultra low latency, and ultra high reliability, while integrating communications, localization/sensing, control, and computing with native intelligence and built-in security [49].

Despite the clear advances of 5G and the ambitious vision for 6G, practical deployment faces serious challenges. Supporting mMIMO requires many RF chains, which increases power consumption, hardware cost, and integration area—issues that become more acute at higher frequencies and threaten energy efficiency and scalability. Moreover, current mMIMO approaches largely adapt to an uncontrolled wireless environment rather than shaping it. A shift toward a software-programmable, intelligent 6G—where the entire end-to-end system including the propagation environment can be reconfigured—is expected. In this context, metamaterials and metasurfaces, particularly in the form of reconfigurable intelligent surfaces (RIS), offer a promising route to meet 6G's stringent demands. Metasurfaces also provide a practical path toward electromagnetic holography and the holographic MIMO (H-MIMO) concept, which could enable holographic radios with manageable power and fabrication costs. Nevertheless, H-MIMO research is still nascent: its fundamental limits are not yet fully understood, and several critical technical challenges remain to be solved [49].

Engineered metasurfaces in the form of RIS, as will be explained in more details in Chapter 3, can serve as dynamic (tunable) boundary conditions to reshape propagation environments. This evolving paradigm in wireless communication motivates the move beyond Shannon's classical view of the wireless mathematical channel, which treats information theory and EM theory as largely non-overlapping domains. In other words, traditional communication models—mathematical simplifications that ignore near-field interactions and mutual coupling in multi-port networks—have been adequate for conventional transmission scenarios, but they no longer produce reliable results for many of the recently emerging use cases. As a matter of fact, the emergence of the controlled phase-shifting techniques, e.g. RIS and holographic surfaces, necessitates the advancement of wave interaction theories. To this end, electromagnetic signal and information theory (ESIT) has recently been proposed [50] as a unified wave-centric framework that bridges information theory with electromagnetic field interactions. Some critical challenges such as translation of field-based behaviors into information-theoretic metrics and effective management of system-level and regulatory barriers are also discussed in [50]. For more information, interested readers are referred to the IEEE official website of the emerging technology initiatives on ESIT[2] whose opening statement

[2]https://esiteti.committees.comsoc.org/

reads, "The Emerging Technology Initiative (ETI) on Electromagnetic Signal and Information Theory (ESIT) is aimed to foster research and innovation on theories and technologies in which electromagnetic aspects are taken into consideration when designing next-generation communication systems and networks. The aim of ETI-ESIT is therefore to unveil the fundamental limits of communication systems moving from first electromagnetic principles, and to develop electromagnetically consistent communication models, signal processing, and optimization algorithms. ETI-ESIT is inherently interdisciplinary and is intended to glue research efforts across multiple scientific fields, communities and societies, including communication and information theory, signal processing, antennas and propagation, electromagnetics, metamaterials, and optics."

1.4 Thesis Outline

This thesis consists of two main parts: BioEM and SEM. Forming the first part of the thesis, Chapter 2 predominantly considers various aspects of Hyperthermia treatment planning (HTP) in the BioEM application track. After introducing a new antenna model for both superficial and deep HT applications, the chapter investigates the process of applicator selection for the cancers occurring in the human head and neck region. It then focuses on near-field beam shaping and thermal analysis to assess the heating ability of the proposed phased-array system based on HT quality metrics.

Starting with Chapter 3, the second part of the thesis re-orients the discussion towards SEM research on RIS modeling. Chapter 3 first reviews the basics and fundamentals of metasurface modeling, followed by a thorough discussion on RIS beamforming techniques. The chapter concludes by presenting numerical and simulation results of a Varactor-based unit cell (UC) design, supplemented by beamsteering performance predictions of a handful of rectangular panels built upon this UC design. Deepening the SEM discussion, Chapter 4 presents a hybrid analysis technique for open-cavity-based beamforming panels. The chapter sets the stage by reviewing the mathematical framework of the domain decomposition method, introduces a novel hybridization scheme to handle sophisticated UC models, and uses the developed computational platform to analyze over-the-air mutual coupling impacts among the adjacent cells for this specific family of beamforming panels. Fur-

thermore, a representative example in this chapter draws a direct comparison between the pattern prediction capability of the proposed method and that of some well-established methods from the literature reviewed in Chapter 3. Finally, the last two chapters are set to wrap up the thesis by providing a brief summary of the included papers as well as by mentioning some concluding remarks and future study directions.

1.5 Notation

The following should be the standard unified notational math nomenclature throughout the thesis unless otherwise mentioned.

Definition 1: *Regular, plain roman letters and symbols* are to identify *scalar quantities and/or scalar operations* such as V, T, $\nabla^2\bullet$, $\cdots$

Definition 2: *Double-struck font* is used to identify *instantaneous vector field quantities* such as $\mathbb{E}$, $\mathbb{H}$, $\cdots$

Definition 3: *Boldface roman letters and symbols* are used to identify *phasor vector field quantities and/or vector operations* such as $\boldsymbol{E}$, $\boldsymbol{H}$, $\boldsymbol{\nabla}\bullet$, $\boldsymbol{\nabla}\times\bullet$, $\cdots$

Definition 4: *Upright boldface letters* are used to identify *vector/ matrix* representation such as $\mathbf{I}_{N\times 1}$, $\mathbf{Y}_{N\times N}$, $\cdots$

Definition 5: *Script letters* are used to identify *Integro-differential operators* such as $\mathcal{L}$, $\mathcal{K}$.

CHAPTER 2

BioEM: HT Antenna Design & Treatment Planning

This chapter begins by outlining the biological foundations of microwave HT and reviewing the technologies used to implement various HT modalities. It then introduces a UWB, compact, and shielded antenna design developed to meet the practical requirements of modern HT systems. Building upon this design, the chapter next presents a phased-array applicator developed from the proposed antenna model. The chapter concludes with an overview of the simulation tasks typically involved in a Hyperthermia Treatment Planning (HTP) workflow.

2.1 Fundamentals of RF/MW HT

Time-varying electric field $\mathbb{E}$ (V/m) and magnetic intensity $\mathbb{H}$ (A/m) are related to each other and to their sources, charge ϱ (C/m^3) and current density $\mathbb{J}$ (A/m^2), by Maxwell's set of equations [1]. Interaction of EM waves with lossy media such as biological tissues results in the power loss density (PLD) deposition which eventually turns into heat. This section first presents a short overview on EM fields, their propagation, and the power deposition in biological tissues. It then concludes the discussion by reviewing a widely used

thermal model for the heat transfer in perfused tissues.

EM Fields & Electrical Properties

Assuming a sinusoidal time dependency in Maxwell's equations, we can separate the temporal and spatial dependencies to work in the phasor domain as follows:

$$\boldsymbol{\nabla} \times \boldsymbol{E} = -\boldsymbol{M} - j\omega\mu\boldsymbol{H} \tag{2.1}$$
$$\boldsymbol{\nabla} \times \boldsymbol{H} = \boldsymbol{J} + j\omega\varepsilon\boldsymbol{E} \tag{2.2}$$
$$\boldsymbol{\nabla} \cdot \boldsymbol{D} = \varrho \tag{2.3}$$
$$\boldsymbol{\nabla} \cdot \boldsymbol{B} = 0 \tag{2.4}$$

where

$$\mathbb{E}(x, y, z; t) = \mathrm{Re}\{\boldsymbol{E}\ e^{j\omega t}\}$$
$$\mathbb{H}(x, y, z; t) = \mathrm{Re}\{\boldsymbol{H}\ e^{j\omega t}\}$$
$$\mathbb{J}(x, y, z; t) = \mathrm{Re}\{\boldsymbol{J}\ e^{j\omega t}\}$$
$$\boldsymbol{D} = \varepsilon\boldsymbol{E}\ ,\ \boldsymbol{B} = \mu\boldsymbol{H}.$$

Since the interaction between $\boldsymbol{B}$ fields and biological materials through magnetization is insignificant, we can consider only two mechanisms of the interaction with $\boldsymbol{E}$ fields through which currents are produced in tissues. The first mechanism is the drift of free conduction charges in the material in response to the applied $\boldsymbol{E}$ field. This conduction current is $\sigma\boldsymbol{E}$, where σ (S/m) is the conductivity. The second mechanism is dielectric polarization, which may arise when the positive and negative charges of a molecule are displaced slightly from their equilibrium positions due to the applied $\boldsymbol{E}$ field, hence the name displacement current. This effect is taken into account in a dimensionless quantity known as electric susceptibility, χ. Now, it is useful to define the complex permittivity of the material as follows

$$\varepsilon = \varepsilon_0\big(1 + \chi + \frac{\sigma}{j\omega\varepsilon_0}\big) = \varepsilon_0(\varepsilon^{'} - j\varepsilon^{''}). \tag{2.5}$$

The additional polarization charge is accounted for by $\varepsilon^{'}$ whilst the effect of the conduction of free charges is described by $\varepsilon^{''}$. The parameter $\varepsilon^{''}$ determines how much power is absorbed from the electric field. A related parameter

often used in the literature is loss tangent $tan\delta = \frac{\varepsilon^{''}}{\varepsilon^{'}}$. Notice that in biological tissues, both $\varepsilon^{'}$ and $\varepsilon^{''}$ vary with the frequency of the applied field and therefore are considered as dispersive. Debye and Cole-Cole dispersion models that represent the dielectric spectra of tissues are discussed by Gabriel et al. [51].

Power Absorption

The following discussion aims to show how, in the HT context, we derive the amount of power dissipated in a volume V from the amount of power entering that volume enclosed by the surface S. According to Poynting theorem [1], energy exchange in a source-free volume V satisfies the following equilibrium

$$\int_V \boldsymbol{E} \cdot \boldsymbol{J}\ dv = -\frac{d}{dt}\Big(W_E + W_H\Big) - \oint_S \boldsymbol{E} \times \boldsymbol{H} \cdot \boldsymbol{ds}. \tag{2.6}$$

In other words, the rate of energy change in volume V can be determined by the change of electrically (W_E) and magnetically (W_H) stored energy in that volume as well as the amount of energy flux passing through the enclosing surface S of the same volume. Since there are no stored energy in the patients body and in biological tissues in general, the first term in the right-hand side of Equation (2.6) can be safely omitted. From a measurement point of view, time-averaged quantities are more useful than the instantaneous quantities in Equation (2.6), and from phasor domain relations, we know that taking average $< \bullet >_T$ over a time period T of the power quantities results in an expression such as $< \boldsymbol{E} \times \boldsymbol{H} >_T = \frac{1}{2}\mathrm{Re}\{\boldsymbol{E} \times \boldsymbol{H}^*\}$ where $\boldsymbol{H}^*$ is the complex conjugate of $\boldsymbol{H}$. Thus, we get

$$\frac{1}{2}\int_V \mathrm{Re}\{\boldsymbol{E} \cdot \boldsymbol{J}^*\}\ dv = -\frac{1}{2}\oint_S \mathrm{Re}\{\boldsymbol{E} \times \boldsymbol{H}^*\} \cdot ds \tag{2.7}$$

Since $\boldsymbol{J} = \sigma\boldsymbol{E}$, the left-hand side of the Equation (2.7) represents heat-producing Ohmic losses. In mathematical terms, the incremental energy (dW) absorbed by (dissipated in) an elemental volume (dv) is $P = \frac{dW}{dv} = \frac{1}{2}\sigma|\boldsymbol{E}|^2$. Equation (2.7) shows that the time-averaged power dissipated in V is equal to the time-averaged power passing into V through the surface S.

The specific absorption rate (SAR), i.e. mass normalized energy absorption rate, is defined as the time derivative of the incremental energy absorbed by an incremental mass (dm) contained in dv of a given density (ρ) as follows

$$SAR = \frac{d}{dt}\left[\frac{dW}{dm}\right] = \frac{d}{dt}\left[\frac{dW}{\rho dv}\right] = \frac{d}{dt}\left[\frac{1}{\rho}P\right] = \frac{\sigma}{2\rho}|E|^2. \tag{2.8}$$

The unit for SAR is W/kg.

Heat Transfer Model

The deposited EM energy, discussed in the previous section, eventually turns into heat due to Joule heating. A simplified version of the heat equation in homogeneous, non-perfused media is usually used to relate the SAR to incremental change in temperature ($\frac{\Delta T}{\Delta t}$) as follows

$$SAR = c\frac{\Delta T}{\Delta t} \tag{2.9}$$

where c is the heat capacity (J/°C/kg).

Equation (2.9) gives only an estimate of how the temperature may evolve in the tissue during the SAR deposition. Biological models, however, involve perfused tissues due to blood circulation in body, and this fact is not accounted for in this simple formula. The most established way to model this phenomenon while taking into account the blood perfusion rate is by using the Pennes Bioheat equation [52] as follows:

$$c\rho\frac{\partial T}{\partial t} = \boldsymbol{\nabla}\cdot(\kappa\boldsymbol{\nabla}T) + PLD - c_b\omega_b(T - T_b) \tag{2.10}$$

where T (°C) is temperature; ρ (kg/m^3) is mass density; κ (W/°C/m) is thermal conductivity; and T_b, c_b, ω_b (kg/m^3/s) are temperature, heat capacity, and perfusion rate of blood, respectively.

2.2 HT Treatment and Systems

Radiative applicators use EM energy mostly in the RF or microwave range to deliver heat into the target/ body. They can be categorized into two types: internal and external. Internal heating includes interstitial heat delivery through the insertion of tiny antennas into tumor. External heating of deep-seated tumors involves use of a conformal multi-element antenna phased array used to emit microwaves or radiowaves in order to transfer the EM energy into the tissue. External heating techniques require a waterbolus (WB) to be

placed between the applicator and the body. The presence of WB improves the impedance match to the tissue, reduces the level of stray radiation compared with the case of an air gap between applicator and tissue, and provides cooling for the skin and other superficial tissues. WB also spaces the tissue from the relatively rapidly decaying near-field, or in other words, it helps to avoid putting the patient's body in the reactive near-field by setting it instead within or beyond the radiating near-field zone (Fresnel region) [53].

The general configuration of an RF/ microwave HT system is given in Figure 2.1. Four main parts to such a system can be identified from the figure as follows: (1) an antenna applicator which also includes waterbolus and the cooling system (2) a power amplification unit (3) the control and treatment planning unit and (4) a thermometry feedback loop. Only parts one and three will be discussed in the upcoming sections. For a thorough discussion about HT amplifier systems and the hardware design of such systems, interested readers can consult [54], [55]. Thermometry is still accomplished invasively through the insertion of temperature sensors into body. A non-invasive alternative for temperature measurement, not shown in Figure 2.1, is based on proton resonance frequency shift (PRFS) of MRI [38], [56], [57], [58] which can be used to monitor the heating process and to have a closed-loop feedback control with a graphical user interface (GUI) for operator control.

Depending on the target volume, one can consider three distinct categories of HT application [59]: superficial, deep, or whole-body hyperthermia.

Superficial Hyperthermia

Superficial HT applicators are typically used to heat a limited volume of tissue close to the heating device. In general, lower frequencies heat larger and deeper regions in the body while the higher frequencies can provide localized heating of the skin and superficial tissues. Using the frequencies in the range of 400–1000 MHz, superficial heating within 2–4 cm from the skin can be obtained [59]. These heating devices can be based on waveguide/ horn antennas [61], [62] as well as low-profile, printed designs [63] and can be used to heat such superficial tumors as lymph-node metastases of H&N tumors, chest wall recurrence, breast cancer or cutaneous metastases [64]. An example of horn-based applicator, shown in Figure 2.2(a), is the Lucite cone applicator (LCA) working at 433 MHz to treat breast carcinomas, melanoma, and lymph-node metastasis of H&N squamous cell [61], [65]. The conformal microwave array

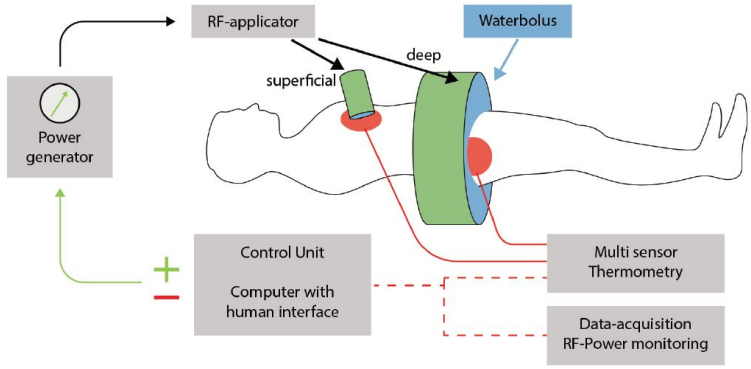

Figure 2.1: Conceptual schema of a typical HT system (Taken and reprinted from [60])

(CMA) [66], shown in Figure 2.2(b), is another example of the superficial applicators of this family that can be put around the torso of the patients and thus are low-profile and wearable. Last but not least, the 434 MHz contact flexible microstrip applicator (CFMA) and the 434 MHz ALBA ON4000 [67], [68] and the 915 MHz BSD-500 [69], [70] are superficial systems which are clinically applied and are routinely used in the treatment of local breast cancer recurrences [71].

Deep Hyperthermia

In deep HT, multi-antenna phased array systems are typically used to treat deep-seated tumors in large parts of the body such as the pelvic region and the limbs. Examples of such systems can be found in [35], [72], [73], [74], [75]. In targets located beyond 2 cm from the skin, the temperature goal is often better achieved with these systems where an array of antennas is placed around the patient [59]. To create a constructive wave interference for selective heating of the target, the antennas need to be suitably fed in amplitude and phase. These steering parameters as well as the operating frequency of the antennas are determined and optimized during the Hyperthermia treatment planning (HTP) stage, as reviewed in [76], [77]. In a phased array system, the operating frequency is a critical parameter because it not only determines the achievable penetration depth of a certain system, but it also controls

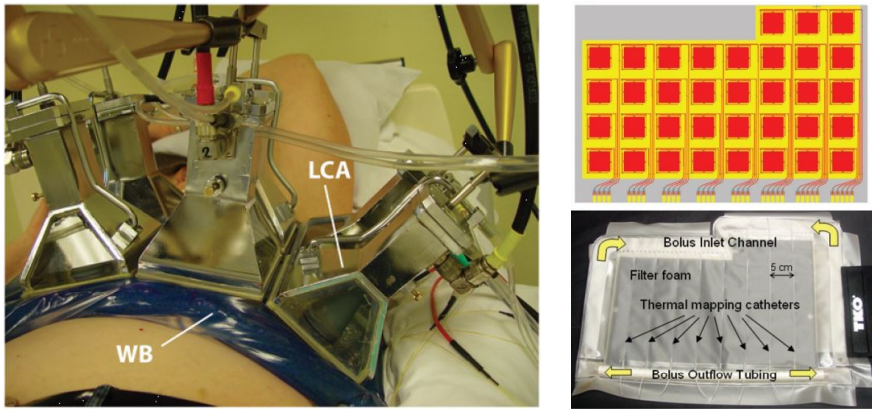

(a) (b)

Figure 2.2: Examples of superficial applicators for local HT (a) A 2×3 Lucite Cone Applicator (LCA) array, reprinted from [62] (b) A 35-element L-shaped CMA array along with its waterbolus coupling layer, reprinted from [66].

the size of the temperature focal spot which is, according to the diffraction limit, roughly around half a wavelength. Having a wide operational frequency band, ultra-wideband (UWB) HT systems offer more degrees of freedom and flexibility.

The typical frequency for cancer treatment in pelvic region ranges from 70 to 200 MHz. Within this band, applicators from BSD 2000 family [1] have been widely used for this purpose. BSD Sigma 60 which is the first of the two types of BSD systems is a cylindrical applicator with a ring of 8 dipole antennas and operates at 77 MHz. The second BSD applicator is Sigma Eye which is an elliptical applicator with 24 dipole antennas operating at 100 MHz.

A higher frequency range, typically above 400 MHz, has been used for hyperthermia in H&N. The group of Erasmus MC was the first to develop a cylindrical applicator HYPERcollar consisting of 12 patch antennas operating at 434 MHz for the treatment of H&N cancers [35], [80]. By proposing a 20-patch-antenna configuration over three rings, the group has recently re-

[1] https://pyrexar.com/hyperthermia/bsd-2000

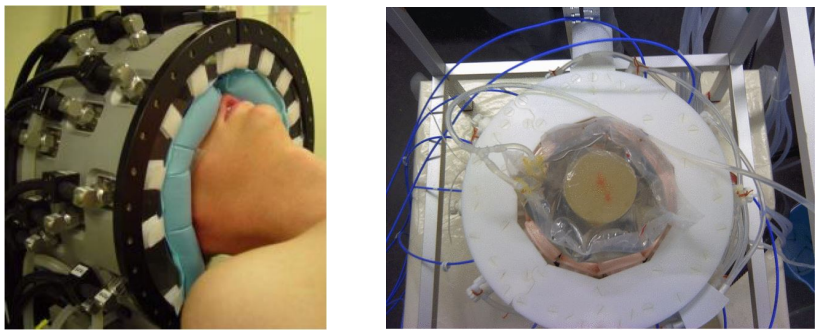

(a) (b)

Figure 2.3: Examples of deep applicators for regional HT (a) HYPERcollar3D developed in Erasmus MC, reprinted from [78] (b) A H&N prototype developed at Chalmers, reprinted from [79].

designed the original applicator and branded it HYPERcollar3D [75], [81] (Figure 2.3(a)). A laboratory prototype for an ultra-wideband H&N applicator has also been developed at Chalmers. The prototype consists of 10 self-grounded bowtie (SGBW) antenna [82] arranged in two interlaced rings in a cylindrical configuration (Figure 2.3(b)).

Whole-body Hyperthermia

Whole-body HT can be used to treat carcinomas with distant metastases where the cancer has expanded from the primary tumor to distant lymph nodes or organs. Soft tissue sarcomas, melanomas, or leukemia are some examples of the cancer types suitable for this type of treatment. Two systems are clinically used for this purpose by employing microwave and infrared radiation with a heating time of 60–90 minutes [64].

2.3 Antenna Design

Antenna design for biomedical applications has been widely pursued by researchers in the field and has attracted attention in the past decades. These applications can be divided into two categories: therapy and diagnostics. In

therapy, antennas have been used mainly for hyperthermia which has a different set of design criteria than those proposed for diagnostic purposes or free-space applications.

The antenna matching impedance in HT depends on the antenna-tissue distance determined by waterbolus dimensions, the human body region, and the patient anatomy [83]. Hence, designing an antenna that can maintain its impedance match over a practical range of distances between the antenna and the human body is a critical step towards building a good clinical HT applicator. Since human bodies with different tissues of variable dielectric properties present a high permittivity complex load to an antenna, the presence of a patient located in the antenna's radiating near-field can detune its resonance frequency, thereby impairing the EM coupling process. Conventional applicators exhibit tissue- and distant-dependent matching performance. Design strategies need to be considered to increase the resilience of the antenna against the detuning effect due to variable tissue-loading conditions. For instance, if the applicator's operational band can be widened, the detuning effect becomes less critical as long as the detuned band still contains the desired resonant frequency feature of the nominal design [83].

In HT, focused induced heating is achieved through having a constructive interference of waves in order to make a focal point on the target. Concentrating the fields amounts to having narrow-beam radiation which requires an electrically large aperture [84]. The effective size of the aperture also plays an important role in determining the EM-field penetration profile into the body. Reflection at the interfaces between different kinds of tissues is another important factor in coupling EM energy into biological systems. The reflection at the interface of two tissues is not merely determined by the specific tissue types, but also by other factors such as the frequency, the polarization, and the angle of incident wave. When there is a large amount of reflection from these tissue interfaces, the interference between the incident and the reflected waves can result in significant standing-wave patterns that may cause excessive heating (hot spots) in certain regions of the body [84]. Ideally, it is recommended for the E-field components to be predominantly tangential to the border of these discontinuities since this will prevent overheating of superficial and interfacing tissues [83].

Aiming to contribute to the ongoing work in this active field of research, this section proposes a UWB, compact, shielded design that is specifically tailored

to meet the requirements of modern HT devices. Furthermore, a phased array applicator based on the proposed antenna model will be presented in the subsequent section.

Design Criteria for HT Antennas

The following criteria need to be satisfied in order to have an efficient antenna design for HT applications.

- Choice of an appropriate frequency band: Biological tissues are a lossy propagation medium for EM waves, and the amount of the loss increases with frequency. On the other hand, higher frequencies give better spatial resolution and thus a smaller focal point. Therefore, when selecting the operation band of HT antennas, a compromise between these two opposing factors is needed. This has led to the selection of the lower part of the UHF band ([300–900] MHz) for hyperthermic purposes.

- An ultra-wideband characteristic: UWB antennas are highly desirable for HT applications. This allows for frequency hopping to control the size of the focal point and hence to adjust it to the size of the tumors under treatment.

- A directional radiation pattern with low side-lobe levels: This provides more efficient power deposition in the patient body and also a lower level of mutual coupling and cross-talk between adjacent elements of the array.

- Size and isolation: The design should be compact and shielded from the EMC point of view.

In the literature, a variety of antenna types for high power applications of deep hyperthermia have been proposed so far [82], [85], [86], [87]. Applicators based on dipole [88], [89], waveguide [72], [90], and microstrip patch [35] antennas, for instance, have been in clinical use in the treatment of cervical and H&N cancer patients. While efficient, these designs are inherently narrowband, with a fractional bandwidth no more than 5–10%. In an attempt to overcome the bandwidth limitation of the previous designs and to achieve a UWB design for H&N region, Takook et al. [82] tailored the self-grounded

bow-tie (SGBW) design of [91] to suit the hyperthermic condition. However, to obtain a symmetric radiation field and stable electrical performance, bow-tie designs require a balun [92] which will also act as an RF-matching network. This matching network absorbs a substantial amount of power and thus decreases the efficiency of these designs [85]. Therefore, in terms of reliability and reproducibility, antennas in which an RF matching network can be avoided have a clear advantage in clinical settings [85].

The type of antenna used in an HT applicator also determines how the energy is distributed in the treated area. Many applicators are based on waveguides (WG) [72], [90] which have one of their sides closed and operate in a TE mode on the other side with an open rectangular cross-section. These hollow WGs are usually filled with distilled water and are excited by means of a short extension of loop antennas or coaxial probes [93]. The radiation resistance of the probe or loop can be made equal to the characteristic impedance of the coaxial feedline by choosing the dimensions of the coupling antenna and its position with respect to the closed end of the applicator. Compared to rectangular WGs of the same dimensions, ridged waveguides (i.e. waveguides with a ridged cross-section) have a lower cut-off frequency, a lower characteristic impedance, and a wider frequency band free from higher-order-mode interference [94], [95], [96]. On the other hand, the horn-based applicators [61], which can also be considered as a variant of WG applicators by utilizing a flared opening, produce more uniform temperature fields than classical waveguides [60]. To take advantage of the positive features of both ridged waveguides and horn antennas, this study proposes a new design by combining the two approaches and calls it open ridged-waveguide (ORWG) as follows.

The ORWG Model

Aiming for a UWB antenna suitable for both deep and superficial HT, *Paper A* proposes the design of an ORWG antenna for HT applicators. ORWG takes advantage of positive features of double-ridged horn (DRH) antennas thus offering a wide band of operation. By avoiding use of a balun or RF-matching network, it avoids the problem associated with the SGBW antenna. Moreover, it is less susceptible to the cross-talks among adjacent elements as well as environmental noise and interference in general because it is inherently shielded by its metallic housing. This makes the design also appealing for

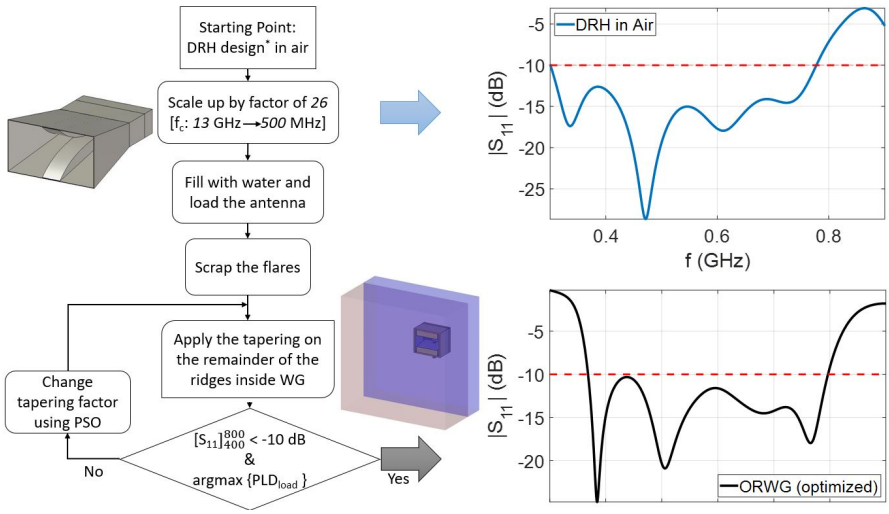

Figure 2.4: Summary of the design and optimization process of the ORWG antenna (* Original DRH from the design proposed by Mallahzadeh et al. [98])

diagnostic purposes like microwave imaging [97].

All the details and steps taken in the design procedure of ORWG are given in *Paper A* and therefore are not repeated here. In summary, a well-established DRH design for radar and EMC applications in the X and Ku bands [98] was scaled, filled with water, and loaded with a flat WB and muscle phantom according to the hyperthermic assurance guidelines [99], [100]. To avoid power losses in the water inside the structure and to help make the design more compact, the flaring parts were scrapped and the built-in PSO optimizer of CST[2] was used to fine-tune the parameters of the model. The PSO algorithm was set for a multi-objective optimization to yield a return loss better than -10 dB in the range of [400–800] MHz as well as to maximize PLD in the target tissue, i.e. muscle in this case. Figure 2.4 gives a concise summary of the design optimization workflow and the final result.

CST MW Studio 2019 provides power budget analysis whose calculation is depicted in Figure 2.5. Analysis of different power components, labeled in Figure 2.5, reveals interesting features of the optimized antenna in front of a

[2] www.cst.com

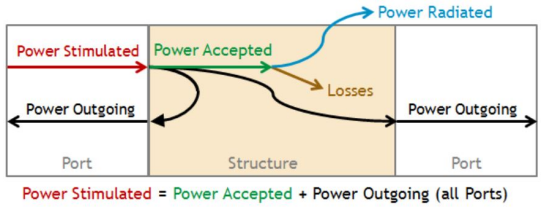

Figure 2.5: The power that is *stimulated* at one or more ports will be divided into the power which is *accepted* by the structure and the power which is again leaving the structure via the ports (*outgoing power*).Furthermore, the accepted power is converted either into *losses* (losses in dielectrics or metals) and/or is *radiated*.

flat WB and muscle phantom. It shows how much power is deposited in the phantom and where undesirable power losses occur. Figure 2.6(a) shows that when excited with a normalized power of 0.5 W within the desired frequency band, the antenna accepts almost all the incoming power (the blue curve) and there is a small portion of the power outgoing as the return loss (the orange curve). It is also shown that almost all the accepted power has been deposited in the dielectric materials (the red curve) with a very small amount of stray radiation outside the region of interest (the magenta curve). In this scenario, we have two dielectric materials, i.e. water and muscle. To get a better picture of how much power was successfully delivered to the target volume (muscle in this case), one can separate the volume losses in these two materials as reported in Figure 2.6(b). As can be seen, the power dissipation in water becomes larger at higher frequencies. This was expectable from the Debye model used for water in the CST simulation.

Hydrogel Bolus and Phantom Preparation

As discussed in Section 2.2, waterbolus is an inseparable part of today's HT systems and plays an important role in the heating pattern of the antennas. A good WB design allows for easy positioning of the applicator around the patient, has a high level of shape predictability which is a crucial factor affecting the treatment planning performance, and is elastic enough to conform to skin contours. To form a WB, the water is typically circulated within plastic bags. Hydrogel bolus [101] has similar dielectric properties to water and is a

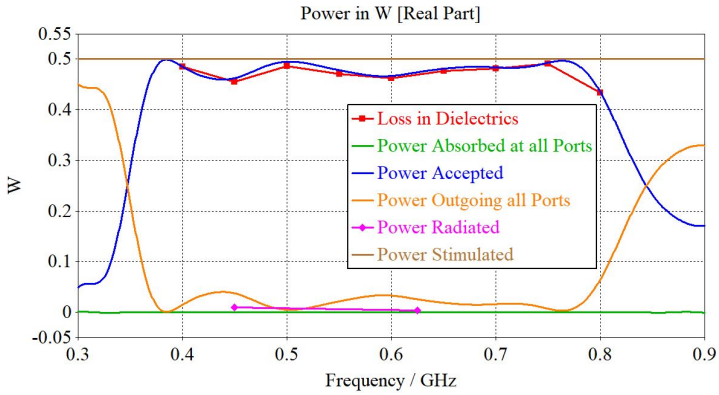

(a)

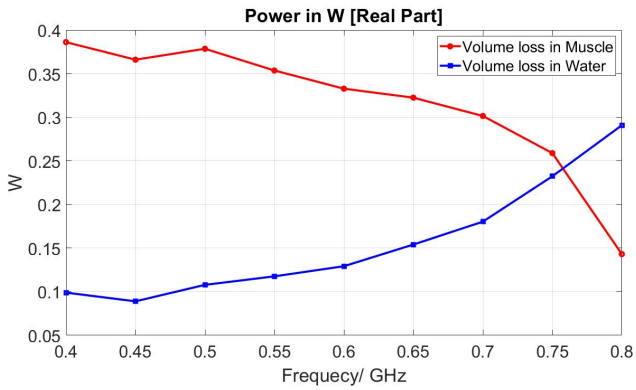

(b)

Figure 2.6: Power balance for the ORWG simulation in CST (a) All the incoming and outgoing powers along with the volume losses (b) Volume losses in each dielectric material separately.

very convenient replacement for a water-filled, plastic bag bolus. It has also been shown to provide a better enclosure between the antenna and the body [101].

The hydrogel is made of 99% deionized water and 1% polymer of which 35% is LBG, another 35% is Xanthan, and the remainder 30% is Agar. The recipe

Table 2.1: List of the ingredients used to make 3 liters of hydrogel and muscle phantom in the lab.

Ingredients	Mili-Q water (ml)	LBG (g)	Xanthan (g)	Sugar (g)	Salt (g)	Agar (g)
Hydrogel	2970	10.5	10.5	–	–	9
Muscle Phantom	2100	–	–	1665	42	66

and the list of ingredients for approximately 3 liters of hydrogel and muscle phantom are reported in Table 2.1. Dielectric properties of the hydrogel and phantom were measured with an open-ended coaxial dielectric probe (85070E, dielectric probe kit with performance probe, Agilent Technologies, USA) connected to a vector network analyzer (VNA) (E8362B, Agilent Technologies, USA). Their relative permittivities are quite constant throughout the band and they read as 78 and 60 for hydrogel and muscle phantom, respectively. Their conductivities, however, slightly change within the band and they were recorded in the range of [0.3–0.6] and [0.4–1.1], respectively.

Measurement & Verification

Far-field radiation pattern, gain, and efficiency are the design characteristics and conventional verification procedures widely used in the antenna and propagation society. Unfortunately, these metrics are not directly applicable to HT scenarios due to the propagation in lossy media [102], [103]. However, other criteria defined by the HT guidelines have been proposed as viable measures for antennas' efficacy for this specific application. Since the final goal in HT is to produce a temperature gradient between the tumor and the rest of the body by raising tumor's temperature, it seems quite natural and intuitive to have a criterion to assess the capability of different antenna designs in terms of temperature rise. To this end, Equation (2.9) is usually used to relate the specific absorption rate to incremental change in temperature. According to [104], an efficient heating device for superficial HT should be able to increase the tumor temperature at a rate of 1°C per minute. Considering a typical heat capacity of muscle tissues to be around 3600, this criterion corresponds to the SAR deposition of at least 60 (W/kg). To assess if this condition was met by the ORWG design, the setup shown in Figures 2.7(a) and 2.7(b) was used in the lab. For the input power of 25 W fed to the antenna for 6 minutes,

the temperature was monitored at different locations by fibre optic probes[3] located in the phantom according to Figure 2.7(a). Figure 2.7(c) shows the recorded temperature by the probes during the exposure and indicates that the design certainly meets this criterion.

Another criterion to appraise the efficacy of the antennas designed for HT applicators is the effective field size (EFS). The EFS is defined by the area within the 50% of maximum SAR contour in the 1 cm deep plane under the aperture. According to the guidelines, a good radiator for superficial HT needs to have an EFS greater or at least equal to its physical aperture size so that side-by-side elements in an array configuration leave no area of tissue surface uncovered. To assess the EFS experimentally, the muscle phantom was pre-cut 1 cm below its surface, and after exposure, temperature profiles were captured by an infrared camera[4] at two different frequencies as reported in Figures 2.7(d) and 2.7(e). As can be seen, the performance of the antenna at 800 MHz is not as good as at 600 MHz and this was expected because 800 MHz is at the far end of the design's operational bandwidth where the penetration depth also starts to decline. All in all, this criterion has also been successfully met by the design (see *Paper A* for more details).

2.4 Phased Array Applicator

Annular phased arrays (APA) are the most common type of applicators used for treating deep-seated tumors in regional hyperthermia. They typically have their elements arranged in a circular or elliptical configuration around the patient's body. When it comes to selection of the right antenna design for an APA system, the impedance bandwidth is not the only deciding factor; certain minimum requirements regarding energy distribution need to be met for an applicator to be suitable for deep HT trials. The average power absorption (aPA) ratio has therefore been defined to quantify the relative amount of energy deposited in the tumor. If N_T and N_H are the total number of voxels in the tumorous volume (V_T) and healthy volume (V_H), respectively, then aPA is defined as

[3]FISO Technologies, Quebec, Canada
[4]B355, FLIR Systems, USA

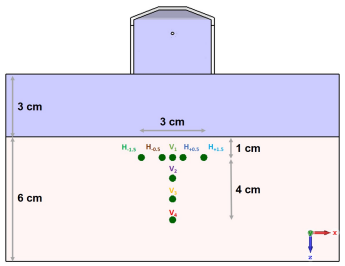

(a)

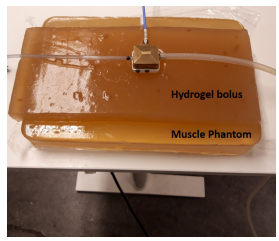

(b)

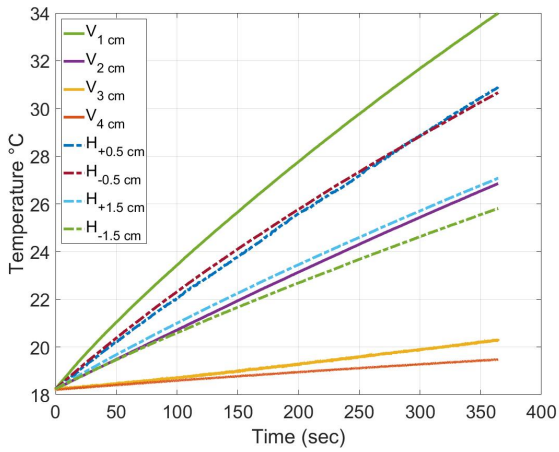

(c)

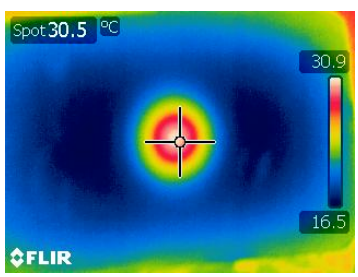

(d)

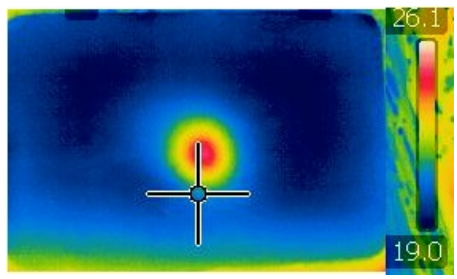

(e)

Figure 2.7: The setup used in the verification procedures (a) Schematic illustration (b) Its photograph (c) Rate of temperature change recorded by the fiber optic probes within 6 minutes of exposure at 600 MH. (d) and (e) IR-camera temperature profiles 1 cm below the surface of the muscle phantom at 600 and 800 MHz, respectively.

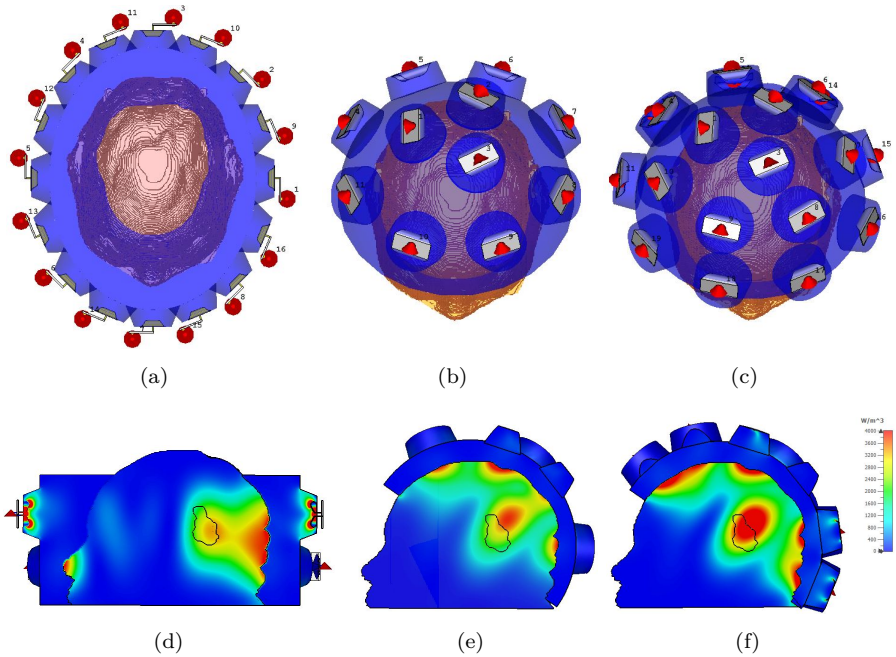

Figure 2.8: Simulation setups (1^{st} row) and PLD distributions (2^{nd} row) for the head phantom model. (a), (b), and (c) are top views of 16-element elliptical, 11-element helmet-based, and 19-element helmet-based arrangements for the antennas, respectively. (d), (e), and (f) are the corresponding PLD distributions at 450 MHz in the sagittal plane.

$$aPA = \frac{\frac{1}{N_T} \times \text{Total power absorbed in the tumor}}{\frac{1}{N_H} \times \text{Total power absorbed in the healthy tissue}} = \frac{N_H \sum^{V_T} PLD}{N_T \sum^{V_H} PLD}. \tag{2.11}$$

For an applicator to be deemed capable of deep heating, aPA must be greater than 1.5 [53].

Since the aim was to come up with an applicator design that would suit as many cancer cases in the human head as possible, an investigation on the op-

timal design for such a one-size-fits-all applicator had been performed. To this end, an anthropomorphic head phantom consisting of two regions of tumorous and average healthy brain tissues was used to evaluate the performance of three different applicators as depicted in Figure 2.8. Their performances in terms of aPA are compared in Table 2.2 which also reports the amount of the power deposited in the target and healthy tissues.

The first configuration was an elliptical annular applicator of 16 elements arranged in two rings. Some parametric studies on array parameters, similar to [105], were conducted on the dimension of the waterbolus and the distance between the two rings. The optimized design had two rings with an inter-ring distance of 5 cm and a waterbolus with the major axis, minor axis, and height of 14, 11, and 14 cm, respectively. The second and third configurations had a helmet-like shape with 11 and 19 elements. It should be mentioned that the old antenna model (SGBW) had been used in these simulations. However, given the comparative nature of the investigation, one should be able to generalize the result. Another subtle distinction is that the complete SGBW antenna model including its balun was used in the ring configuration whereas the simulation of helmets did not include the balun and used discrete lumped ports right at the location of the antenna pins.

As can be seen from Figure 2.8(e), the configuration with 11 elements for the helmet design does not guarantee deep enough penetration to reach the target. The configuration with 19 elements, on the other hand, is rather effective but at the expense of more stray losses deposited in the healthy tissue. It is also more complex hardware-wise and requires more input power due to the higher number of antennas. Performance of the ring configuration is somewhere in the middle, showing results between those two bounds achieved by the helmet designs. It provides good coverage of the tumor with the lowest level of stray losses deposited outside the target. For the same default input power of 0.5 W per channel, a bit fainter color for the focal spot of this design compared to those of the helmet designs can be partly linked to the losses associated with the balun in this simulation.

Based on the aPA metrics, level of the undesired power deposition in healthy tissue, and the number of antennas, the elliptical ring configuration was selected as the optimal design for *Paper B*. This selection is in line with the conclusion made by other groups active in the field. Oberacker et al. [56], for instance, showed that the best results in a power optimization sweep are

Table 2.2: Summary and comparison in terms of aPA among the three different array configurations used in the head phantom simulation.

Array Configurations	Annular Elliptical	Helmet	
Number of Antennas	16	11	19
$\sum^{V_T \approx 13(\text{ml})} PLD$ (W)	0.0318	0.0315	0.0445
$\sum^{V_H \approx 3600(\text{ml})} PLD$ (W)	2.81	2.94	3.8
aPA	3.13	2.96	3.24

Table 2.3: Dielectric properties of the tissues and the power deposited in them in the simulation of the child model at 400 MHz (σ: electric conductivity, ε_r: relative permittivity, ρ: density).

Tissue Type	**Index**	σ [**S/m**]	ε_r	ρ [**kg/m^3**]	**Volume (ml)**	$\sum^V PLD$ **(W)**
Skin	1	0.73	44.9	1109	496	0.76
Muscle	2	0.82	56.4	1090	1633	0.51
Bone	3	0.1	12.9	1908	438	0.18
CSF	5	2.28	70.1	1007	341	0.32
Gray matter	6	0.78	55.8	1045	1007	0.68
White matter	7	0.47	41	1041	124	0.04
Tumor + Cyst	8	0.85	56.6	1056	126	0.35
Eye	9	1.54	68.9	1005	18	0.02
Cartilage	10	0.62	44.6	1099	6	0.014

obtained for a 16-element interleaved RF applicator using an elliptical antenna arrangement with waterbolus.

To test the power deposition capability of the ring configuration with ORWG antennas, two realistic and very challenging cancer cases of the pediatric medulloblastoma and adulthood central nervous system (CNS), shown in Figures 2.9(a) and 2.9(b), were further considered at the frequency of 400 MHz. Dielectric properties reported in Table 2.3 were used for the child model and those related to the CNS-Duke model were taken from the IT'IS database [106]. The built-in PSO optimizer of CST was used to maximize their aPA ratios. The optimum values of 4.5 and 4.8 were obtained for the medulloblastoma and CNS scenarios, respectively.

Compared to the Duke model where there are more than 45 tissue types, the child model has only 10 tissue types which makes it very convenient to tabulate

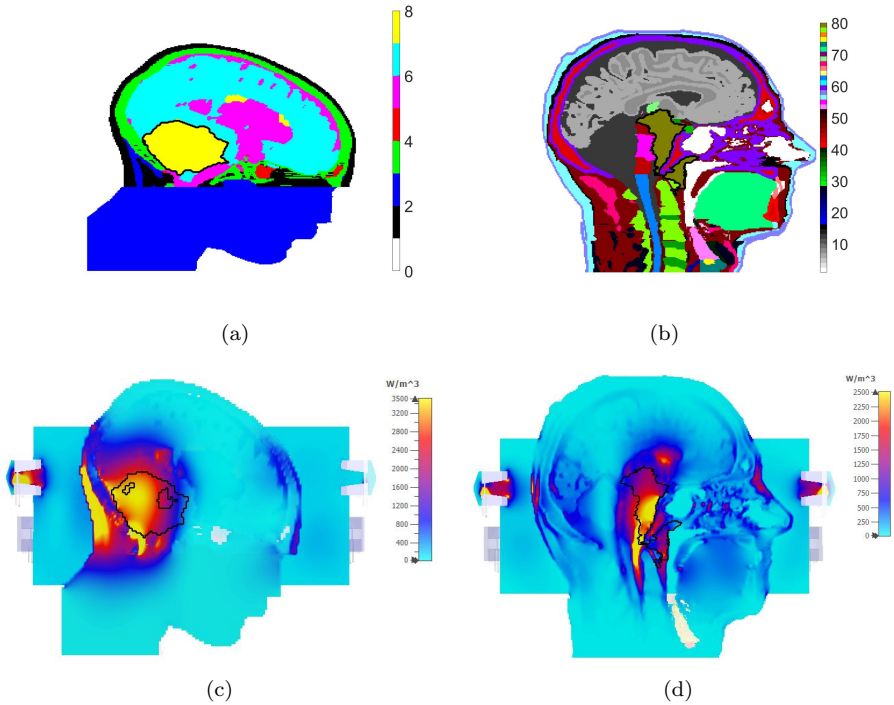

Figure 2.9: Sagittal cross-sections of the realistic models for (a) a child with a big medulloblastoma tumor and (b) an adult with a tumor in CNS. (c) and (d) are their corresponding PLD distributions (solid black lines show the border of the tumors).

the amount of power absorbed by each tissue type as in the last column of Table 2.3. Out of 3.95 W of the stimulated power, 3.72 W has been absorbed by the dielectrics of which 0.85 W is the share of water. The normalized absorbed power per volume of each tissue type is reported in Figure 2.10.

2.5 Hyperthermia Treatment Planning

Hyperthermia treatment planning (HTP) is a process in which a set of treatment parameters are established by EM and thermal modellings to maximize

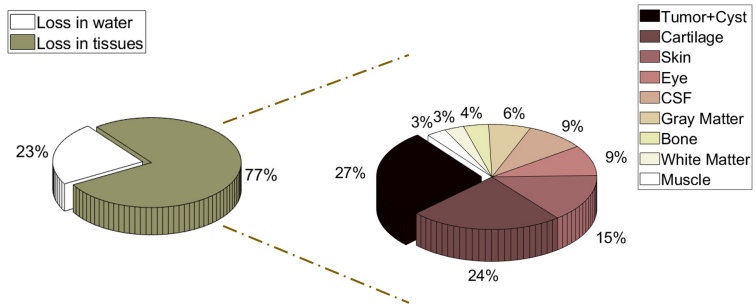

Figure 2.10: Separate representation of the normalized power dissipated per occupied volume of each tissue type for the child model.

the treatment quality [76]. HTP simulation tools can be used to develop enhanced treatment approaches or, retrospectively, to analyze treatment quality. In recent years with the introduction of more powerful EM simulation tools and software packages capable of handling thermal simulations, HTP has begun to appear in the clinical HT routines because of its ability to predict clinical outcomes [28]. It helps evaluate the effectiveness of different scenarios before HT sessions to aid in the selection of applicator or treatment approach and specific power excitation planning. In addition, simulations are helpful for assessing treatment risks to the patient or operator.

As depicted in Figure 2.11, simulations for HTP can be divided into three distinct tasks summarized below and further elaborated upon each separately in the subsequent sections.

1. **Generation of the patient model for Computational Electromagnetics (CEM):** Starting with patient data acquisition, the geometry and tissue properties of the involved body region must be carefully determined. Using computed tomography (CT) or magnetic resonance images (MRI) of the actual subject, manual or semi-automatic segmentation needs to be performed to obtain the patient-specific model.

2. **Calculation of the PLD/ SAR distributions in the tissue:** Patient's model and a model of the applicator with the required degree of complexity are combined and used to compute the PLD/ SAR distribution.

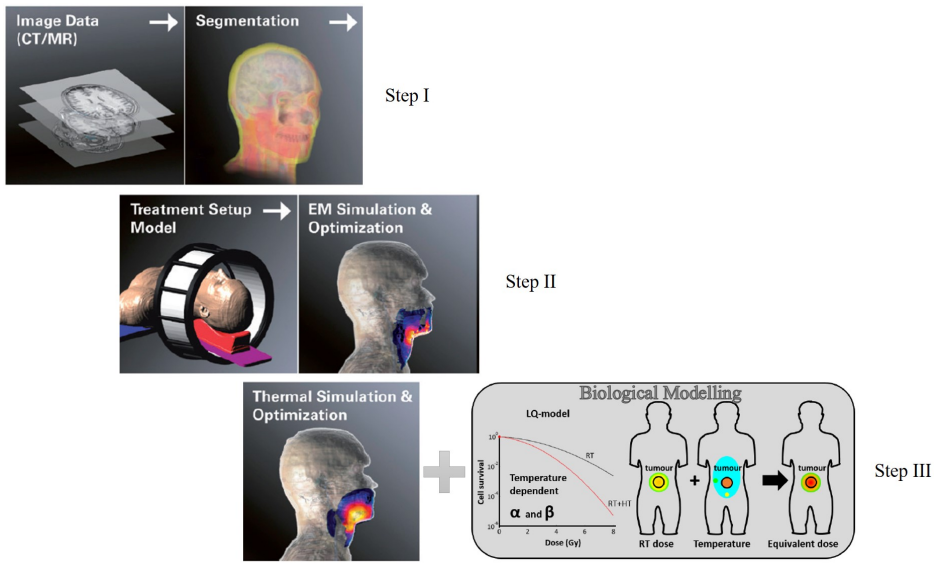

Figure 2.11: Schematic workflow for EM-HTP (Reprinted fron [76] and [28]).

3. **Calculation of the resultant temperature distribution and post-processing analysis in case of a combined treatment modality:** Once the PLD pattern is established, the temperature (T) distribution can be predicted considering the impact of physiological aspects such as perfusion and core temperature. In synergistic treatment modalities like thermoradiotherapy, a further step can be also taken to quantify the radio-sensitizing effect of hyperthermia.

Step I. Human Models for CEM Research

Realistic computational human models or 'virtual humans' are becoming a significant component of modern biomedical research. The Virtual Population from IT'IS Foundation Switzerland [107], [108] is certainly one of the most comprehensive model families for CEM and radiological simulations. Major members of the virtual population are shown in Figure 2.12 and tabulated in Figure 2.13.

A vast majority of the virtual-human models available are voxel models

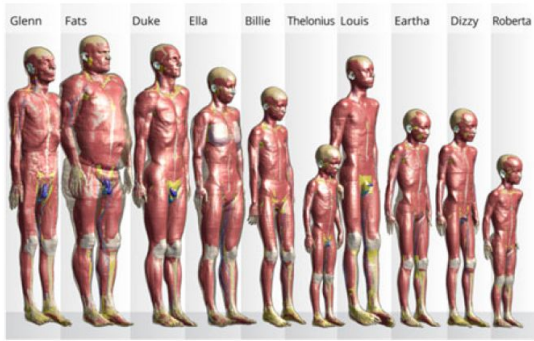

Figure 2.12: Member of IT'IS Virtual Population – Voxel models.

and not CAD models. The difference between CAD and voxel models is quite significant and influences both the type of the CEM problems to be solved (resonant or not) and the EM solver type [109]. Voxel-based models naturally represent highly-inhomogeneous inter-tissue regions and can replicate these tissues exactly as they appear in the source images. This is not the case with 3D CAD models of a multi-tissue body as they are much more difficult to construct. Furthermore, detailed triangulated human models with a very large number of triangles can be very computationally expensive, both in terms of FEM meshing times to create a volumetric tetrahedral mesh and in terms of FEM simulation times. This can make their use prohibitive for a number of optimization tasks.

On the other hand, triangular- or quadrilateral-based CAD models have a clear mathematical advantage which is a linear surface approximation in contrast to the staircase approximation of the voxel grid. In fact, the segmentation accuracy which is the deviation from the true surface along the normal direction is equal to the size of the unit cell for voxel models. Moreover, voxel models are inflexible to deformations while the CAD models are inherently deformable including both free-form deformations and affine transformations [109]. Last but not least, CAD models are fully compatible with the standard FEM analysis on unstructured grids and 3D printing while the voxel models are not.

The two realistic models used in this chapter are shown in Figure 2.14. The first model, henceforth called case-study 1 in this section, is the head of the

Model Name	G/A/H/W	Da	TYPE	RES, mm^3	FV	D
Glenn	m/84/173/61.1	N	V	0.5x0.5x1.0h 0.9x0.9x2b	N	Y
FATS	m/37/182/119	N	V	0.5x0.5x1.0h 0.9x0.9x2b	N	Y
DUKE	m/34/177/70.3	N	V/S	0.5x0.5x1.0h 0.9x0.9x2b	Y	Y
ELLA	f/26/163/57.3	N	V/S	0.5x0.5x1.0h 0.9x0.9x2b	Y	Y
LOUIS	m/14/168/49.7	N	V	0.5x0.5x1.0h 0.9x0.9x2b	N	Y
BILLIE	f/11/149/34.0	N	V/S	0.5x0.5x1.0h 0.9x0.9x2b	Y	Y
EARTHA	f/8/136/29.9	N	V	0.5x0.5x1.0h 0.9x0.9x2b	N	Y
DIZZY	m/8/137/25.4	N	V	0.5x0.5x1.0h 0.9x0.9x2b	N	Y
THELONIOUS	m/6/115/18.6	N	V/S	0.5x0.5x1.0h 0.9x0.9x2b	Y	Y
ROBERTA	f/5/109/17.8	N	V	0.5x0.5x1.0h 0.9x0.9x2b	N	Y
NINA	f/3/92/13.9	N	V	0.5x0.5x1.0h 0.9x0.9x2b	N	N
CHARLIE	f/8w/na/4.3	N	V	0.5x0.5x1.0h 0.9x0.9x2b	N	N

Figure 2.13: G/A/H/W—Gender/Age/Height/Weight; Da—Original image dataset made available for independent evaluation (Y/N); TYPE (V—voxel; S—surface-based model, but without proven FEM meshability); RES-Lowest image resolution (before or after post-processing) of the model declared by the provider (h = head, b = body); FV—Free version availability (Y/N); D—Deformable/posable (Y/N). Rerinted from [109].

Duke model from IT'IS which was down-sampled to the resolution of 2 mm for the sake of faster simulations and a tumor was inserted in the tongue region as shown in red in Figure 2.14(a). The second model, henceforth called case-study 2, is the same as the one presented in Section 2.3. The only distinction is that the original tumor was too large for radiosurgery with $\gamma-$knife and was thus reduced to 34 mL by means of morphological operations. This model was manually segmented from an MRI scan with a $1 \times 1 \times 1$ mm resolution of a 13-year old boy with medulloblastoma treated at Sahlgrenska University Hospital. Note that only a part of the head was segmented, and the section outside the treatment volume was modelled as muscle.

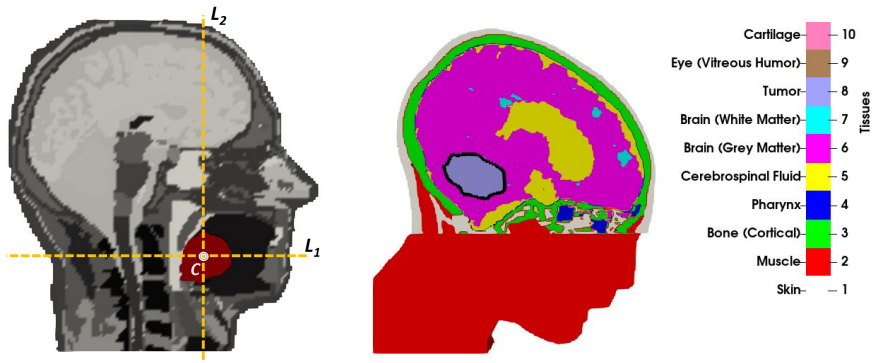

(a) case-study 1 (b) case-study 2

Figure 2.14: Sagittal cross-sections of (a) The Duke model with a tumor shown in red in the tongue region – L_1 and L_2 are 2D cut-lines for thermal validation and C is the center of the tumor where the two lines intersect (b) The child model with shrunken medulloblastoma.

Step II. EM Simulation & Optimization

EM Field Simulation

The type of EM technique used depends on the human model availability, e.g. voxel or CAD. Voxel-based models on uniform rectangular grids lend themselves primarily to finite-difference (FD) methods [110] at low frequencies and to the FD time-domain (FDTD) methods at high frequencies [6], [110], [111]. For high frequency EM simulations which involve computational human models, FDTD is currently the major tool. The time domain EM solver of CST uses a variant of this method called finite integration technique (FIT) [112], [113] which is reduced to the standard FDTD on a uniform rectangular grid as shown in Figure 2.15(a) and can simultaneously expand the FDTD method to tetrahedral grids as shown in Figure 2.15(b).

A CAD-based human model is suitable for the finite element method (FEM). Both commercial software packages of ANSYS HFSS[5] and COMSOL[6] use FEM as their computational engine for EM simulations. For radio wave prop-

[5] www.ansys.com/ansys-hfss
[6] www.comsol.com/comsol-multiphysics

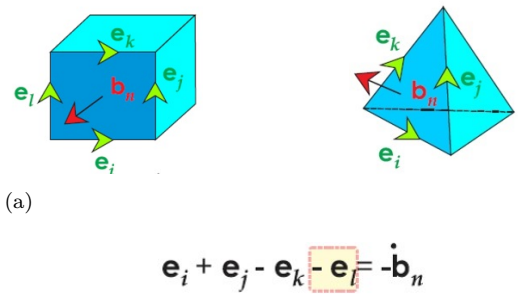

Figure 2.15: Using FIT to discretize Faraday's equation for (a) a cube – similar to the FDTD Yee cell (b) a tetrahedral mesh.

agation, the FEM method has been primarily implemented in the frequency domain which can better resolve resonances. For MRI-related studies, for example, frequency-domain FEM can substantially outperform FDTD simulations [114]. This advantage arises in part from FEM's robust adaptive mesh-refinement capabilities, which optimize the tetrahedral mesh to reduce computational time while still maintaining high simulation accuracy. For complicated geometries, the use of unstructured meshes combined with automatic mesh adaptation in the frequency domain is instrumental in delivering accurate results [109]. On the other hand, it has been traditionally difficult to implement FEM methods in the time domain for a broadband system response. To tackle this issue, discontinuous Galerkin schemes have been developed [115].

SAR-based Optimization

For HTP routines, a focusing technique that guarantees the formation of a focal point at the tumor's location is of paramount importance. In other words, a good power deposition scheme avoids creating hot spots which are excessive focal points formed outside the targeted region. Associated with all the focusing techniques proposed in this context are such heated topics as hot spot suppression and multi-target beamforming based on either specific absorption rate (SAR) or temperature. In fact, whether SAR, as is the case in this thesis, or temperature should be optimized is still a matter of debate

[116]. Although the final goal of the treatment is to generate a temperature gradient between tumor and healthy tissue, all the potential benefits of direct temperature optimization may be lost under the heavy computational burden due to large uncertainties in thermal modeling [117]. Moreover, Lee et al. [118] demonstrated a good correlation between SAR coverage indicators and clinical outcomes of HT.

Because the problem of finding appropriate excitations for each individual channel in an RF/MW applicator is non-convex, finding the global optimum has proven to be challenging and computationally expensive. To tackle the issue, several beamforming methods have been proposed in the literature among which we count the generalized eigenvalue problem (EGV) [119], time reversal (TR) [120], particle swarm optimization (PSO) [121], focusing via constrained optimization (FOCO) [122], [123], and multiplexed vector field shaping (MVFS) [124].

While fast and efficient, the EGV is highly dependent on its functional definition. For instance, other indicators like hotspot-tumor quotient (HTQ), which has so far shown the most successful correlation with clinical results [125], cannot be used as the functional for this method. Moreover, the method does not allow for simultaneous optimization of multiple frequencies. TR is a fast and popular method widely used in the literature, albeit with several limitations: (a) due to the emergence of ghost focal points, TR's focusing capability decreases for the large target areas (b) the performance is highly dependent on the selection of 'virtual source position'. PSO and FOCO are more computationally demanding, but they offer more flexibility when it comes to beam-shaping and the adoption of different fitness functions. Using only the predominant field component at a single or a very few points in a scalar regime, FOCO linearizes the problem which may not lead to the optimal solution if the assumption of a single dominant component in the target region does not hold true. Like FOCO, MVFS falls into the category of convex optimization approaches but with the distinction that there is no linearization in its formulation and hence it is not scalar. MVFS casts the constrained RF/MW heating problem into a semi-definite program of a time- and frequency-multiplexed iterative optimization algorithm and quickly solves it to global optimality.

To find the optimum excitations for antenna elements of the proposed applicator, this chapter utilizes PSO while taking advantage of TR fast computation by using it as the starting point. It goes without saying that using an

educated initial guess can help to reduce both the optimization time and the odds of getting trapped in local minima.

Implementation of PSO in EM problems is straightforward as discussed elsewhere [126]. The main steps taken are listed below.

- **Definition of the problem space:** if N is the number of antennas, then the goal is to find N complex numbers (each has a phase and amplitude that is normalized to the maximum in the set) in such a way that they make a focal point on tumor when excited simultaneously. To this end, 15 particles are set to search the solution space of a unit circle in the complex plane. So each particle is an N by one vector of complex numbers in that space.

- **Initialization of the $1^{\mathbf{st}}$ swarm:** TR setting is assigned to the first particle in the set because we want to take advantage of having a good initial guess and to expedite the whole process of the optimization. The rest of the particles are initialized by being assigned random complex numbers in the search space.

- **Cost Function:** a well-defined goal function is the key to every successful optimization problem. Although there are a lot of different indicators defined in the literature to reflect SAR distribution in tumor's volume, HTQ so far seems to be the most promising, showing a better correlation to clinical outcomes. Therefore, it is selected as the cost function here as follows

$$HTQ = \frac{\overline{SAR}(V_{1\%})}{\overline{SAR}(T)} \tag{2.12}$$

  where $\overline{SAR}(V_{1\%})$ and $\overline{SAR}(T)$ are the highest percentile of SAR distribution in the healthy tissue and the mean SAR absorbed by the tumor, respectively.

- **Termination condition:** the optimization is terminated when the maximum number of iterations (M) or the maximum number of stall iterations (S) is reached, whichever comes first. In this problem, M and S are set to 30 and 5, respectively.

Given that the size of tumors is different in these two scenarios, with case-study 2 having a much larger tumor volume, frequencies of 500 MHz and

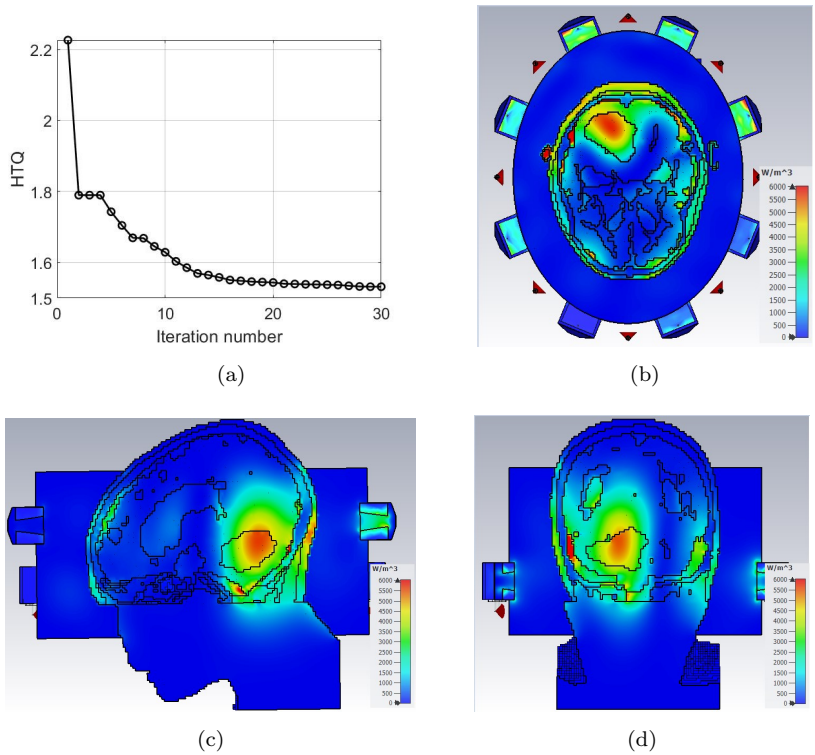

Figure 2.16: (a) TR-PSO for minimization of the HTQ at 400 MHz (b), (c), and (d) PLD distributions for the normalized excitation power of 0.5 W per channel in transverse, sagittal, and coronal planes, respectively.

400 MHz are selected for case-study 1 and 2, respectively. Results of the cost function minimization and beamforming for case-study 1 have been reported in *Paper B* and thus not repeated here. The corresponding results for case-study 2 are shown in Figure 2.16. As can be seen from the plot, the hyperthermia treatment plan resulted in an HTQ value of 1.53 in less than 30 iterations. SAR treatment quantifiers of target coverage 25% (TC_{25}) and 50% (TC_{50}) were measured to be $TC_{25} = 97\%$ and $TC_{50} = 78\%$. TC_x indicates the percentage of the tumor volume that is enclosed by the iso-contour of $x\%$ of the maximum deposited SAR in the tumor.

Step III. Thermal Simulation

To fully understand and evaluate HT treatment sessions, SAR simulations need to be followed by thermal analysis in order to account for relevant cooling mechanisms as tissue perfusion and waterbolus cooling. The most widely used model for this purpose is the Pennes Bioheat equation [127]. While computationally efficient, Pennes equation provides a simplified model for the phenomenon as it fails to account for the direction of the blood flow or heat exchange between large blood vessels and tissue. Van den Berg et al. [128] have shown that this can result in significant inaccuracies in temperature prediction of about 1–2°C. To address the issue and to improve temperature predictions in HTP, advanced thermal models such as DIVA which includes large discrete vasculature have been developed [129]. These advanced models are, however, computationally expensive and require GPU-based algorithms for a fast and efficient implementation. Moreover, a detailed and adequate estimation of blood flow during hyperthermia which is an important input parameter to these models remains challenging and subject of further research [28].

While commercial solvers like CST and COMSOL can be used to tackle such a multi-physics problem to some extent, a modular open-source computational engine provides more flexibility to model, simulate, and optimize the treatment planning workflow. It can also save computational time upon efficient implementation. Moreover, CST uses only hexahedron meshes for thermal simulation of biological models which limits the ability of its solver to conform the meshes to the natural curvatures of the biological structures/ tissues. As a result, it can give rise to staircase approximations at tissue borders. COMSOL, on the other hand, uses the tetrahedron mesh type, which is more flexible for conformal meshing, but at its current implementation, COMSOL's mesh generator package cannot handle very sophisticated structures like human bodies with lots of intricate tissue geometry. Despite the availability of a possible workaround suggesting the dielectric mapping instead of importing the whole physical body model into COMSOL [130], [131], this solution introduces additional approximation due to dielectric interpolation at tissue borders. Interested readers are encouraged to consult [132] for more information on the limitations of commercial thermal solvers, as well as the implementation details of an alternative open-source computational engine for Hyperthermic thermal simulations.

Development of a FEniCS-based Thermal Solver

In this section, Pennes Bioheat Equation (2.10) in conjunction with the Dirichlet boundary condition of $T = T_{\text{bolus}}$, i.e. a fixed waterbolus temperature at the border of the computational domain, has been considered for thermal modelling. A brief overview of the theoretical approach to model the physical phenomenon is first given and the integral 'weak forms' are derived. Then the open-source codes of the Finite Elements of nonlinear iterative Computational Science (FEniCS) project [133] have been used to numerically solve the integral forms. FEniCS uses the unified form language (UFL) which provides a flexible interface for defining expressions for weak forms in a notation close to mathematical notations and can be scripted either in C++ or Python. The Python distribution of Anaconda[7] with its powerful IDE, Spyder, which resembles and includes most of MATLAB's functionalities, has been used for the thermal analysis in this study. Finally, the results of FEniCS are presented and crosschecked against COMSOL.

In the context of the finite element method, boundary-value problems can be solved using either the Rayleigh-Ritz variational method or the Galerkin weighted residual method to formulate the elemental FEM equations [134]. In the Rayleigh-Ritz method, the boundary-value problem is formulated in terms of a variational expression, called functional. The minimum of this functional corresponds to the governing differential equation under the given boundary conditions (BC). Natural BCs are automatically satisfied in the process of minimization or maximization of the functional. Essential BCs, on the other hand, have to be explicitly enforced, hence the name 'essential'. Galerkin's method, which belongs to the family of weighted residual methods, seeks the solution by weighting the residual of the governing differential equation. The weighting functions in this method are selected to be the same as the basis functions used for the expansion of the approximate solution (see [134], [135] for a thorough discussion on the subject).

Considering $\frac{\partial T}{\partial t}$ as $(T^{n+1} - T^n)/\Delta t$ which is a central finite difference discretization of the n^{th} time step, the weak form of Equation (2.10) can be derived as:

[7] www.anaconda.com

$$\frac{c\rho}{\Delta t}(T^{n+1}-T^n)=\kappa\nabla^2T^{n+1}+PLD-c_b\omega_b(T^{n+1}-T_b)$$
$$T^{n+1}-T^n-\frac{\kappa\Delta t}{c\rho}\nabla^2T^{n+1}-\frac{\Delta t}{c\rho}PLD+\frac{c_b\omega_b\Delta t}{c\rho}(T^{n+1}-T_b)=0. \quad (2.13)$$

By multiplying Equation (2.13) with the weight function w and integrating it over the computational domain Ω, we get

$$\int_\Omega\Big[T^{n+1}w-T^nw-\frac{\kappa\Delta t}{c\rho}\nabla^2T^{n+1}w-\frac{\Delta t}{c\rho}PLD\cdot w+\frac{c_b\omega_b\Delta t}{c\rho}(T^{n+1}-T_b)w\Big]d\Omega=0.$$

The 'weak form' means reducing the second-order derivative of ∇^2T to a first-order derivative using By-part integration for higher orders. The product rule for divergence from vector identities in mathematics states that $\boldsymbol{\nabla}\cdot(w\boldsymbol{V})=w\boldsymbol{\nabla}\cdot\boldsymbol{V}+\boldsymbol{\nabla}w\cdot\boldsymbol{V}$ for a given vector $\boldsymbol{V}$ and a scalar w. Now, considering $\boldsymbol{\nabla}T^{n+1}$ as $\boldsymbol{V}$, the following mathematical manipulation can be performed

$$w\nabla^2T^{n+1}=w\boldsymbol{\nabla}\cdot\boldsymbol{\nabla}T^{n+1}=\boldsymbol{\nabla}\cdot(w\boldsymbol{\nabla}T^{n+1})-\boldsymbol{\nabla}w\cdot\boldsymbol{\nabla}T^{n+1}$$

which can be further simplified using the divergence theorem to get

$$\int_\Omega w\nabla^2T^{n+1}d\Omega=\int_{\partial\Omega}w\boldsymbol{\nabla}T^{n+1}d\Gamma-\int_\Omega\boldsymbol{\nabla}w\cdot\boldsymbol{\nabla}T^{n+1}d\Omega. \quad (2.14)$$

According to the essential Dirichlet BC and the fact that we have no variation on the border, the first term in the right-hand side of Equation (2.14) vanishes and the substitution of the second term into Equation (2.13) gives the following weak form equation

$$\int_\Omega\Big[T^{n+1}w-T^nw+\frac{\kappa\Delta t}{c\rho}\boldsymbol{\nabla}w\cdot\boldsymbol{\nabla}T^{n+1}-\frac{\Delta t}{c\rho}PLD\cdot w+\frac{c_b\omega_b\Delta t}{c\rho}(T^{n+1}-T_b)w\Big]d\Omega=0. \quad (2.15)$$

Finally, using the UFL notation, Equation (2.15) can be written in a Python script as the symbolic Bioheat equation ($F_{n+1}(T;w)=0$) and then FEniCS can be asked to separate the linear ($L(w)$) and bi-linear ($a(T,w)$) parts and solve the equation. Interested readers can consult [136] for detailed instructions on how to write a UFL Python script for heat equations in general. Note that the steady-state analysis can also be easily performed by setting $\frac{\partial T}{\partial t}$ in

Equation (2.10) to zero and repeating the weak form calculation as discussed above.

Following the instructions in its official website[8], the latest stable version of FEniCS can be installed on a Linux distribution such as Ubuntu[9] or on the Windows Subsystem for Linux (WSL)[10] in a Windows-based machine. After a successful installation of the platform and having the weak form Equation (2.15) scripted in Python and ready, the next step is to import the geometry and the mesh into the platform. FEniCS itself does not provide the necessary tools and functionalities to mesh very complex scenarios such as human bodies with very heterogeneous properties, but it accepts most common mesh types produced by other dedicated mesh generators. In particular, it provides two mesh converters, i.e. *dolfin-convert* and its modern version *meshio*, to convert the imported meshes to the *xml* format for its internal processes. A powerful MATLAB-based meshing toolbox called Iso2mesh[11] is used in this study to mesh the scenarios. Iso2mesh allows for the tissue-specific assignment of blood perfusion rate and other thermal properties by giving each tissue type a unique identifier. It can also save the meshes in the *Gmesh*[12] format that can be later imported, converted, and used by FEniCS. To compute the solution, FEniCS offers a variety of linear solver methods based on either Krylov iterative solvers such as Conjugate gradient (Cg) and generalized minimal residual (gmres) methods with different pre-conditioners or direct LU-decomposition methods such as PETSc and Multifrontal Massively Parallel Sparse direct Solver (MUMPS). The appropriate selection of the solver depends on the scenario, the number of mesh cells, available RAM of the operating computer, desired accuracy, and the run-time. After running the simulation, FEniCS can output the result in *HDF5* or *vtk* formats. The latter is a very convenient choice for post-processing and visualization in ParaView[13].

[8] www.fenicsproject.org
[9] www.ubuntu.com
[10] https://docs.microsoft.com/en-us/windows/wsl/about
[11] www.iso2mesh.sourceforge.net
[12] www.gmsh.info
[13] www.paraview.org

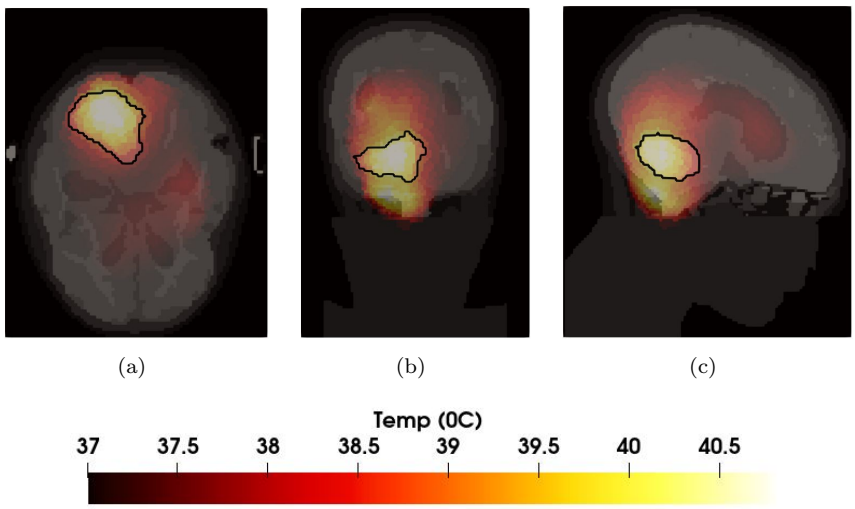

Figure 2.17: Temperature distributions for case-study 2 in (a) transverse, (b) coronal, and (c) sagittal planes.

Thermal Evaluation & Analysis

After exporting the EM fields from CST, thermal analysis for both case-studies were performed using FEniCS. Steady-state temperature distributions for case-study 1 has been reported in *Paper B* and those of case-study 2 are shown in Figure 2.17. To quantify the quality of the treatment outcome based on commonly used metrics in the HT community, thermal indicators of T_{90}, T_{50}, T_{10} were measured as follows: $T_{90} = 38.57°\text{C}$, $T_{50} = 39.79°\text{C}$, and $T_{10} = 40.77°\text{C}$. The thermal indicator of T_x determines the temperature in the target tumor exceeding by x percent of all the temperature values.

The thermal distribution obtained for case-study 1 was compared to that of COMSOL. As stated earlier, we do not expect to see identical results due to limitations associated with the current implementation of COMSOL. Figures 2.18(a) and 2.18(b) present the steady-state temperature distributions computed by FEniCS and COMSOL along the cut-lines L_1 and L_2 that run through the center of the tumor and are shown in Figure 2.14(a). As can be seen, there is a good agreement between the two solvers in general. The pre-

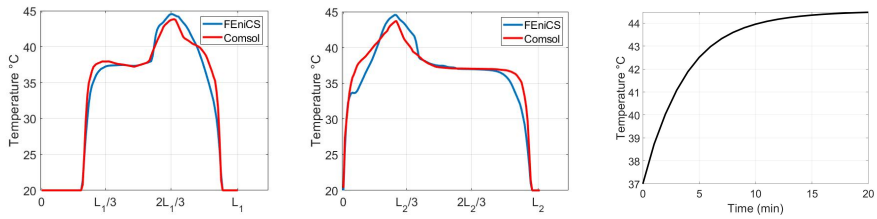

(a) (b) (c)

Figure 2.18: Steady-state temperature profiles of case-study 1 simulated both by FEniCS and COMSOL along (a) L_1 (b) L_2. (c) Transient temperature evolution in the center of the tumor (point C) over a time window of 20 minutes simulated by FEniCS.

dicted distribution of FEniCS is, however, smoother than COMSOL because of the finer meshes employed. The highest possible number of mesh cells that COMSOL could handle for this scenario was used. Yet, as the sharp edges in red curves indicate, the number of mesh cells in COMSOL needs to be higher to obtain a smoother thermal distribution. For the transient analysis, Figure 2.18(c) shows how temperature at the center of the tumor (point C in Figure 2.14(a)) evolves during a time window of 20 minutes of HT application. After almost 15 minutes, the steady-state condition reaches with temperature plateauing at 44.5 °C. The transient result is presented only for the FEniCS case because the COMSOL solution did not converge at the end due to the spatial resolution of the meshes and its impact on the temporal steps. On the contrary, a Crank-Nicolson scheme for temporal steps in FEniCS was utilized which guaranteed the convergence in a reasonable deal of simulation time. Below, the temporal stability is briefly elaborated upon.

As mentioned earlier, the central FD scheme for temporal steps was used to obtain Equation (2.15). However, for complex geometries where there are very fine and detailed mesh cells, there are other schemes more capable of handling transient problems. This intricacy of the mesh can have an implication on the numerical stability and convergence of the method. The so-called θ-scheme offers three discretization methods in one notation as follows

$$\frac{c\rho}{\Delta t}(T^{n+1}-T^n) = \kappa\theta\nabla^2 T^{n+1}+\kappa(1-\theta)\nabla^2 T^n+\theta f(t_{n+1})+(1-\theta)f(t_n) \quad (2.16)$$

where f is the source/ sink term. Depending on the value of θ, Equation (2.16) can be considered as the explicit Euler scheme, for $\theta = 0$; the Crank-Nicolson scheme, for $\theta = \frac{1}{2}$; or the implicit Euler scheme, for $\theta = 1$.

CHAPTER 3

SEM: EM Modeling of Beamforming Metasurfaces

A rich variety of electromagnetic properties has been witnessed in natural materials and harnessed over centuries. However, the ambitious desire of having full control over EM properties of materials in recent years has put a stringent demand on nature, which cannot, despite its rich diversity, equip us with a full range of materials to realize all physically possible effects and phenomena. This is where the artificial, engineered substances, better known as metamaterials (MTM), come into the picture. Having a set of small scatterers or apertures arranged in a regular array throughout their structures, metamaterials can exhibit some desirable bulk behaviour. In fact, such desired properties as left-handedness (backward waves with phase and group velocities that are in opposite directions), negative refractive index, near-zero index, and so on cannot often be found naturally and thus require some engineering intervention and effort to bring them to life [48]. Volumetric MTMs can, in practice, impose significant dissipation losses and fabrication difficulties. However, it is not always necessary to design a bulk material but rather analogous responses can be obtained by judiciously placing electrically small scatterers into a two-dimensional pattern at a surface or an interface. This gives rise to the concept of metasurfaces (MTS), single-layer 2D counterparts

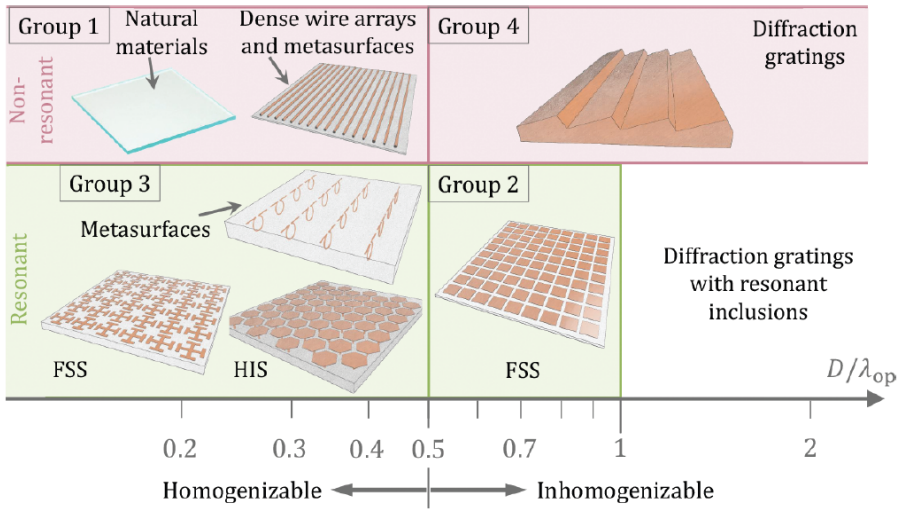

Figure 3.1: Different types of periodic planar structures classified in terms of their homogenizability and the resonant (green shade) or non-resonant (red shade) natures of their operation (Taken and reprinted from [137]).

of the bulk metamaterials [3].

Within the limits dictated by energy conservation, metasurfaces can arbitrarily modify such wave attributes of an incident EM radiation as polarization, amplitude, phase, and wavefront shape both in reflection and transmission scenarios. This property of metasurfaces makes them particularly appealing to applications in need of polarization converters, phase shifters, steering antennas, holograms, and so on. As the brief discussion on surface EM in Section 1.3 revealed, various types of periodic structures have emerged in recent years to cater to different applications. At this stage and based on the distance between adjacent inclusions/elements (D) as well as the type of electromagnetic response (resonant or non-resonant), it might be informative to refer to a classification of some common forms of these structures proposed by [137] and reprinted above in Figure 3.1.

The topic of this chapter revolves around the metasurfaces belonging to the third category of Figure 3.1, i.e. homogenizable ($\frac{\lambda_{op}}{30} \leq D \leq \frac{\lambda_{op}}{2}$) single-layer composites of macroscopic inclusions under resonance.

3.1 Homogenization Approach & Floquet Theorem

Being polarizable interfaces and often idealized as an electromagnetic discontinuity of exactly zero-thickness, metasurfaces are in need of a new set of boundary conditions because the conventional boundary conditions found in most electromagnetic textbooks do not rigorously apply to these kinds of interfaces [138]. There is, however, a modified set of rigorous boundary conditions commonly referred to as the Generalized Sheet Transition Condition (GSTC) which was first developed by Idemen [139] and later applied to metasurfaces by Kuester et al.[140]. In short, the GSTCs form a set of coupled inhomogeneous partial differential equations which has enabled the researchers in the field to cast the metasurface synthesis into an inverse problem whose solution generally leads to a closed-form formula for synthesized surface susceptibilities [138]. GSTC, whose technical discussion is beyond the scope of this text, offers the most rigorous and thorough characterization technique for an infinitesimally thin metasurface but comes at the cost of a discrepancy between the scattering response of the zero-thickness model and that of the thin metasurface slab. However, there exists a much simpler technique (not so general or rigorous as GSTC) using the homogenized theory [141].

Periodic nature of metasurfaces lends itself to the efficient utilization of spatial harmonic analysis using Floquet theorem, a spatial counterpart of the Fourier series. In the sub-wavelength regime where the periodicity of the inclusions is much smaller than the operating wavelength, considering only the first-order response of the surface will be sufficient. More precisely, it can be shown that the propagation of higher-order Floquet harmonics will be suppressed if the operating frequency (f_0) satisfies the following condition

$$f_0 < \frac{c}{d(\sqrt{\varepsilon_{reff}} + sin\theta_i)} \tag{3.1}$$

where c is the speed of light in free-space, d is the lattice periodicity, ε_{reff} is the effective relative permittivity of the surrounding medium, and θ_i is the incident angle of the impinging EM wave [142]. In other words, higher-order Floquet modes (grating lobes) are in cut-off when Equation 3.1 is satisfied. Under this condition and according to the averaged theory, the periodic surface can be modeled as a homogeneous interface characterized by a finite surface current, and consequently, it can be represented by a uniform sheet with a frequency-dependent surface impedance [143].

At this point, an overall review of the Floquet concept may serve interested readers well and will also facilitate discussion flow in the remainder of the chapter. For simplicity, let us consider a 1D periodic structure lying on the xz-plane with lattice periodicity d_z along the z-axis. Due to spatial periodicity, which leads to having periodic boundary conditions (PBC), any EM field components at the borders can be described by

$$\phi(x, y, z + d_z) = e^{-jk_{z0}d_z}\phi(x, y, z) \tag{3.2}$$

which implies that the field components differ only by a phase term indicated by the exponential factor $k_{z0} = \beta - j\alpha$ (where β and α are the propagation and attenuation constants, respectively). This is in accord with Floquet-Bloch theorem [144], stipulating that an EM wave propagating through a periodic medium takes on the same periodicity as that of the hosting medium. In other words, while plane waves are the eigen modes of propagation in a homogeneous medium, the eigen modes of a periodic medium, known as Bloch modes, are traveling waves modulated by standing waves. Therefore, the field component satisfying Equation 3.2 can be written as

$$\phi(x, y, z) = e^{-jk_{z0}z} \cdot p(x, y, z) \tag{3.3}$$

where p is the modulating periodic function such that $p(x, y, z) = p(x, y, z+d_z)$ which can then be expanded in a Fourier series form

$$p(x, y, z) = \sum_{n=-\infty}^{n=+\infty} a_n(x, y)e^{-j\frac{2\pi n}{d_z}z} \tag{3.4}$$

with a_n being the structural coefficients describing the field variations in the x and y directions. Substituting Equation 3.4 into 3.3, the final field distribution can be written as $\phi(x, y, z) = \sum_{n=-\infty}^{n=+\infty} a_n(x, y)e^{-jk_{zn}z}$ where $k_{zn} = k_{z0} + \frac{2\pi}{d_z}n, \quad n = 0, \pm1, \pm2, ...$ which is often called Floquet spatial harmonic expansion.

3.2 Reconfigurability Mechanisms

As mentioned in the opening of Section 1.3, reflectarrays and transmitarrays are two prime examples of quasi-periodic surfaces whose reconfigurable versions, i.e., RRA and RTA, have in recent years laid the foundation for the

heated topic of engineered EM metasurfaces in wireless communication, a concept widely known as reconfigurable intelligent surface (RIS) in the literature. Therefore, to better understand the basic concept of RISs, we may benefit from looking back to their "ancestors" whose enabling technologies and mainstream reconfigurability mechanisms are neatly reviewed in [145]. Reflectarrays and transmitarrays, as their names may suggest, are interesting hybrids between aperture antennas, such as reflectors and lenses, and antenna arrays. Due to their attractive qualities, they have been the subject of extensive investigation for many years, and their electronically tunable versions have garnered significant attention over the past decade. Indeed, reconfigurability turns RAs and TAs into powerful beamforming platforms by combining the best features of aperture antennas and phased arrays.

A simple statistical analysis on the number of publications over a 20-year period, conducted recently by Ramaccia et al. [146] and reprinted here in Figure 3.2(a), reveals a steady and significant growth in the publication trends on both reconfigurable MTMs and tunable MTSs. Another interesting observation from these publication volumes over the years is that while both categories exhibit an upward trend, reconfigurable metasurfaces seem to be outpacing their metamaterial counterparts, probably thanks to their thinner profile and potentially simpler fabrication methods. When it comes to EM reconfigurability techniques and implementation methods, Figures 3.2(b) (taken from a survey in 2014 [145]) and 3.2(c) (reprinted from a much more recent survey [146] in 2025) show that the primary approaches have remained more or less the same over the years, although the techniques in each category have inevitably become more mature over time. Mechanical-based, material phase change, and electronic lumped element tunability approaches, as depicted in the figure, are the three pillars, choice of which ultimately depends on application-specific requirements such as operational frequency band, desirable tunability range, switching speed, and power consumption. Given the intended application in wireless communication at FR1 (sub-6 GHz frequency range), this thesis exclusively focuses on the third category, i.e., electronic approaches, and more precisely on the varactor-diode sub-category within that family.

EM systems in general better lend themselves to electronic reconfigurability because of their natural compatibility with printed circuit board technology and simpler driving strategy via electric signals. Thanks to this granular con-

trol provided by electronic lumped elements, the EM community has been able to realize spatially dispersive reconfigurable metasurfaces whose properties can be controlled not only in time but also in space, an idea widely known as space-time or spatio-temporal (ST) modulation [147], [148]. When comparing the reconfiguration speed with the frequency of the interacting EM wave in the context of ST modulation, two operational modes can be identified i.e., the quasi-static regime where the reconfiguration speed is much slower than the frequency of the EM field, and the dynamic regime, which is characterized by a reconfiguration speed comparable with the frequency of the illuminating EM field.

Diode-based reconfigurability methods, either PINs or varactors, continue to dominate within the electronic family while MEMS have gradually faded away during the years due to their relatively more complex and expensive fabrication process and also their slow switching speed, typically falling into the kHz (millisecond) range. Varactors are semiconductor devices that provide voltage-controlled variable capacitors for tunability. They offer fast switching speed and broad tuning ranges (continuous phase control) but suffer from relatively high insertion losses, limited power handling capabilities, and also a limited range of operational frequency which barely exceeds a couple of few GHz. On the other hand, PIN diodes, which are also semiconductor devices consisting of a wide and undoped intrinsic region sandwiched between a P-N junction, offer a faster switching rate thanks to their very low reverse recovery time. PIN diodes also excel in terms of insertion losses, power handling capabilities, and range of operation frequency. However, the downside of a PIN diode implementation is its limited tuning performance, as a single PIN element can switch only between two different states (providing 180 degrees phase discretization), while the use of multiple PIN diodes to achieve a discrete number of reconfiguration states significantly increases the complexity of the unit cell design and DC biasing feed network. As a compromise to achieve a sufficient phase discretization level of 45° (8 states), an RF-switch-based design along with fixed printed delay lines has also been proposed and investigated in the literature [149], [150].

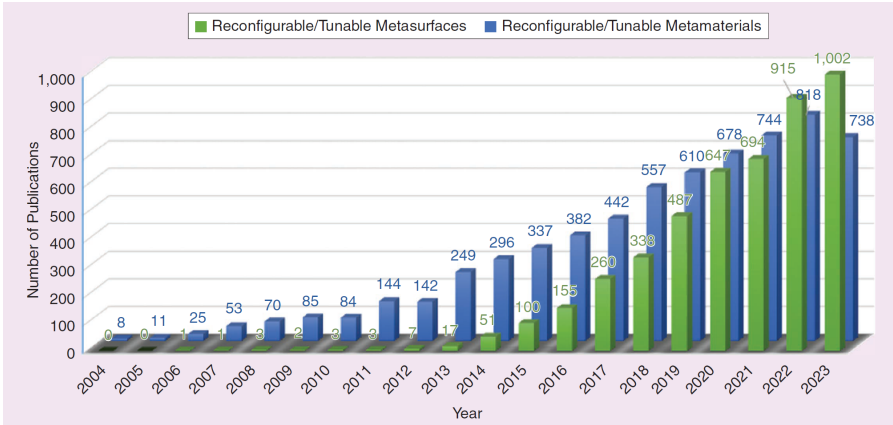

(a)

Type	Technology	Maturity - reliability	Integration (incl. biasing)	D/A control	Complexity (cost)	Loss (microwave / THz)	Bias power consumption	Linearity	Switching time
Lumped elements	PIN diodes	+	-	D	+	-/-	-	0	+
	Varactor diodes	+	-	A	+	-/-	+	-	+
	RF-MEMS	0	+	D[1]	+	+/0	+	+	0
Hybrid	Ferro-electric thin film	0	+	A	0	0/-	+	0	+
Tunable materials	Liquid crystal	0	0	A	0	-/+	0	0	-
	Graphene	-	+	A	0	-/+	+	-	+
	Photo-conductive	0	-	A	0	-/-	-	-	+
Mechanical	Fluidic	0	-	A	0	0/+	+	0	-
	Micromotors	-	0	A	-	+	0	+	-

(b)

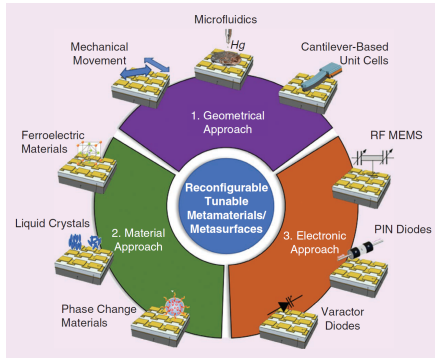

(c)

Figure 3.2: Trends and techniques in reconfigurable meta-devices. (a) Publication numbers per year on tunable metasurfaces vs metamaterials. (b) Mainstream reconfigurability technologies for RRA and/or RTA reviewed in 2014 by Hum et al. [145] along with a qualitative assessment of their related properties, where '+', '0', and '-' symbols refer to good, neutral, and poor, respectively. (c) Three primary reconfigurability approaches in meta-structures reviewed and reported in 2025 by Ramaccia et al.[146].

3.3 RISs in Wireless Communications

Massive MIMO and mmWave communications were two key technologies of the 5G physical layer that helped to significantly increase the network capacity and resolve the spectrum shortage issue in current cellular communication systems [151]. Through boosting system capacity by spatial multiplexing, achieving reliable transmission by diversity, and overcoming propagation loss by beamforming, the multi-antenna technique has indeed played a key role in wireless communications [152]. Yet, the emerging data-intensive applications, such as virtual/augmented reality and autonomous driving, push the ever-increasing traffic demands to a new level that can hardly be supported by 5G, and this is partly why the sixth-generation (6G) of mobile communications has gained a lot of momentum recently, both in industry and academia. In the context of potential enabling technologies for 6G, one can, among an exhaustive list proposed in the literature, enumerate a selected few possibilities

- to further extend the spectrum to terahertz (THz) or even visible-light communication, hence expanding the available spectrum resources [153]
- to scale the antenna arrays to ultra massive MIMO [154] or even gigantic MIMO [155] to boost the spatial diversity and/or multiplexing gain
- to artificially control and shape the electromagnetic wave propagation environment by deploying engineered EM metasurfaces [156].

In line with the last item in the above-mentioned list, this chapter revolves around RIS modeling from the EM point of view. In fact, the emergence of metasurfaces and their widespread applications during recent years has led to the conceptualization of an evolving subdiscipline of electromagnetics commonly known as surface electromagnetics (SEM). Arbitrary manipulation of EM wavefronts is one of the coveted SEM goals which has given rise to the notion of RIS and is poised to play a pivotal role as an enabling physical layer technology in transceiver design for wireless systems and applications. An RIS is a large metasurface panel backed by a control unit that synthesizes a desired radiation pattern using either the generalized law of reflection or holographic beamforming techniques, to be discussed in more detail in the upcoming sections. When it comes to different RIS layouts and operational modalities, they can be broadly categorized into continuous phase gradient

Application	Pros and cons of SEM	Pros and cons of existing solutions
6G and beyond	Pros 1: Reduced power consumption and simplified hardware layer by eliminating phase shifters (e.g., holography). Pros 2: Low form-factor. Pros 3: Capability to realize multiple EM functions from the same surface. Cons 1: Limited frequency bandwidth (additional techniques are available to widen the frequency band of operation). Cons 2: Low to moderate aperture efficiency.	Pros 1: Moderate to high aperture efficiency. Pros 2: Superior beam scanning performance. Cons 1: Increased hardware complexity. Cons 2: Increased power consumption. Cons 3: Increased hardware footprint.

Figure 3.3: Qualitative comparison between pros and cons of metasurfaces vs existing antenna solutions for 6G wireless communication (Taken and reprinted from [160]).

(analog) metasurfaces [157] and digital coding metasurfaces [158]. While analog surfaces provide more freedom in phase tunability, a large range of distinct functionalities can also be realized by digital coding and programmable metasurfaces that usually exploit an FPGA processor to bridge the EM physical world and the digital information world by performing direct modulation on the metasurface interface itself without using any external digital-to-analog (D2A) conversion and/or mixing process [159].

Agile reconfigurability of RISs particularly appeals to the future wireless 6G communication sector where dynamic beamforming and tracking are needed for automotive radar applications, vehicle-to-vehicle (v2v) communication, and satcom globalization [160]. Despite the great promises offered by metadevices as a disruptive technology to the existing antenna architecture, certain challenges still remain to be addressed before they can gain widespread support for commercial deployments. Figure 3.3 provides a high-level comparison between pros and cons of SEM-based metasurfaces versus existing solutions and technologies. In a nutshell, frequency bandwidth limitation is one of the toughest challenges EM metasurfaces currently face due to the resonant nature and frequency dispersive behavior of their building blocks, i.e. their unit cells.

3.4 RIS Modeling Techniques

Covering communication theory, electromagnetism, and computer science, RIS's modeling, analysis, and design for wireless network applications is a multidisciplinary research topic. Ignoring this multidisciplinarity by separating the communication and EM aspects of the problem and assigning an arbitrarily controlled phase profile to RISs, as the vast majority of studies in

communication society have assumed so far, is too much of a simplification. This is because perfect phase prescription may or may not comply with the physics of the problem at hand and thus may lead to unrealizable performance predictions. In fact, the response depends not only on the properties of the designed surface (such as the choice of substrate and the characteristics of the tunable components) but also on the properties of the impinging wave (such as the angle of incidence and polarization) [142].

As far as the response dependency on the incident angle is concerned, RISs are said to be spatially dispersive, meaning that the reflection properties of an EM wave interacting with RIS strongly depend on the incident angle. When it comes to polarization dependency, the behavior of a symmetric surface topology under normal incidence coincides for both TE (Transverse Electric) and TM (Transverse Magnetic) polarizations. However, oblique incidence can, in general, cause polarization dependency in RIS responses and therefore should be analyzed separately. Accounting for mutual interaction/ coupling among adjacent meta-atoms is another important issue that ultimately sets the proposed methods in the literature apart in terms of their analysis complexity, accuracy, and repeatability under different loading conditions. Therefore, the development of an EM-compliant model that is both tractable and low-cost, thereby avoiding heavy computational burdens, is of crucial importance for characterizing and predicting the performance of RISs at the system level.

To set the stage for the remainder of the chapter and to place the mutual coupling discussion in the proper context, infographic 3.4 presents an abstract, high-level classification of the most common RIS modeling approaches reported in the literature to date. It illustrates the progression in modeling abstraction—from the smallest meta-atom scale, to the full beamforming panel, and ultimately to the RIS-assisted wireless propagation scenario involving multiple-input–multiple-output (MIMO) transmitter–receiver antenna pairs. Overview of this section is not intended to be exhaustive, nor is it meant to provide a comprehensive treatment of all listed techniques. Rather, only the methods employed in this study will be discussed in detail, while readers interested in alternative approaches are directed to the cited references. Key aspects of the infographic are summarized in the following subsections.

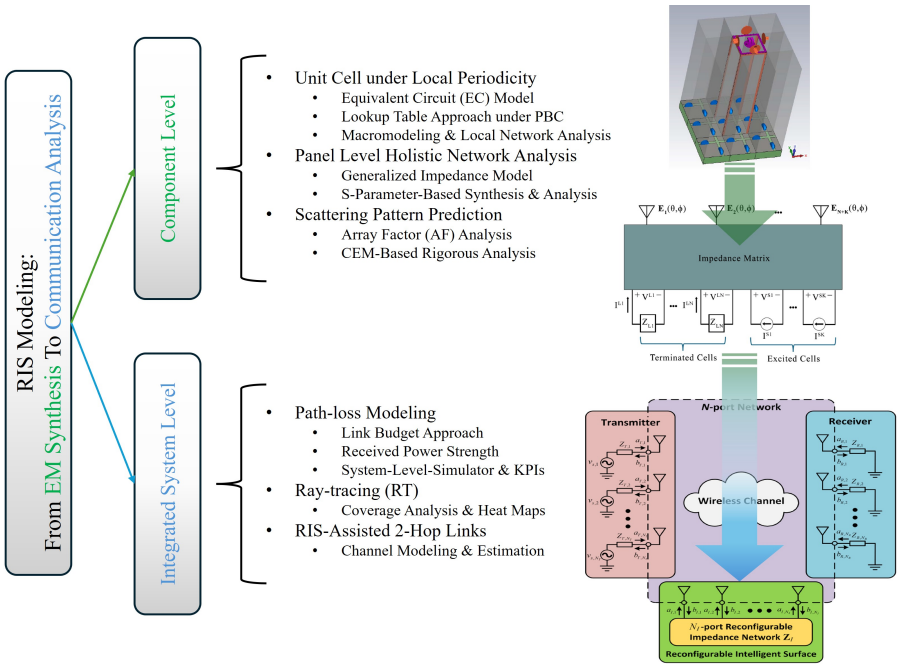

Figure 3.4: RIS modeling infographic.

Local Periodicity

Built upon the concept of periodic boundary condition (PBC), local periodicity (LP) [161] assumes that the characteristics of the elements vary gradually across the surface, thereby justifying the use of a single unit cell response surrounded by an infinite set of identical elements. This way, a database of phases can be created by performing a parametric simulation of the elements under different loading conditions. This is commonly referred to as the 'lookup table' approach through which a correspondence can be established between geometrical surface parameters and the phase response of a particular pixel in the panel. This methodology, in fact, links back to the discussion of homogenization under the Floquet-Bloch theorem as presented in Section 3.1. Moreover, LP can indeed capture a 'coherent' version of mutual coupling [162] among cells since the unit cell is not in a standalone/ isolated configuration but rather embedded in an infinite array of elements all identical to each other,

hence the name coherent. However, as experimentally demonstrated in a recent study [163], the PBC-based modeling and its ensuing lookup-table-based synthesis can lead to pattern predictions that may noticeably deviate from the realistic behavior of a heterogeneous/ disordered panel where there are rapid phase variations in the prescribed phase profile across the surface, e.g., at the location of Fresnel-zone phase wrappings or the surface edge elements.

Local Network Analysis

In the context of RIS modeling, microwave network analyses have recently received a lot of attention. Depending on whether these approaches are applied for analysis at the UC level or the entire panel, they can be categorized into 'local' and 'global' microwave network techniques, of which the former is the subject of this section while the latter will be discussed in the upcoming section. Macroscopic modeling, known also as Macromodeling (MM) for short [164], is a prime example of this family where the standard network analysis is applied to RIS unit cells under local periodicity assumptions. The detailed discussion and formulation of the method are provided in *Paper D* and *Paper E* and therefore will not be repeated here, but rather the salient points of the method are briefly summarized as follows:

- Since it is based on network analysis, MM in theory is more accurate and more versatile than equivalent circuit (EC) based analyses [143], [165] which are based on transmission line theory and face challenges in incorporating oblique incidence and polarization effects in their surrogate models.

- MM separates passive structures, to be handled only once by a full wave analyzer in order to produce the network parameters of a given UC, from active lumped components that can then be analyzed repeatedly later on using a fast circuit analyzer under different loading conditions for RIS beamforming, for instance. This way, MM provides a fast and efficient UC characterization technique, which can also streamline the design process of RIS unit cells as proposed in [166].

- Being PBC-based, MM cannot capture non-coherent mutual coupling effects among cells and thus inherits all the limitations associated with the local periodicity approach discussed in the previous section.

- At the panel level, MM interfaces with the array-factor (AF) framework—discussed in a later section—and consequently inherits its underlying assumptions and limitations when predicting far-field (FF) scattering patterns. As concluded in *Paper D* and *Paper E*, MM-AF-based pattern predictions are satisfactory for main beam predictions, but care needs to be taken when accurate sidelobe predictions are also of concern and importance, as the method may not reliably capture these finer details.

Global Network Analysis

As discussed previously, such local network analyses as Macromodeling can provide viable and fast surrogate models for RISs within their above-mentioned limitations and/or constraints. To harness the full potential of microwave network analysis, however, the finite panel, and not just one unit cell under infinite periodicity assumptions, needs to be considered and analyzed in its entirety so that the complete mutual coupling effects under dynamic beamforming conditions can be fully captured. Moreover, due to overlooking 'non-coherent' intera-cell interactions among aperiodic unit cells, local periodicity cannot in general achieve amplitude control from the synthesis point of view, although it can approximately control the phase of a wavefront [167]. To accurately capture the inter- and intra-cell interactions, another strategy, relying on impedance matrix representation, is proposed in the literature [168], [169]. This hybrid method treats the metasurface as a grid of unit cells, each of which is modeled as a single port, and then uses a commercial FW solver only once to compute the impedance matrix of the entire panel. The method also provides the flexibility to model the metasurface as either a passive reflector or a directly-fed leaky-wave antenna (the importance of the latter is further emphasized under the holographic beamforming framework in *Book Chapter C*).

To provide some background about the network representation of MTSs, let us follow the methodology in [168], where it is supposed that N number of unit cells are terminated by loads and K of them are directly excited. An impedance matrix notation can then be used to express the relationship between the excitations and terminations in the network as follows:

$$\begin{bmatrix} \bar{V}_L \\ \bar{V}_E \end{bmatrix} = \begin{bmatrix} \bar{\bar{Z}}_{LL} & \bar{\bar{Z}}_{LE} \\ \bar{\bar{Z}}_{EL} & \bar{\bar{Z}}_{EE} \end{bmatrix} \begin{bmatrix} \bar{I}_L \\ \bar{I}_E \end{bmatrix} \tag{3.5}$$

where the subscripts E and L denote the excitations and the loads, respectively; $\bar{\bar{Z}}_{LL}$ (an $N \times N$ matrix) represents coupling among the terminated ports; likewise, $\bar{\bar{Z}}_{EE}$ (a $K \times K$ matrix) represents coupling among excitations; and finally, $\bar{\bar{Z}}_{LE}$ and $\bar{\bar{Z}}_{EL}$ are to represent the coupling between terminations and excitations. If the load impedances at each terminated port are plugged into a diagonal matrix $\bar{\bar{Z}}_L$, then the voltages produced by excitations across the loads can be directly related to the load currents and impedances as $\bar{V}_L = -\bar{\bar{Z}}_{LL}\bar{I}_L$. Substituting $\bar{V}_L$ into Equation 3.5 and performing simple mathematical manipulations, one can analytically derive the required impedances needed to achieve a desired radiation pattern as:

$$\bar{\bar{Z}}_L = \left[-\bar{\bar{Z}}_{LE}\bar{I}_E - \bar{\bar{Z}}_{LL}\bar{I}_L\right] \oslash \bar{I}_L \tag{3.6}$$

where the symbol $\oslash$ denotes the Hadamard element-wise division. As can be seen, Equation 3.6 relates the load impedances to the currents at the ports, hence providing a basis for an accurate synthesis technique of the currents to produce desired scattering/ radiation patterns.

Another closely related approach to the generalized impedance method is the scattering parameter network analysis since the impedance matrix $\bar{\bar{Z}}$ can be easily converted to its corresponding scattering matrix $\bar{\bar{S}}$. In fact, S matrices have already been shown to be very effective in accurately characterizing MIMO wireless systems [170], [171], and now their extension to RIS-assisted communication link modeling seems to be a natural and straightforward step to follow [172], [173]. At this point, a brief technical review on S-parameters from microwave engineering textbooks [174], which can also be seen as a concomitant expansion to the Macromodeling formulation discussed before, will facilitate the flow of discussion for the remainder of the chapter. With reference to Figure 3.5(a), if we consider a_1 as the incident voltage wave entering port 1 and b_1 as the subsequent reflected voltage wave, then the reflection coefficient Γ of this 1-port network is simply given by $\Gamma = \frac{Z-Z_0}{Z+Z_0}$ with Z and Z_0 being the input and characteristic impedances of the network, respectively. Next, considering an arbitrary N-port network as illustrated in Fiqure 3.5(b), the concept generalization of the 1-port network's reflection coefficient Γ to $\bar{\bar{S}}$ matrix can be carried out through the vector-matrix notation as $\bar{b} = \bar{\bar{S}}\ \bar{a}$

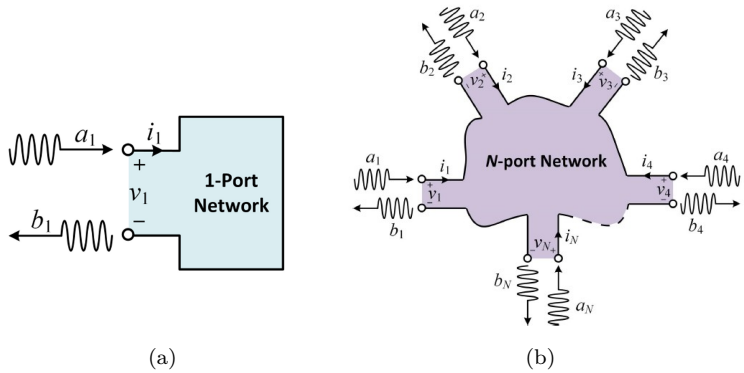

Figure 3.5: (a) 1-port network and (b) its expansion to an N-port network analysis.

where $\bar{a} = [a_1,\ a_2,\ \cdots,\ a_N]^T$ and $\bar{b} = [b_1,\ b_2,\ \cdots,\ b_N]^T$ are now inward- and outward-propagating wave vectors, respectively. Under this generalized matrix notation, the scattering matrix $\bar{\bar{S}}$ can be expressed in terms of the impedance matrix $\bar{\bar{Z}}$ through

$$\bar{\bar{S}} = \left(\bar{\bar{Z}} + Z_0\bar{\bar{I}}\right)^{-1}\left(\bar{\bar{Z}} - Z_0\bar{\bar{I}}\right) \tag{3.7}$$

which for a 1-port network, reduces to the scalar Γ calculated above.

Scattering Pattern Prediction

Before diving into scattering pattern calculations, it will be beneficial to first distinguish between the radiating near-field (Fresnel) and the far-field (Fraunhofer) regions by revisiting some of the standard definitions in antenna engineering textbooks. Although various criteria have been established to identify these regions, the boundaries separating them are not unique. However, according to the discussion in [175], the observation point at r is considered to be in the far-field (FF) if $r \geq 2D^2/\lambda$, where D is the largest dimension of the antenna/ scatterer (in this case RIS). Now assuming this far-zone distance criterion is met, the FF patterns of RIS beamforming panels can be predicted using several methods, among which the array-factor-based (AF-based) approximate techniques and the rigorous computational-electromagnetic-based (CEM-based) techniques stand out in the literature. CEM-based approaches

are the subject of more detailed study in the next chapter and will be treated there, but for now, suffice it to say that they provide the most accurate predictions at the cost of requesting more intensive computational resources. AF-based methods, on the other hand, are less precise but faster and build upon the common wisdom in phased array antenna design and analysis by considering elements of RIS panels as passive scatterers ('2nd-hand' radiators), each contributing their own specific phase-delay to shape and manipulate the scattered wavefront in a prescribed manner.

In mathematical terms, the dominant polarization ($\hat{e}$) of the scattered electric field in the far zone can be expressed as:

$$\boldsymbol{E}^s_{RIS} = \frac{1}{r} e^{-jkr} \boldsymbol{G}(\hat{r}) = \hat{e} \frac{1}{r} e^{-jkr} G(\theta, \varphi) \tag{3.8}$$

where $\boldsymbol{r} = r\hat{r}$ is the position vector, $1/r$ is the divergence factor, e^{-jkr} is the phase factor, and $\boldsymbol{G}(\hat{r})$ is the complex far-field function [176]. Using the pattern multiplication rule [175], the panel's FF function can be written as $G(\theta, \varphi) = G_{element}(\theta, \varphi) \times AF$ with $G_{element}$ and AF being the co-polar dominant component of the FF function of one isolated element and the array factor, respectively. AF is a function of local reflection coefficients (Γ_{mn}) and can be expressed for a rectangular grid of M rows and N columns as follows:

$$AF = \sum_{m=1}^{M} \sum_{n=1}^{N} |\Gamma_{mn}| e^{-j[k(n-1)d_x \sin\theta \cos\varphi + k(m-1)d_y \sin\theta \sin\varphi + \angle\Gamma_{mn}]} \tag{3.9}$$

where d_x and d_y are inter-element spacings in x- and y-directions, respectively. It is noteworthy to mention that instead of reflection coefficient Γ, some studies in the literature [177], [178] have preferred to use the concept of radar cross-section (RCS) ($\sigma^s = \lim_{r\to\infty} 4\pi r^2 |\boldsymbol{E}^s|^2 / |\boldsymbol{E}^i|^2$) to calculate the array factor, which is just a different interpretation yielding comparable results in the end.

System-Level Modeling

A key component of any wireless communication system is the wireless channel, through which radio waves convey signals and information. In propagation channels of realistic large-scale scenarios, it becomes computationally intractable, if not impossible, to obtain analytical solutions for the EM fields through solving Maxwell's equations under appropriate boundary conditions.

In fact, the classic computational EM (CEM) techniques, such as FDTD, FEM, and MoM, which are based on the discretization of integro-differential equations, have to face the challenges of prohibitively large memory requirements and slow computational speed or convergence rate due to the fact that wireless propagation environments are, in most cases, electrically large. Therefore, based on some known system parameters such as operating frequency, terrain characteristics, antenna heights, and other relevant factors, propagation modeling aims to estimate EM fields or signal strength for these large-scale scenarios [179]. A channel model should ideally include not only large-scale and small-scale features of the channel but also the impact of arbitrary array configurations and antenna elements.

A thorough treatment of the methods commonly used for propagation analysis is beyond the scope of the current work, yet the interested readers may find it beneficial to have a short survey on the topic here. Note that a unified notation is not used in this section, but rather the formulas are taken and directly reported as in their respective original studies. To start with, we notice that the propagation models fall within one of the broad families of empirical/ stochastic models and theoretical/ deterministic models. Empirical models, such as Hata-Okumura for urban regions, are widely used and are developed on the basis of extensive field measurements. In the context of path-loss (PL) modeling and large-scale fading for RIS-assisted links, the following empirical model is widely adopted in the wireless community [180]:

$$PL = PL_0 - 10\alpha \log_{10}(\frac{d}{d_0}), \tag{3.10}$$

where PL_0 (for instance, -30 dB) is the path loss at the reference distance d_0 (for example, 1 m). Empirical models are generally simple to use and computationally efficient, while still offering satisfactory accuracy. However, they are typically range-based and remain valid only for environments similar to those from which they were originally derived. Moreover, in the context of MIMO systems, empirical models cannot reliably capture space–time or angle–delay characteristics, which are essential for accurate MIMO channel simulations.

For line of sight (LoS) free-space radio propagation, the simplest theoretical propagation model is the Friis equation [181] which relates the received power (P_r) captured by the receiver (Rx) antenna with an effective area A_{eff} to the transmitted signal power density in a sphere with radius r meters as follows

$$P_r = \frac{P_t G_t}{4\pi r^2} A_{eff} \tag{3.11}$$

where the product of the transmitted power (P_t) and the gain of the transmitter (Tx) antenna (G_t) is usually called effective isotropically radiated power, i.e. EIRP $= P_t G_t$. As stated in [175], [176], A_{eff} can be related to the gain of the receiving antenna G_r and the wavelength λ through $A_{eff} = \frac{\lambda^2}{4\pi} G_r$. Substituting this expression into Equation (3.11) and defining L_s as the free-space path loss, one then gets:

$$P_r = \frac{P_t G_t G_r}{L_s}; \qquad L_s = \left(\frac{4\pi r}{\lambda}\right)^2. \tag{3.12}$$

Modifying the basic Friis equation to account for the 2-hop link between Tx and Rx through an RIS as shown in Figure 3.6(a), Tang et al. [182] proposed the following formula for link budget calculations in terms of local reflection coefficients of a $N \times M$ panel in a virtual LoS RIS-assisted communication:

$$P_r = P_t \frac{G_t G_r G d_x d_y \lambda^2}{(4\pi)^3} \left| \sum_{m=1}^{M} \sum_{n=1}^{N} \frac{\sqrt{F_{n,m}^{combine}}\,\Gamma_{n,m}}{r_{n,m}^t r_{n,m}^r} e^{-jk_0(r_{n,m}^t + r_{n,m}^r)} \right|^2 \tag{3.13}$$

where $F_{n,m}^{combine} = F^{Tx}(\theta_{n,m}^{Tx}, \phi_{n,m}^{Tx}) F^{UC}(\theta_{n,m}^{Tx}, \phi_{n,m}^{Tx}) F^{Rx}(\theta_{n,m}^{Rx}, \phi_{n,m}^{Rx})$ accounts for the effect of $F^{\bullet}$ (the normalized power radiation patterns of Tx, Rx, or the unit cell) on the received signal power. In a similar fashion but by utilizing RCS (σ) of the unit cells instead of their normalized power radiation patterns, Costa et al. [143] reformulated Equation (3.13) to calculate the received signal power in RIS-assisted wireless communications as follows:

$$P_r = \frac{P_t}{(4\pi)^3} \lambda^2 \times \sum_{m=1}^{M} \sum_{n=1}^{N} \frac{G_t(\theta_{n,m}^{Tx}) G_r(\theta_{n,m}^{Rx}) \sigma(\theta_{n,m}^t, \theta_{n,m}^r) |\Gamma_{n,m}|^2 e^{-2j\angle\Gamma_{n,m}} e^{-2jk_0(r_{n,m}^t + r_{n,m}^r)}}{|r_{n,m}^t|^2 |r_{n,m}^r|^2}. \tag{3.14}$$

Borrowing from the power definition of Equation (3.13), later investigations, such as [183] among many other similar studies, defined an end-to-end SISO

channel for a typical RIS-assisted scenario between a base station (BS) and a user equipment (UE), shown in Fiqure 3.6(b). They modeled the UE received signal (r) under additive white Gaussian noise (n) in the familiar format of $r = wx + n$, with w being the cascaded BS-RIS-UE channel expanded as

$$w = \frac{\sqrt{G_r G_u G_t A_r A_u}}{4\pi} \sum_{n=1}^{N_{\text{tot}}} \frac{\sqrt{\tilde{F}_n}\Gamma_n}{r_n^t r_n^r} e^{-jk_0(r_n^t + r_n^r)} \tag{3.15}$$

where N_{tot} is the total number of RIS elements, A_r is the effective aperture area of the TX antenna, $\tilde{F}_n$ is the same as $F_{n,m}^{combine}$ in Equation (3.13) but with linear indexing, i.e. $N_{\text{tot}} = N \times M$, and A_u, G_u are the area and gain of each UC element, respectively. Equation (3.15) can also be written in the compact form of $w = \sqrt{G_r G_u G_t}\,(\mathbf{g} \odot \mathbf{h})^T\, \mathbf{\Gamma}$ where $\mathbf{h} = [h_1, h_2, \cdots, h_{N_{\text{Tot}}}]^T$ with $h_n = \sqrt{A_u F_n^{Tx} F_n^t / 4\pi |r_n^t|^2} e^{-jk_0 r_n^t}$ denotes the channel vector between the BS and the RIS, $\mathbf{g} = [g_1, g_2, \cdots, g_{N_{\text{Tot}}}]^T$ is the LoS channel vector between the UE and all the elements of the RIS with $g_n = \sqrt{A_r F_n^{Rx} F_n^r / 4\pi |r_n^r|^2} e^{-jk_0 r_n^r}$, and $\odot$ stands for Hadamard product.

As one can see from all the theoretical Friis-based equations above, only unobstructed LoS paths in each hop (between BS–RIS and RIS–UE) are considered in Equations (3.13), (3.14), and (3.15) and thus these formulas do not account for the presence of multi-path components. To capture multi-path effects and therefore get a more realistic channel estimate, a more sophisticated deterministic channel modeling, such as ray-tracing (RT), is required. Unlike empirical and theoretical models, RT does not come with simple closed-form formulas but is rather based on ray optics, which solves Maxwell's equations under high-frequency approximation in a fast and memory-efficient manner. During recent years, RT has evolved and turned into a popular propagation modeling tool for obtaining deterministic, site-specific channel models [184], [185], [186] that can provide estimates of path loss, angle of arrival/departure, and time delays. For instance, assuming that the complex channel gains (β_n) and angles of departure (θ_n^T) and arrival (θ_n^R) for N_A significant paths between an N_T-element TX array and N_R-element RX array are provided by a ray-tracer, Wallace and Jensen [170] formulated a simple two-dimensional (azimuthal plane at a fixed ϕ) single-polarization path-based channel model for a MIMO communication system as follows:

$$V_i^R = \sum_{j=1}^{N_T} \sum_{n=1}^{N_A} E_i^R(\theta_n^R)\ \beta_n\ e_j^T(\theta_n^T)\ I_j^T \tag{3.16}$$

where V_i^R is the voltage on the i^{th} receive element, $E_i^R(\theta^R)$ is the reception pattern of the i^{th} receive antenna, $e_j^T(\theta^T)$ is the transmitted field per unit excitation current of the j^{th} transmit antenna in the direction of θ^T and I_j^T is the transmit excitation current applied at the j^{th} antenna terminal. As another RT integration example in the link budget calculations, Zhao et al. [185] expanded Equation (3.16) to a dual-polarized (with vertical $\bullet^V$ and horizontal $\bullet^H$ components) MIMO system by formulating the channel transfer function between TX antenna m and RX antenna n ($H_{m,n}(f)$) in a 2D azimuthal plane as follows:

$$H_{m,n}(f) = \sum_{l=1}^{N_A} \begin{pmatrix} G_{r,n}^V(\theta_l^R) & G_{r,n}^H(\theta_l^R) \end{pmatrix} \begin{pmatrix} a_{l,m,n}^{VV} & a_{l,m,n}^{VH} \\ a_{l,m,n}^{HV} & a_{l,m,n}^{HH} \end{pmatrix} \begin{pmatrix} G_{t,m}^V(\theta_l^T) \\ G_{t,m}^H(\theta_l^T) \end{pmatrix} e^{-j2\pi f \tau_l} \tag{3.17}$$

where $G_{t/r}^{V/H}$ are vertical/horizontal components of TX/RX complex antenna gains and a_l and τ_l are the complex amplitude and time delay of the plane wave l, respectively. These earlier studies on RT-based channel modeling have paved the way for system-level RIS simulations and have recently been integrated into a hybrid framework for RIS analysis and optimization [187], [188].

3.5 Beamforming Techniques

To ensure a sufficient link budget, modern cellular systems rely on beamforming to combat path loss and severe shadowing, especially at mmWave range. Beamforming—the process of shaping and directing electromagnetic waves to optimize signal quality, coverage, and spectral efficiency—is also central to RIS functionality. In fact, the primary motivation for RIS beamforming lies in its ability to dynamically manipulate the wireless environment, thereby enhancing signal coverage, mitigating interference, and improving energy and spectral efficiency. For instance, codebook-based beamforming strategies, which utilize predefined sets of beam patterns or transformation matrices, allow for fast adaptation and reduced computational overhead in practical deployments

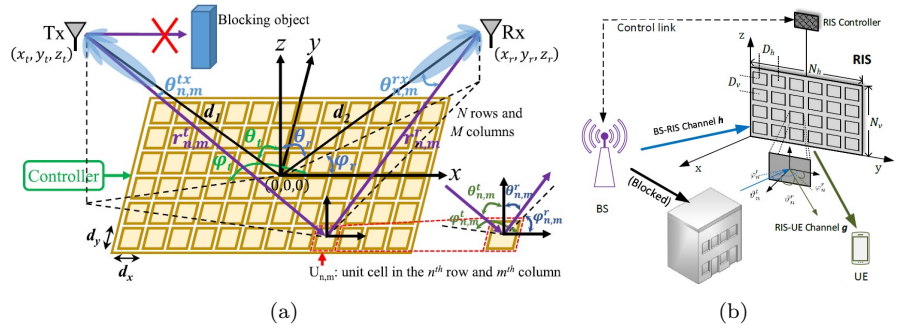

Figure 3.6: Illustrations of a SISO RIS-assisted scenario used for (a) link budget calculation and (b) end-to-end channel modeling (Figures are taken and reprinted from [182] and [183]).

[189], [190]. These methods are especially useful in scenarios with quantized phase shifts or massive RIS arrays, where exhaustive optimization is infeasible [190].

In addition to codebook-based strategies, a rich landscape of RIS beamforming techniques has been proposed in the literature, among which the generalized law of reflection (GLR) [43] and holographic beamforming [191] stand out. The underlying formulation behind these two techniques under plane wave (PW) illumination in far-field is quite similar and can be cast into the same framework of generalized Snell's law as depicted in Figure 3.7 and elaborated briefly upon in the following subsections.

Generalized Law of Reflection

Unlike conventional relay or massive MIMO systems, RIS can operate with minimal power consumption and hardware complexity, leveraging passive or semi-passive elements to control the phase, amplitude, and polarization of incident electromagnetic waves. These elements allow for phase profile engineering on RIS surfaces and hence lead to the idea of reconfigurability and beamsteering. As a generalization of Snell's law, GLR is one of the popular RIS beamforming techniques first introduced in the optics community to incorporate surface phase profile at a given interface between two media, as

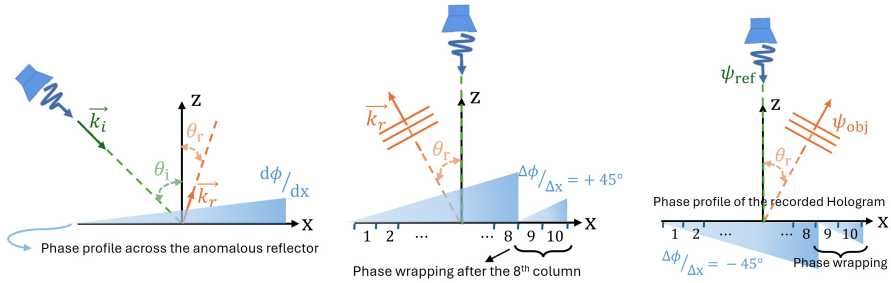

(a) (b) (c)

Figure 3.7: Beamforming techniques under PW illumination. (a) The general concept behind the non-specular reflection from an anomalous reflector with a prescribed linear phase progression $d\phi/dx$ along the x-axis. (b) and (c) Representative examples of column-wise beamforming for a panel consisting of 10 columns and an 8-state phase discretization scheme $\pm 45°$ to reflect and steer a normal incident PW away from the broadside and onto $\mp 30°$ under GLR and Holographic beamforming techniques, respectively.

depicted in Figure 3.7(a). Considering a time-harmonic case with its positive time convention $e^{j\omega t}$ suppressed, GLR reads:

$$\sin\theta_i - \sin\theta_r = \frac{\lambda_0}{2\pi}\frac{\mathrm{d}\varphi}{\mathrm{d}x} \tag{3.18}$$

where $\mathrm{d}\varphi/\mathrm{d}x$ is a surface phase gradient along the x-axis, λ_0 is the free-space wavelength, and θ_i, θ_r are the incident and reflected angles, respectively. If there is no phase progression along the surface, i.e. $\mathrm{d}\varphi = 0$, then Equation (3.18) reduces to the familiar Snell's law of reflection which indicates a specular reflection with $\theta_r = \theta_i$. Non-specular reflections with $\mathrm{d}\varphi/\mathrm{d}x = \text{const.} \neq 0$, on the other hand, can be interpreted as two distinct PW contributions as follows:

$$\mathrm{d}\varphi = k_0 \mathrm{d}x \sin\theta_i - k_0 \mathrm{d}x \sin\theta_r \tag{3.19}$$

where the first term $k_0 \mathrm{d}x \sin\theta_i$ is there to steer an interim beam to the broadside by compensating for the phase differences induced among cells due to

incident PW illumination, while the second term $k_0 \mathrm{d}x \sin\theta_r$ is responsible for steering this interim beam away from the broadside and onto the final desired beam direction of θ_r. As a simple example, let us consider Figure 3.7(b) in which a 10-column RIS panel with the column width of $\Delta x = \lambda_0/4$ has a 3-bit (8 states) discretized phase step of $\Delta\varphi = +45°$. Under these operating conditions, the panel will reflect a normally incident PW ($\theta_i = 0$) to the reflection angle of $-30°$, i.e.

$$0 - \sin\theta_r = \frac{\lambda_0}{2\pi}\frac{\pi/4}{\lambda_0/4} \quad \Rightarrow \quad \theta_r = \arcsin(-\frac{1}{2}) = -30°.$$

This is a typical analysis case which is the opposite process to its corresponding synthesis task where a designer is asked to come up with a proper phase profile ($\Delta\varphi$) given the information about θ_i, θ_r and perhaps $\Delta x/\lambda_0$.

Holographic Beamforming

Holographic beamforming leverages the principles of electromagnetic holography to engineer complex aperture responses on RIS or metasurfaces [192]. By recording and reconstructing the interference patterns of reference ψ_{ref} and object ψ_{obj} waves, holographic RIS can form highly directive beams, focus energy at specific locations, and support multi-beam transmission. This approach is particularly promising for near-field communications, integrated sensing, and wave-domain analog computing, where conventional phased-array methods are insufficient [193]. Detailed explanation about the technique can be found in *Book Chapter C* and references therein and therefore will not be repeated here. It is, however, beneficial to cast the technique into the generalized Snell's framework of Figure 3.7 under PW illumination to see the similarities between the two beamforming techniques discussed in this section.

Let ψ_{ref} be the dominant electric field component of a linearly polarized incident PW and similarly ψ_{obj} be the dominant electric field component of the reflected waveform in the desired direction θ_r. From engineering electromagnetic textbooks, one can express $\psi_{ref} \propto e^{-j\boldsymbol{k}_i\cdot\boldsymbol{r}}$ and $\psi_{obj} \propto e^{-j\boldsymbol{k}_r\cdot\boldsymbol{r}}$ with the symbol $\propto$ denoting proportionality, $\boldsymbol{k}_i = k_0[\sin\theta_i\hat{x} - \cos\theta_i\hat{z}]$, and $\boldsymbol{k}_r = k_0[\sin\theta_r\hat{x} + \cos\theta_r\hat{z}]$. From the holographic recording and reconstruction stages discussed in *Book Chapter C*, we know that the recorded hologram should be in the form of $\psi^*_{ref}\psi_{obj}$ so that upon illumination with ψ_{ref}, the synthesized hologram reproduces a replica (scaled version) of the ψ_{obj}, i.e. $\psi_{ref}(\psi^*_{ref}\psi_{obj}) =$

$|\psi_{ref}|^2\psi_{obj}$. Now given the above PW proportionalities in the far-field, one can easily show that $\psi^*_{ref}\psi_{obj} \propto e^{+jk_0[x\sin\theta_i - z\cos\theta_i]}e^{-jk_0[x\sin\theta_r + z\cos\theta_r]}$. Finally, phase matching condition on the hologram's surface dictates that the phase of the tangential waves (surface waves along $\hat{x}$ direction in this example) be equal as follows:

$$\angle\text{Hologram}|_{\tan} = \varphi = k_0 x[\sin\theta_i - \sin\theta_r] \tag{3.20}$$

which is another interpretation of GLR in Equation (3.18) and can be rephrased to the same form of $\sin\theta_i - \sin\theta_r = {}^{\mathrm{d}\varphi}/_{k_0\mathrm{d}x}$. As an example, Figure 3.7(c) shows the same panel under normal incident PW illumination as in the GLR example but for a beamforming case with a negative phase slope of $-45°$ leading to the reflection angle of $+30°$.

3.6 Illustrative Examples

Summarizing the most salient features of *Paper D*, this short section tends to provide pragmatic examples for some of the algorithms listed in infographic 3.4 from UC characterization under PBC and AF-based pattern synthesis to local network analysis and Macromodeling applied to coding metasurfaces.

Modified Unit Cell Structure

As discussed earlier, the conventional design approach for periodic and quasi periodic structures is to focus on a single cell analyzed under periodic boundary conditions. In this framework, the unit cell (UC) is assumed to reside within an infinite array of identical meta-atoms, all operating in the same state. As the name implies, unit cells form the fundamental building blocks of RIS panels. A metasurface panel is essentially an arrangement of these UCs in an array configuration tailored to a specific application. Consequently, the overall behavior of the panel is governed not only by the collective interactions among its constituent cells but also by the intrinsic characteristics inherited from the UC design itself. Developing a new UC design was not pursued in this study, as such an effort constitutes a broad research topic on its own and requires extensive analysis supported by substantial design experience and intuition. Instead, a comprehensive literature survey was conducted to pick up a design that properly serves the intended application by exhibiting stable

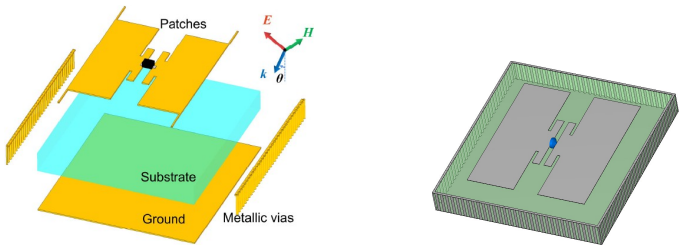

(a) (b)

Figure 3.8: Adopted Unit Cell: (a) the original design taken and reprinted from [194] (b) its modified version employed in this study.

characteristics for wireless communication links at the sub-6 GHz frequency range.

The design proposed by Liang et al. [194] and depicted in Figure 3.8(a) was a promising candidate because it not only provides an almost full range of continuous phase control ($\sim 330°$), but its utilization of via fences makes the design angle-insensitive to a good extent. The design parameters are, therefore, exactly the same as those adopted from the original study and are not repeated here for the sake of brevity. To further improve the angular robustness of the meta-atoms, the original design was, however, slightly modified by extending the metallic via fences around the entire perimeter, thereby fully enclosing the UC. The modified design, shown in Figure 3.8(b), has its resonance frequency shifted downward to 3.1 GHz compared to 3.15 GHz of the original design and at the same time enables the possibility of applying the domain decomposition technique [195] to model the UC as an open cavity as outlined in Chapter 4.

Figure 3.9 presents the EC analysis of the original design performed in ADS®. As can be seen from the typical 'S-curve' behavior of its reflection coefficient (Γ) under different Varactor loadings in the range of $[0.6,\ 1.5]$ pF, the UC exhibits a relatively narrow resonance frequency bandwidth centered around 3.15 GHz with a reasonable loss of magnitude (< 1 dB) and a wide phase change coverage ($[-180°,\ 150°]$). A 3-bit discretization scheme along with its corresponding 8 capacitor values is also shown in the subplot 3.9(c) as a function of frequency.

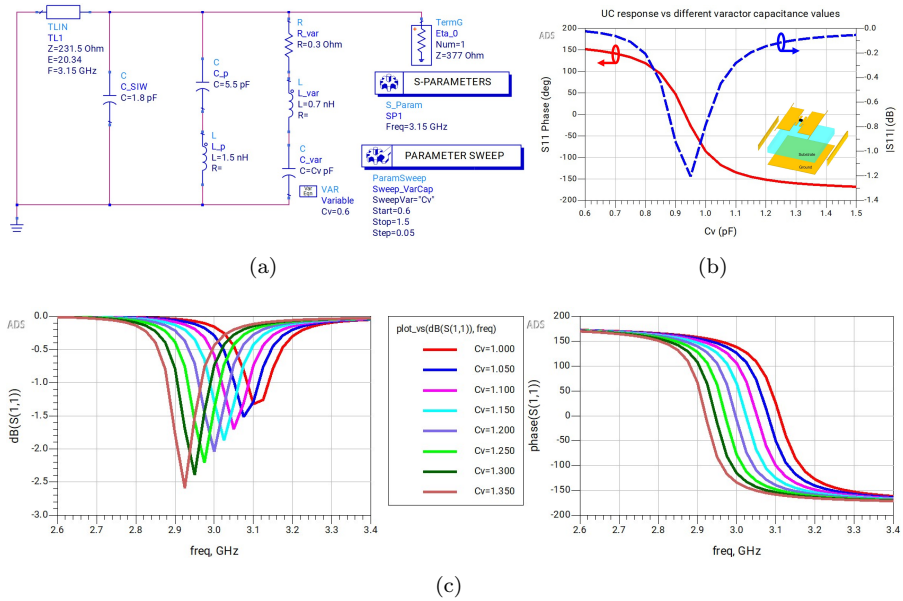

Figure 3.9: Equivalent circuit (EC) analysis of the original design performed in ADS® with (a) EC schematic showing the varactor as a series RLC circuit with variable capacitance c_v (b) the UC reflection coefficient response (S_{11} or equivalently Γ) at 3.15 GHz under different loading conditions and (c) the $|\Gamma|$ and $\angle\Gamma$ as a function of frequency.

A similar parametric sweep analysis was also carried out on the modified UC design as shown in Figure 3.10. The reflection coefficient response of the fully caged UC at the center frequency of 3.1 GHz, shown in both Cartesian and polar formats in the subplots, indicates a Lorentz-like resonance behavior for varactor values between 1–1.2 pF and an almost full angular response coverage with a negligible loss of amplitude.

Beamsteering Case Studies

This subsection provides a handful of simulation results to showcase the typical GLR and holographic beamforming use cases. To start with, the conceptual GLR beamforming scenario of Figure 3.7(b), dubbed as 'validation case' here,

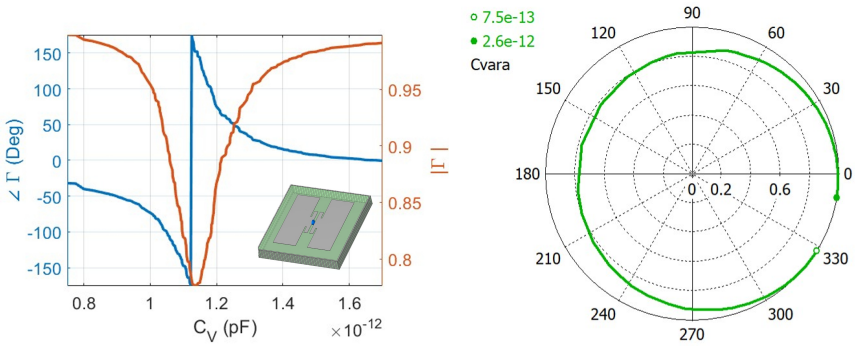

(a) (b)

Figure 3.10: Modified UC response under different varactor loadings in (a) Cartesian and (b) polar formats.

was realized using 100 modified UC elements of Figure 3.8(b) arranged in a 10×10 rectangular grid. Note that although quite close, the lateral size of the UC in the x-direction is not exactly $\lambda_0/4$ at the center frequency of 3.1 GHz, and that is the reason why the phase progression depicted in Figure 3.11(a) is not exactly 45°. In any case, by using the UC's look-up table of Figure 3.10(b), the prescribed phase profile was then mapped to the corresponding Varactor capacitances, as reported in Figure 3.11(b). To validate the beamsteering capability of the panel as well as the accuracy of the beamforming synthesis technique, the whole panel with these modulated C_v values was simulated under PW illumination using the frequency domain (FD) solver of CST, whose proper mesh setting and convergence are thoroughly discussed in *Paper D*. As can be seen from Figure 3.11(d), the main beam of the panel under this column-wise Varactor configuration and GLR beamforming points to $-27.5°$ instead of the desired $-30°$ set as the ultimate goal at the beginning of the synthesis problem. This small discrepancy can be attributed to all the approximations made through PBC and the look-up table beamforming procedure discussed earlier in this chapter.

Two more representative examples of the same 10×10 panel, beamformed to accommodate different purposes, are presented in Figure 3.12. Shown in the first subplot is the reciprocal scenario to the aforementioned validation

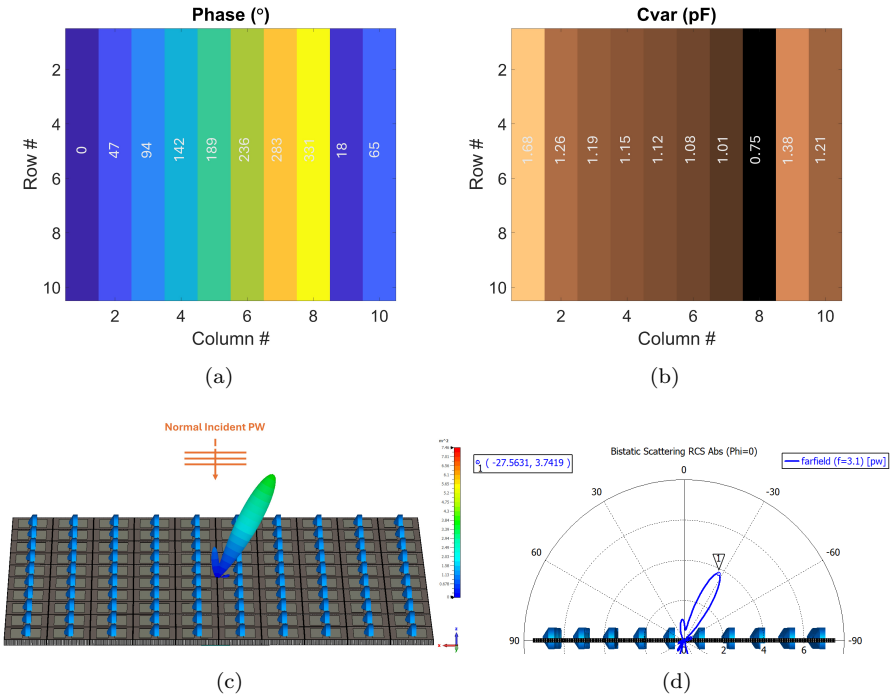

Figure 3.11: Beamforming results of a 10×10 RIS panel composed of the modified unit cell from Figure 3.8(b). (a) Column-wise phase profile for the validation case (normal to $-30°$ scenario of subplot 3.7(b)) synthesized using GLR. (b) Corresponding varactor values mapped from the prescribed phase profile using the lookup table of Figure 3.10(b). (c) and (d) CST full wave simulation results of the panel's scattering pattern in 3D and in the 2D E-plane cut, respectively.

case where the incident and desired angles are now swapped. As can be seen, the incoming wave from $-30°$ azimuthal angle is reflected in a direction perpendicular to the panel and hence towards the broadside, which confirms the angular reciprocity for this case. The second subplot is to showcase a niche application of the retro-reflection concept widely adopted in Van Atta arrays for backscatter communications and/or integrated sensing and communications (ISAC) [196]. As can be seen from the CST simulation result, the beamformed

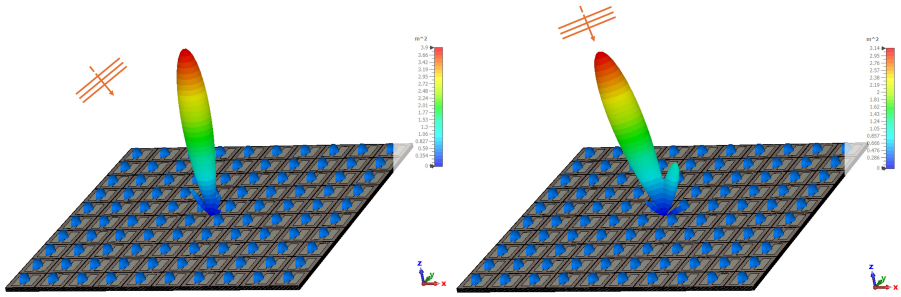

(a) (b)

Figure 3.12: Beamforming case studies under GLR for (a) Angular reciprocity of the validation case and (b) Retro-reflection.

panel (whose beamforming details, such as phase profile and varactor values for this case, are spared and not reported for the sake of brevity) is also successful in producing a retro-directive response by sending energy back toward the incident PW direction.

When it comes to holographic beamforming, a 'frozen' patch model at 10 GHz borrowed from [197] is simulated and reported in *Book Chapter C* for a simple SISO beamforming scenario, details of which will not be repeated here. Interested readers should consult these references for more information about the UC geometric dimensions and its look-up table. To complement this topic, however, a SIMO scenario is considered here, where the patch-based panel is illuminated by a single horn antenna from its broadside and beamformed to serve two users at different elevational angles of 20° and 50° in the 45° azimuthal plane. The size of the panel's constituent patches is varied to form the phase profile of the hologram needed to reflect and split a single normally incident beam (ψ_{ref}) into ψ_{obj1} at (20°, 45°) and ψ_{obj2} at (50°, 225°) directions as depicted in Figure 3.13. Note that the recorded hologram in this case needs to account for the superposition of these two object waves and hence reads: $\psi^*_{ref}(\psi_{obj1} + \psi_{obj2})$. The simulation result in the 45°-plane of Figure 3.13(b) shows that most of the reflected energy is successfully guided toward the target directions, although the reflected beam is not split evenly and the power distribution ratio between these two branches needs to be further engineered as well. As stated, these examples were for frozen patch-based holograms; for

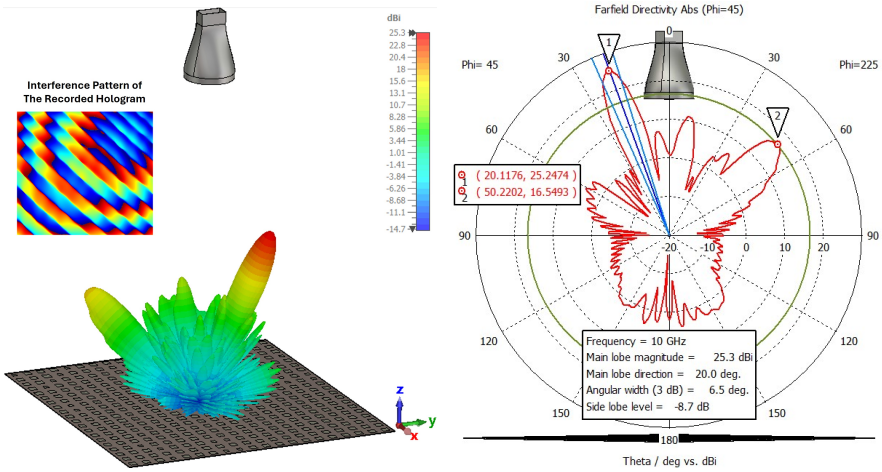

(a) (b)

Figure 3.13: Holographic SIMO Beamforming with the desired reflection angles of $(\theta,\ \varphi) = (20^\circ,\ 45^\circ)$ and $(50^\circ,\ 225^\circ)$, and the scattering pattern of the synthesized frozen panel shown in (a) 3D (with the phase profile of the recorded hologram included in the inset) and (b) 2D 45°-plane cut.

holographic beamforming of a non-frozen (reconfigurable) panel, readers are referred to the Varactor-based SISO example reported in *Paper D*.

MM on Coding Metasurfaces

The 'coding metasurface' paradigm, introduced by Cui et al. [198] in 2014, forges a direct connection between metasurface engineering and information science, enabling metasurfaces to be treated as digitally addressable platforms rather than purely analog materials. In lieu of describing material properties continuously, this approach encodes local geometry, constitutive parameters, and electromagnetic responses (phase, amplitude, polarization) into discrete symbols—commonly binary digits—so that metasurface behavior can be represented and manipulated using digital sequences.

A crucial consequence of this digital representation is that metasurfaces

can leverage many tools and algorithms from digital signal processing, opening design possibilities that were previously confined to electronic and software domains. Practical implementations often incorporate switching elements (for example, diodes) into each meta-atom; these components allow individual elements to toggle among a set of discrete states, thereby making the metasurface reconfigurable or even programmable. When such switching is combined with time-varying control, the platform can realize advanced space–time coding schemes that jointly shape spatial and spectral field properties [158].

Despite their discretized nature, coding metasurfaces have demonstrated powerful field-shaping capabilities in practice, enabling functions such as multi-beam modulation [199], holography [200], [201], and orbital angular momentum (OAM) beam coding [202]. A simple illustrative encoding maps binary digits to phase states—for instance, "0" and "1" may correspond to phase shifts of 0° and 180°, respectively—yet far richer behaviors become possible when multiple states, dynamic modulation, and algorithmic control are employed.

To wrap up this brief discussion on coding metasurfaces, two representative examples are simulated in CST and their results are compared against Macro-modeling. Figure 3.14 shows the simulation results under normal illumination of two coding metasurfaces, which are rectangular 10×16 Varactor-based panels with the following two coding sequences (CS), CS1 : "0000222244446666" and CS2 : "0022446600224466" as shown in the insets of their corresponding plots. Note that 0, 2, 4, and 6 are the four discrete coding states corresponding to reflection phases of 0°, 122°, 165°, and 265°, respectively. MM was also applied to predict the scattering patterns of the panels and shows good agreement with FW results, especially when it comes to main beam predictions.

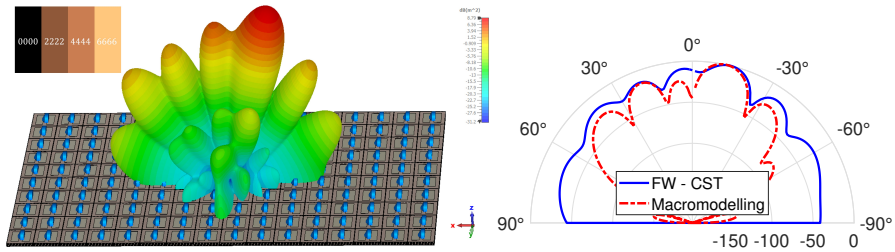

(a) Coding Sequence 1 (b) Coding Sequence 1

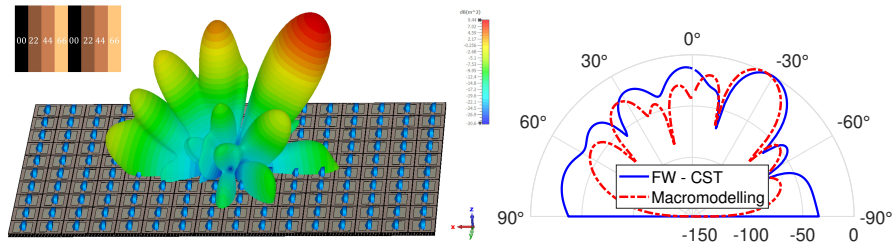

(c) Coding Sequence 2 (d) Coding Sequence 2

Figure 3.14: Two representative examples of coding metasurfaces for beamsteering away from broadside and onto negative elevation angles in the X-Z plane. (a) and (c) 3D patterns of the coding sequences 1 and 2, respectively, simulated and exported from CST. (b) and (d) 2D cut comparisons between full-wave and MM scattering pattern predictions for the two sequences.

CHAPTER 4

SEM: Domain Decomposition Method for RIS Analysis

Quasi-periodic structures have attracted considerable interest for applications such as reflectarrays (RAs), holographic leaky-wave antennas, and RISs, as noted in the previous chapter. Embedding full-wave solvers directly into the design and optimization loop for these architectures remains challenging, however, because their multi-scale nature and the large element counts typical of array implementations lead to prohibitive computational cost. To manage this complexity, design practice has historically relied on simplifying approximations. Early work treated elements in isolation, neglecting interactions with neighbors [203], [204], while later approaches adopted periodic boundary condition (PBC) models that assume an infinite lattice of identical elements [47], [205], [206]. Although PBC-based methods improve on isolated-element models, they still fail to capture important quasi-periodic phenomena such as the non-negligible mutual coupling between adjacent elements. This has motivated recent studies to further investigate the quantification of design errors introduced by these effects.

At the same time, the long continuum of efforts for the development of efficient computational electromagnetic (CEM) tools has paved the way for researchers to further conduct error quantization studies on quasi-periodic ef-

fects. In this spirit, the present chapter supplies the mathematical foundations and numerical tools underlying the CEM-based method introduced in *Paper E*. The method (a) quantifies the impact of over-the-air mutual coupling on scattering-pattern predictions for an open-cavity RIS panel and (b) benchmarks those predictions against the macromodeling approach described in Section 3.4. The proposed technique separates interior cavity domains from the exterior radiation region and employs a domain-decomposition method (DDM) [195], [207] to couple a commercial full-wave solver (CST Microwave Studio Suite®) for the internal regions with an in-house method-of-moments (MoM) solver for the external field computation. The resulting hybrid scheme is referred to throughout the chapter as H-DDM.

4.1 Mathematical Background

This section serves as a short summary of the principal relations and mathematical notation used throughout the chapter and in *Paper E*. Throughout the chapter, $\boldsymbol{r}'$ denotes a point in the source domain. Moreover, the wavenumber and intrinsic impedance of a medium with material constitutive parameters of (ε, μ) are represented by $k = \omega\sqrt{\mu\varepsilon}$ and $\eta = \sqrt{\mu/\varepsilon}$, respectively.

Integro-Differential Formulation of EM Fields

In any region of space for which $\boldsymbol{E}$ and $\boldsymbol{H}$ are differentiable, the EM fields satisfy Maxwell's curl equations as follows:

$$\boldsymbol{\nabla} \times \boldsymbol{E} = -j\omega\mu\boldsymbol{H} - \boldsymbol{M} \tag{4.1a}$$

$$\boldsymbol{\nabla} \times \boldsymbol{H} = j\omega\epsilon\boldsymbol{E} + \boldsymbol{J} \tag{4.1b}$$

where $\boldsymbol{J}$ and $\boldsymbol{M}$ are electric and magnetic current densities, respectively. The common practice for solving wave equations is to express the EM fields in terms of auxiliary potential functions $\boldsymbol{A}$ and $\boldsymbol{F}$ by separating integral operators from differential operators as shown and labeled as 'Path 2' in Figure 4.1. While this two-step procedure often simplifies the solution of most problems, the one-step formulation of Figure 4.1 labeled as 'Path 1' is most convenient for aperture problems and hence adopted here. Note that the factor $\frac{e^{-jkR}}{4\pi R}$ in the figure's formulation is the free-space Green's function $G(\boldsymbol{r} - \boldsymbol{r}')$, where

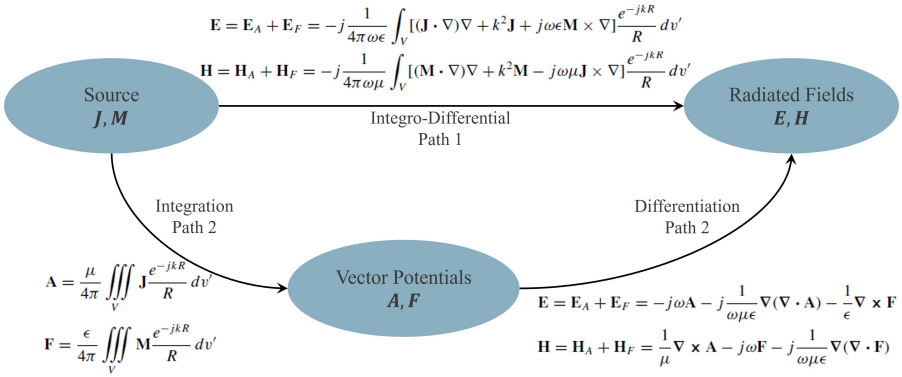

Figure 4.1: Block diagram of radiated EM field computations from electric and magnetic sources (the inspiration and formulations come from [175]).

$R = |\boldsymbol{r} - \boldsymbol{r}'|$ with $\boldsymbol{r}$ and $\boldsymbol{r}'$ being the position vectors to observation and source points, respectively.

For the surface integral operations which are to be performed in the rest of the chapter on surface current distributions ($\boldsymbol{J}_s$, $\boldsymbol{M}_s$) over an aperture S with a normal unit vector $\hat{\boldsymbol{n}}$, it is favorable to put the direct formulation of 'Path 1' into a compact operator notation as follows:

$$\boldsymbol{E} = \boldsymbol{E}(\boldsymbol{J}_s) + \boldsymbol{E}(\boldsymbol{M}_s) \quad \text{and} \quad \boldsymbol{H} = \boldsymbol{H}(\boldsymbol{J}_s) + \boldsymbol{H}(\boldsymbol{M}_s) \tag{4.2}$$

with

$$\boldsymbol{E}(\boldsymbol{J}_s) = \mathcal{L}(\boldsymbol{J}_s), \qquad \boldsymbol{H}(\boldsymbol{M}_s) = \frac{1}{\eta^2}\mathcal{L}(\boldsymbol{M}_s) \tag{4.3}$$

and

$$\boldsymbol{E}(\boldsymbol{M}_s) = -\mathcal{K}(\boldsymbol{M}_s) + \frac{1}{2}\hat{\boldsymbol{n}}\times\boldsymbol{M}_s, \qquad \boldsymbol{H}(\boldsymbol{J}_s) = \mathcal{K}(\boldsymbol{J}_s) - \frac{1}{2}\hat{\boldsymbol{n}}\times\boldsymbol{J}_s \tag{4.4}$$

where the operators $\mathcal{K}$ and $\mathcal{L}$ on any given input kernel $\boldsymbol{X}$ are defined as the following integro-differential operators [208]:

$$\mathcal{K}(\boldsymbol{X}_s) = \int_S \boldsymbol{X}_s(\boldsymbol{r}') \times \boldsymbol{\nabla}' G(\boldsymbol{r} - \boldsymbol{r}') \mathrm{d}S', \tag{4.5a}$$

$$\mathcal{L}(\boldsymbol{X}) = -j\omega\mu \int_S \boldsymbol{X}_s(\boldsymbol{r}') G(\boldsymbol{r} - \boldsymbol{r}') \mathrm{d}S' + \frac{1}{j\omega\varepsilon} \boldsymbol{\nabla} \int_S \boldsymbol{\nabla}' \cdot \boldsymbol{X}(\boldsymbol{r}') G(\boldsymbol{r} - \boldsymbol{r}') \mathrm{d}S'. \tag{4.5b}$$

Furthermore, the scalar Green's function for a homogeneous medium is

$$G(\boldsymbol{r} - \boldsymbol{r}') = \frac{e^{-jk|\boldsymbol{r}-\boldsymbol{r}'|}}{4\pi|\boldsymbol{r} - \boldsymbol{r}'|} = \frac{e^{-jkR}}{4\pi R}. \tag{4.6}$$

The above formulation would not be complete without mentioning a set of proper boundary conditions (BCs) for it. Considering S as a surface between two regions, a and b as depicted in Figure 4.2(a) with its normal unit vector $\hat{\boldsymbol{n}}$ pointing into region a, the set of boundary conditions for the electric surface current ($\boldsymbol{J}_s$) and magnetic surface current ($\boldsymbol{M}_s$) on S can be written as:

$$\boldsymbol{J}_s = \hat{\boldsymbol{n}} \times (\boldsymbol{H}^a - \boldsymbol{H}^b), \qquad \boldsymbol{M}_s = (\boldsymbol{E}^a - \boldsymbol{E}^b) \times \hat{\boldsymbol{n}}. \tag{4.7}$$

Equivalence Theorem

Huygens' principle states that every point on a primary wavefront can be considered as a secondary source emitting spherical waves, and thus a secondary wavefront can be constructed as the envelope of these secondary spherical waves. As a formal, rigorous extension of Huygens' idea, Schelkunoff introduced the concept of field equivalence in 1936. The equivalence principle builds upon the uniqueness theorem which allows for the construction of EM field solutions inside a region solely from the tangential field components specified on that region's boundary [175]. This property is useful for decomposing a complex scattering problem into smaller subproblems, each tied to a distinct spatial region. Under this regime, the coupling between regions is enforced by prescribing the tangential fields on their shared interfaces. For practical implementation, those tangential boundary fields are interpreted as equivalent sources that reproduce the same external field [176].

Depending on use cases, the equivalent model can be constructed differently to serve a specific family of applications. For instance, Love's theorem is

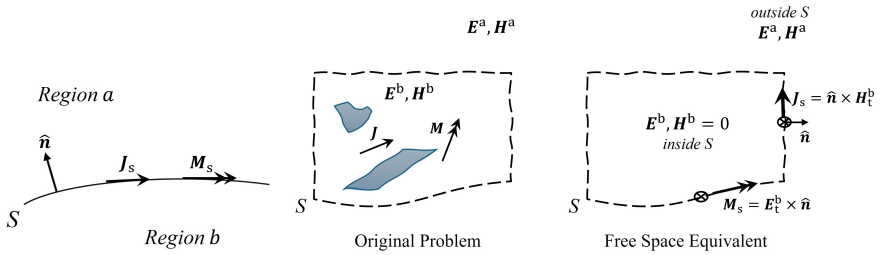

(a) Tangential BCs (b) Love's Theorem

Figure 4.2: EM theorems and principles. (a) A boundary surface S between regions a and b. (b) Free-space equivalent of a field problem (single-headed arrows denote electric current while double-headed arrows represent magnetic current; subscripts s and t stand for surface quantity and tangential component, respectively).

well suited to aperture problems such as horn and reflector antennas. Love's equivalence principle of Figure 4.2(b) produces a null field within the imaginary surface S. In other words, the current densities are selected so that the fields inside the closed surface are zero and outside they are equal to the radiation produced by the actual sources. For convenience and numerical efficiency, the enclosing surface is often chosen to coincide largely with conducting parts of the structure. This is preferred because the vanishing of the tangential electric field components over the conducting parts of the surface reduces the physical limits of integration.

Method of Moment

As stated in the previous subsection, equivalent sources can be used to formulate field problems. To determine these equivalent sources, integral equations need to be solved which are a direct result of enforcing field continuities across the boundaries of the original problem, i.e. at the locations where we want to introduce the equivalent sources. Among numerous CEM techniques, the method of moments (MoM) [209], [210] is a convenient choice for solving such integrals and has been intensively investigated in the literature. To summarize the key points of the method, let us follow the procedure in [176] by

considering a simple MoM formulation here based on the electric field integral equation (EFIE) enforced onto a PEC surface S as follows:

$$\boldsymbol{E}_t^i(\boldsymbol{r}) + \boldsymbol{E}_t^s(\boldsymbol{r}) = 0, \qquad \boldsymbol{r} \in \boldsymbol{r}_s \tag{4.8}$$

which states that the tangential component of the total field (summation of the incident field $\boldsymbol{E}^i$ and the scattered field $\boldsymbol{E}^s$) is zero on the PEC surface S. The quantity $\boldsymbol{E}^i(\boldsymbol{r})$ is a known incident field, and using EFIE, the scattered electric field can be expressed in terms of an unknown induced current distribution ($\boldsymbol{J}(\boldsymbol{r}')$) on S as:

$$\boldsymbol{E}^s(\boldsymbol{r}) = \int_{S'} \boldsymbol{J}(\boldsymbol{r}') \cdot \overline{\boldsymbol{G}}(\boldsymbol{r}, \boldsymbol{r}')\mathrm{d}s' \tag{4.9}$$

where $\overline{\boldsymbol{G}}$ is the dyadic Green's function of the field problem.

The ultimate goal of solving Equation (4.9) is to determine $\boldsymbol{J}(\boldsymbol{r}')$ which can be expanded in M basis functions $\boldsymbol{B}_m(\boldsymbol{r}')$ as $\boldsymbol{J}(\boldsymbol{r}') = \sum_{m=1}^{M} I_m \boldsymbol{B}_m(\boldsymbol{r}')$, where I_ms are unknown coefficients to be determined. Different types, including entire or sub-domain basis functions, can be selected but it is important to keep in mind that a judicious selection of basis functions, depending on how well they can represent the major physical characteristics of the current distribution of the problem at hand, can make the convergence of MoM solutions faster and more straightforward. Inserting $\boldsymbol{J}(\boldsymbol{r}')$ into Equation (4.9) and enforcing the BC of Equation (4.8), we get

$$\boldsymbol{E}_t^i(\boldsymbol{r}) + \sum_{m=1}^{M} I_m \boldsymbol{E}_t^{B_m}(\boldsymbol{r}) = 0; \quad \boldsymbol{E}^{B_m}(\boldsymbol{r}) = \int_{S'} \boldsymbol{B}_m(\boldsymbol{r}') \cdot \overline{\boldsymbol{G}}(\boldsymbol{r}, \boldsymbol{r}')\mathrm{d}s'. \tag{4.10}$$

Next, similar to the discussion on the variational method briefly covered before in Section 2.5, a weighted average of the boundary condition needs to be constructed. To this end, a set of N weighting (aka testing) functions $\boldsymbol{W}_n(\boldsymbol{r}_s)$ is introduced, and according to Galerkin's weighted residual method, is set equal to the basis functions, i.e. $\boldsymbol{W}_n(\boldsymbol{r}_s) = \boldsymbol{B}_n(\boldsymbol{r}_s)$. Multiplying both sides of Equation (4.10) by N weighting functions leads to a set of N linear equations to determine the M unknown expansion coefficients I_ms. Since a unique solution for all I_ms is desirable, one needs to set $N = M$ to obtain the following typical formula

$$\sum_{m=1}^{M} I_m Z_{mn} = V_n, \quad \text{for} \quad n = 1,\ 2, \cdots,\ N \tag{4.11}$$

with

$$Z_{mn} = \langle \boldsymbol{E}^{B_m}, \boldsymbol{W}_n \rangle = \int_S \boldsymbol{E}^{B_m}(\boldsymbol{r}_s) \cdot \boldsymbol{W}_n(\boldsymbol{r}_s) \mathrm{d}s, \tag{4.12a}$$

$$V_n = -\langle \boldsymbol{E}^i, \boldsymbol{W}_n \rangle = -\int_S \boldsymbol{E}^i(\boldsymbol{r}_s) \cdot \boldsymbol{W}_n(\boldsymbol{r}_s) \mathrm{d}s. \tag{4.12b}$$

In this case, Z_{mn} is known as the reaction integral with the symmetric product operation defined as $\langle \boldsymbol{a}, \boldsymbol{b} \rangle = \int \boldsymbol{a} \cdot \boldsymbol{b} \mathrm{d}s$.

Method of moments gives acceptable and accurate results for most cases, and for this reason, it is often used as a 'benchmark' for other approximate numerical methods. However, whenever $\boldsymbol{B}_m(\boldsymbol{r}')$ and $\boldsymbol{W}_n(\boldsymbol{r}_s)$ overlap in Z_{mm} calculation (i.e. in self-impedance calculation for each basis function $\boldsymbol{B}_m$), a problem known as source point singularities may arise because Green's function becomes singular when the field point $\boldsymbol{r}_s$ and the source point $\boldsymbol{r}'$ coincide. Moreover, getting uniform convergence in MoM solutions, when M increases, may sometimes face difficulty due to some numerical instability such as the presence of structural resonances which then give rise to spurious or even erroneous results at specific frequencies.

The problem of hyper-singularity, which occurs in self-impedance calculation of the EFIE-based MoM formulation discussed above, can be alleviated by using the mixed potential integral equation (MPIE) approach [211], where the electric field at the surface boundary is represented by both vector and scalar potentials. This way, the resulting integrals of the MPIE self-impedances contain singularities of order one, which is easier to handle. Crucial to the formulation is the utilization of a special set of sub-domain basis functions which yield a current representation free of line or point charges at the sub-domain boundaries. In other words, MPIE decomposition necessitates that the vector basis/weight function be 'div-conforming', meaning that its divergence tends to zero at the line-boundary of each sub-domain. The most used div-conforming basis functions in the MoM context are the so-called Rao-Wilton-Glisson (RWG) basis functions [212], which are defined on pairs (doublets) of adjacent triangular patches and thanks to their triangular shape are conformal to any kind of curved surfaces.

4.2 DDM & Generalized Admittance Approach

Following a similar procedure in the original study of Harrington [207], a general formulation for a two-region aperture is considered in this section. The formulation begins by expressing the problem as an operator equation involving an unknown equivalent magnetic current. Applying the method of moments then converts this operator form into a corresponding matrix system. In this framework, interaction between regions occurs solely through the aperture, whose behavior is characterized by region-specific admittance matrices. The general problem of aperture coupling between two regions, labeled a and b, is represented in Figure 4.3(a). In region b, there are impressed sources $\boldsymbol{J}^i$, $\boldsymbol{M}^i$, and region a is assumed source-free. Region b is shown to be bounded by an electric conductor, while region a is assumed to be open to infinity.

Domain decomposition method (DDM) utilizes the equivalence principle in order to split the problem into two equivalent parts as shown in Figure 4.3(b). In region b, the field is produced by the sources $\boldsymbol{J}^i$, $\boldsymbol{M}^i$, plus the equivalent magnetic current $\boldsymbol{M} = \boldsymbol{n} \times \boldsymbol{E}$ over the aperture region, with the aperture covered by an electric conductor. The field, in region a, is produced by the equivalent magnetic current $-\boldsymbol{M}$ over the aperture region, while the aperture is covered by an electric conductor. This way, the continuity of the tangential component of the electric field across the aperture is guaranteed by the fact that the equivalent current in region a is the negative of that in region b. The remaining boundary condition to be applied is to ensure that the tangential component of the magnetic field remains continuous across the aperture. In mathematical terms, the tangential component of magnetic fields in region a ($\boldsymbol{H}_t^a$) and region b ($\boldsymbol{H}_t^b$) must be set equal to one another, where $\boldsymbol{H}_t^b = \boldsymbol{H}_t^i + \boldsymbol{H}_t^b(\boldsymbol{M})$ is due to the presence of the impressed sources and the equivalent source in region b whereas the only source in region a is $-\boldsymbol{M}$ producing $\boldsymbol{H}_t^a = \boldsymbol{H}_t^a(-\boldsymbol{M})$, which can also be written as $\boldsymbol{H}_t^a = -\boldsymbol{H}_t^a(\boldsymbol{M})$ due to linearity of the $\boldsymbol{H}_t^a$ operator. Enforcing continuity of magnetic fields across the aperture therefore results in

$$-\boldsymbol{H}_t^a(\boldsymbol{M}) - \boldsymbol{H}_t^b(\boldsymbol{M}) = \boldsymbol{H}_t^i \tag{4.13}$$

which is the basic operator equation for determining the equivalent magnetic current $\boldsymbol{M}$.

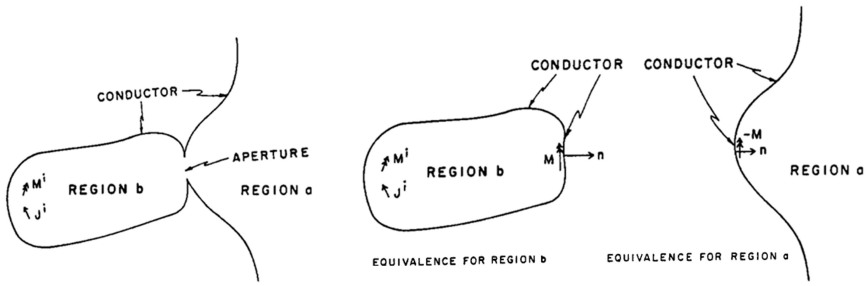

(a) (b)

Figure 4.3: The general problem of two regions coupled through an aperture. (a) The original problem and (b) its equivalent problems resulting from the application of DDM, thus dividing the original problem into two. (Figures are taken and reprinted from [207])

The exact solution to Equation (4.13) can be obtained only for a handful of canonical problems. However, to extend the applicability of the DDM approach to any given problem, a numerical technique such as MoM can be employed to obtain an approximate solution as follows. Through expanding $\boldsymbol{M}$ in terms of a set of basis functions $\{\boldsymbol{m}_n\}_{n=1}^{N}$, i.e. $\boldsymbol{M} = \sum_{n=1}^{N} V_n \boldsymbol{m}_n$, where the coefficients V_n are to be determined, and using the linearity of the $\boldsymbol{H}_t$ operators, one can rewrite Equation (4.13) as

$$-\sum_{n=1}^{N} V_n \boldsymbol{H}_t^a(\boldsymbol{m}_n) - \sum_{n=1}^{N} V_n \boldsymbol{H}_t^b(\boldsymbol{m}_n) = \boldsymbol{H}_t^i. \tag{4.14}$$

Next, using the same set of basis function as the testing function (Galerkin balancing method) $\{\boldsymbol{W}_m = \boldsymbol{m}_m\}_{m=1}^{N}$ and taking the symmetric product of Equation (4.14) with each testing function $\boldsymbol{m}_m$, we obtain

$$-\sum_{n=1}^{N} V_n \langle \boldsymbol{m}_m \, , \boldsymbol{H}_t^a(\boldsymbol{m}_n)\rangle - \sum_{n=1}^{N} V_n \langle \boldsymbol{m}_m \, , \boldsymbol{H}_t^b(\boldsymbol{m}_n)\rangle = \langle \boldsymbol{m}_m \, , \boldsymbol{H}_t^i\rangle, \quad \text{for } m = 1, \cdots, N. \tag{4.15}$$

As can be seen, this method leads to a set of N linear equations whose solution determines the coefficients $\mathbf{V} = [V_1,\ V_2,\ \cdots,\ V_N]^T$ and consequently

$\boldsymbol{M}$ in the end. Once $\boldsymbol{M}$ is known, the fields and field-related parameters of the original problem can be computed by standard methods. Moreover, by defining

$$\langle -\boldsymbol{m}_m, \boldsymbol{H}_t^a(\boldsymbol{m}_n)\rangle = Y_{mn}^a, \quad \text{and} \quad \langle -\boldsymbol{m}_m, \boldsymbol{H}_t^b(\boldsymbol{m}_n)\rangle = Y_{mn}^b \tag{4.16}$$

as aperture admittances for regions a and b, and $\langle \boldsymbol{m}_m, \boldsymbol{H}_t^i\rangle = I_m^i$ for the excitation term, we can rewrite Equation (4.15) as

$$\sum_{n=1}^{N} V_n Y_{mn}^a \; + \; \sum_{n=1}^{N} V_n Y_{mn}^b \; = \; I_m^i, \quad \text{for} \quad m = 1, \cdots, N \tag{4.17}$$

or in the compact matrix notation form of

$$\left[\mathbf{Y}^a + \mathbf{Y}^b\right] \mathbf{V} = \mathbf{I}^i \tag{4.18}$$

where $\mathbf{I}^i = \left[I_1^i,\ I_2^i,\ \cdots,\ I_N^i\right]^T$. Note that the minus signs are introduced in the abovementioned definition of admittances to make sure that the real parts of admittances are positive when $\boldsymbol{W}_n = \boldsymbol{m}_n$. As shown, the aperture coupling is ultimately expressible as the sum of the two independent aperture admittance matrices, with source terms related to the incident magnetic field. Equation (4.18) can be interpreted in the framework of a generalized network as two networks $\mathbf{Y}^a$ and $\mathbf{Y}^b$ in parallel with $\mathbf{I}^i$, whose resultant solution is equivalent to an N-term variational solution to Equation (4.13).

Multi-Scale EM Surface Analyzer

This section first revamps the original two-region DDM formulation of Harrington discussed previously and revisited here in sub-figure 4.4(a). It then proceeds to expand the concept to a K-aperture problem of an open-cavity-based RIS panel, and finally, the section concludes by introducing a novel hybrid DDM (H-DDM) framework illustrated in sub-figure 4.4(b), complete treatment of which can be found in *Paper E*.

Unlike Harrington's original MFIE formulation [207], [213] which is based on PEC equivalence and hence deals only with the surface magnetic current $\boldsymbol{M}_s$, free-space equivalence, aka Love's theorem, of Section 4.1 is employed here which leads to dealing with both MFIE and EFIE equations associated with magnetic as well as electric surface current densities $\boldsymbol{M}_s$ and $\boldsymbol{J}_s^a,\ \boldsymbol{J}_s^b$,

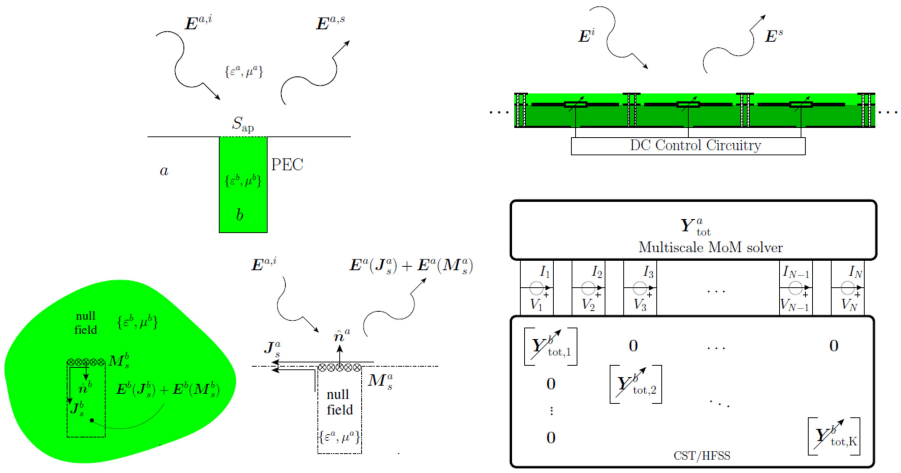

Figure 4.4: The basic idea behind H-DDM (a) at the UC level for a 2-region problem and (b) at the RIS panel level with K tunable apertures.

as shown in Figure 4.4(a). Note that the normal unit vectors to the aperture surface S_{ap} for two equivalent internal (labeled as b) and external (labeled as a) regions are set to point in opposite directions in the figure. In other words, $\hat{\boldsymbol{n}}^a = -\hat{\boldsymbol{n}}^b$ and since the tangential electric field component across the surface should remain continuous, i.e. $\boldsymbol{E}_t^a = \boldsymbol{E}_t^b$ where $\boldsymbol{E}_t^a = \hat{\boldsymbol{n}}^a \times \boldsymbol{M}_s^a$ and $\boldsymbol{E}_t^b = \hat{\boldsymbol{n}}^b \times \boldsymbol{M}_s^b$, then one can conclude that $\hat{\boldsymbol{n}}^a \times \boldsymbol{M}_s^a = -\hat{\boldsymbol{n}}^a \times \boldsymbol{M}_s^b$ which results in the single magnetic current $\boldsymbol{M}_s^a = -\boldsymbol{M}_s^b = \boldsymbol{M}_s$. The interior electric surface current $\boldsymbol{J}_s^b$ is, however, different from the exterior electric surface current $\boldsymbol{J}_s^a$ as emphasized in the figure.

The MFIE formulation, whose complete treatment can be found in [195], begins by enforcing continuity of tangential magnetic fields across the aperture as $\boldsymbol{H}_t^a = \boldsymbol{H}_t^b$ in which $\boldsymbol{H}^a$ has three contributors of firstly the form of impressed impinging wave from region a denoted as $\boldsymbol{H}^{a,i}$, secondly the form of magnetic field radiated by magnetic surface current $\boldsymbol{M}_s$ denoted as $\boldsymbol{H}^a(\boldsymbol{M}_s)$, and thirdly the form of magnetic field radiated by electric surface current in region a denoted as $\boldsymbol{H}^a(\boldsymbol{J}_s^a)$. Note that $\boldsymbol{H}^b$ can be interpreted and constructed in a similar fashion just by replacing superscript a with b and

that the compact operator formulas for them are those provided in Section 4.1 through Equations (4.3) and (4.4). Therefore, we have

$$\begin{aligned}\left[\boldsymbol{H}^{a,i}+\boldsymbol{H}^{a}(\boldsymbol{M}_s)+\boldsymbol{H}^{a}(\boldsymbol{J}_s^a)\right]_{\tan}&=\left[\boldsymbol{H}^{b,i}+\boldsymbol{H}^{b}(-\boldsymbol{M}_s)+\boldsymbol{H}^{b}(\boldsymbol{J}_s^b)\right]_{\tan},\\ \left[\boldsymbol{H}^{a}(\boldsymbol{M}_s)+\boldsymbol{H}^{b}(\boldsymbol{M}_s)\right]_{\tan}+\left[\boldsymbol{H}^{a}(\boldsymbol{J}_s^a)-\boldsymbol{H}^{b}(\boldsymbol{J}_s^b)\right]_{\tan}&=\left[\boldsymbol{H}^{b,i}-\boldsymbol{H}^{a,i}\right]_{\tan}\end{aligned} \tag{4.19}$$

which is the exact MFIE equation at the aperture and can be cast into the framework of MoM and Galerkin weighted residual approach by expanding the surface currents in terms of RWG basis functions $\{\boldsymbol{m}_n,\ \boldsymbol{i}_n^a,\ \boldsymbol{i}_n^b\}$ as follows

$$\boldsymbol{M}_s(\boldsymbol{r})=\sum_{n=1}^{N_e}V_n\boldsymbol{m}_n(\boldsymbol{r}),\qquad \text{for}\quad \boldsymbol{r}\in S_{\text{ap}} \tag{4.20}$$

$$\boldsymbol{J}_s^a(\boldsymbol{r})=\sum_{n=1}^{N_e^a}I_n^a\boldsymbol{i}_n^a(\boldsymbol{r}),\quad \boldsymbol{J}_s^b(\boldsymbol{r})=\sum_{n=1}^{N_e^b}I_n^b\boldsymbol{i}_n^b(\boldsymbol{r}) \tag{4.21}$$

where N_e is the number of expanding sub-domain basis functions for $\boldsymbol{M}_s$ and $\mathbf{V}=[V_1,V_2,\cdots,V_{N_e}]^T$ is the vector of unknown coefficients to be determined as the ultimate goal of solving the DDM equations while $\mathbf{I}^a=[I_1^a,I_2^a,\cdots,I_{N_e^a}^a]^T$ and $\mathbf{I}^b=[I_1^b,I_2^b,\cdots,I_{N_e^b}^b]^T$ are dependent variables (as will become more evident further below) and can be conveniently found once $\mathbf{V}$ is solved for. Testing Equation (4.19) by the basis functions $\{-\boldsymbol{m}_m\}$ and using the symmetric product of reaction integrals leads to the following formulation:

$$\begin{aligned}&\langle-\boldsymbol{m}_m,\boldsymbol{H}_t^a(\boldsymbol{M}_s)+\boldsymbol{H}_t^b(\boldsymbol{M}_s)\rangle+\langle-\boldsymbol{m}_m,\boldsymbol{H}_t^a(\boldsymbol{J}_s^a)-\boldsymbol{H}_t^b(\boldsymbol{J}_s^b)\rangle\ =\\ &\qquad\langle-\boldsymbol{m}_m,\boldsymbol{H}_t^{b,i}\rangle-\langle-\boldsymbol{m}_m,\boldsymbol{H}_t^{a,i}\rangle,\qquad m=1,2,\cdots,N_e\end{aligned} \tag{4.22}$$

Using linearity of the operators and the definition of aperture admittances (according to Equation (4.16)), we obtain

$$\sum_{n=1}^{N_e}\left[Y_{mn}^a+Y_{mn}^b\right]V_n+\sum_{n=1}^{N_e^b}C_{mn}^bI_n^b-\sum_{n=1}^{N_e^a}C_{mn}^aI_n^a=I_m^{a,i}-I_m^{b,i},\ m=1,2,\cdots,N_e \tag{4.23}$$

where

$$\begin{aligned} C_{mn}^{a,b} &= \langle \boldsymbol{m}_m, \boldsymbol{H}_t^{a,b}(\boldsymbol{i}_n^{a,b}) \rangle \\ I_m^{a,i} = \langle \boldsymbol{m}_m, \boldsymbol{H}_t^{a,i} \rangle, &\qquad I_m^{b,i} = \langle \boldsymbol{m}_m, \boldsymbol{H}_t^{b,i} \rangle. \end{aligned} \tag{4.24}$$

This N_e set of linear equations can be conveniently represented in the compact form of vector-matrix multiplication by rewriting Equation (4.23) as

$$\left[\mathbf{Y}^a + \mathbf{Y}^b\right] \mathbf{V} + \mathbf{C}^b \mathbf{I}^b - \mathbf{C}^a \mathbf{I}^a = \mathbf{I}^{a,i} - \mathbf{I}^{b,i}. \tag{4.25}$$

As stated before, the ultimate goal is to find $\boldsymbol{M}_s$ of which $\mathbf{V}$ is an N_e-term variational approximate solution. In fact, $\mathbf{I}^a$ and $\mathbf{I}^b$ are intermediate, dependent variables and can therefore be found in terms of $\mathbf{V}$ by enforcing the second set of boundary conditions, i.e. ensuring electric field continuity as follows:

$$\boldsymbol{E}_t^a = \hat{\boldsymbol{n}}^a \times \boldsymbol{M}_s = -\hat{\boldsymbol{n}}^b \times \boldsymbol{M}_s = \boldsymbol{E}_t^b \tag{4.26}$$

which results in the two following EFIE equations

$$\left[\boldsymbol{E}^{a,i} + \boldsymbol{E}^a(\boldsymbol{M}_s) + \boldsymbol{E}^a(\boldsymbol{J}_s^a)\right]_{\tan} = \hat{\boldsymbol{n}}^a \times \boldsymbol{M}_s, \tag{4.27}$$

$$\left[\boldsymbol{E}^{b,i} - \boldsymbol{E}^b(\boldsymbol{M}_s) + \boldsymbol{E}^b(\boldsymbol{J}_s^b)\right]_{\tan} = -\hat{\boldsymbol{n}}^b \times \boldsymbol{M}_s. \tag{4.28}$$

Following a similar Galerkin procedure by testing with $\{\boldsymbol{i}_m^{a,b}\}$ and expansions to basis functions as before, the discretized version of the EFIEs read:

$$\sum_{n=1}^{N_e^a} Z_{mn}^a I_n^a = \sum_{n=1}^{N_e} D_{mn}^a V_n + V_m^{a,i}, \quad \text{for} \quad m = 1, 2, \cdots, N_e^a \tag{4.29}$$

$$\sum_{n=1}^{N_e^b} Z_{mn}^b I_n^b = -\sum_{n=1}^{N_e} D_{mn}^b V_n + V_m^{b,i}, \quad \text{for} \quad m = 1, 2, \cdots, N_e^b \tag{4.30}$$

where

$$Z_{mn}^{a,b} = -\langle \boldsymbol{i}_m^{a,b}, \boldsymbol{E}_t^{a,b}(\boldsymbol{i}_n^{a,b}) \rangle, \quad D_{mn}^{a,b} = \langle \boldsymbol{i}_m^{a,b}, \boldsymbol{E}_t^{a,b}(\boldsymbol{m}_n) - \hat{\boldsymbol{n}}^{a,b} \times \boldsymbol{m}_n \rangle \tag{4.31}$$

$$V_m^{a,i} = \langle \boldsymbol{i}_m^a, \boldsymbol{E}_t^{a,i} \rangle, \quad V_m^{b,i} = \langle \boldsymbol{i}_m^b, \boldsymbol{E}_t^{b,i} \rangle \tag{4.32}$$

or simply

$$\mathbf{Z}^a\mathbf{I}^a = \mathbf{D}^a\mathbf{V} + \mathbf{V}^{a,i} \tag{4.33}$$

$$\mathbf{Z}^b\mathbf{I}^b = -\mathbf{D}^b\mathbf{V} + \mathbf{V}^{b,i}. \tag{4.34}$$

By rearranging the above equations, the intermediate variables can now be expressed in terms of $\mathbf{V}$:

$$\mathbf{I}^a = (\mathbf{Z}^a)^{-1}\left(\mathbf{V}^{a,i} + \mathbf{D}^a\mathbf{V}\right), \qquad \mathbf{I}^b = \left(\mathbf{Z}^b\right)^{-1}\left(\mathbf{V}^{b,i} - \mathbf{D}^b\mathbf{V}\right) \tag{4.35}$$

and finally, the substitution of $\mathbf{I}^a$ and $\mathbf{I}^b$ back into Equation (4.25) leads to the final generalized admittance formula as follows:

$$\left[\mathbf{Y}^a_{\text{tot}} + \mathbf{Y}^b_{\text{tot}}\right]\mathbf{V} = \mathbf{I}, \tag{4.36}$$

where

$$\mathbf{Y}^a_{\text{tot}} = \mathbf{Y}^a - \mathbf{C}^a(\mathbf{Z}^a)^{-1}\mathbf{D}^a \tag{4.37a}$$

$$\mathbf{Y}^b_{\text{tot}} = \mathbf{Y}^b - \mathbf{C}^b(\mathbf{Z}^b)^{-1}\mathbf{D}^b \tag{4.37b}$$

$$\mathbf{I} = \left[\mathbf{I}^{a,i} + \mathbf{C}^a(\mathbf{Z}^a)^{-1}\mathbf{V}^{a,i}\right] - \left[\mathbf{I}^{b,i} + \mathbf{C}^b(\mathbf{Z}^b)^{-1}\mathbf{V}^{b,i}\right]. \tag{4.37c}$$

Once $\mathbf{V}$ is known from solving Equation (4.36), one can find the magnetic surface current distribution through RWG basis function expansion of Equation (4.20) as well as the electric surface current distributions using Equation (4.35) in conjunction with Equation (4.21). Having $\boldsymbol{M}_s$ and $\boldsymbol{J}^a_s$ at hand, the scattered field from the panel in region a can then be easily calculated as $\boldsymbol{E}^a(\boldsymbol{M}_s) + \boldsymbol{E}^a(\boldsymbol{J}^a_s)$ using the operator relations in Equations (4.3) and (4.4).

Armed with the developed methodology above, the extension of the two-region method of Figure 4.4(a) to a K-aperture panel is straightforward at this point, as illustrated in Figure 4.4(b). This is accomplished by stacking internal admittances per aperture into a block-diagonal matrix for the interior regions because the cells are isolated at the substrate level due to the presence of metallic walls. In contrast, the external $\mathbf{Y}^a_{\text{tot}}$ is a fully populated matrix accounting for all over-the-air mutual couplings occurring among the cells. This way, DDM allows for hybridization of different techniques by separating the highly sensitive internal regions, which are usually in need of

high-density meshes to resolve and capture their resonance nature, from the external free-space propagation medium that can be efficiently handled by a fast computational technique with much lower mesh densities. For instance, FEM-BEM-DDM was recently proposed in the literature [214] for analyzing static ('frozen') metasurfaces, where the finite element method (FEM) was hired to resolve the internal regions while the external region was handled by the fast asymptotic boundary element method (BEM).

Along this line, *Paper E* proposes a hybrid DDM (H-DDM) technique to handle all sorts of open-cavity-based beamforming panels, including reconfigurable ones with sophisticated interior structures and/or lumped components. To this end and to be able to handle reconfigurability of the dynamic panels – a feature typically attributed to the presence of such lumped circuit elements as Varactor or PIN diodes – H-DDM interfaces CST with an in-house developed MoM-based platform named multi-scale EM surface analyzer (MESA). For the internal domains, plane wave (PW) characterization using CST is adopted and that is the reason why two different index numbers, i.e. K and N, are shown in the schematic circuit representation of Figure 4.4(b) to convey the message that depending on the operating frequency and the structural features of the unit cells, we might need several modes, say N_c, per each aperture to fully characterize the internal field distribution on S_{ap} through a multi-PW characterization scheme. Therefore, N in general is bigger than K, having the relation $N = K \times N_c$ provided a uniform N_c-PW characterization is employed for all the aperture types.

However, only single-PW characterizations are performed in *Paper E* by setting N equal to K, which leaves the multi-PW characterization scheme and its associated SVD post-processing as a future study. For this purpose, a relatively simple UC structure, called Pin-Waveguide (PinWG), was designed for the center frequency of 0.85 GHz that could be fully characterized by only one normally incident PW in CST. Interested readers can find the design details in *Paper E* which are not repeated here for the sake of brevity. Once the PW characterization is complete and the aperture field distributions are exported from CST, the calculation of $\mathbf{Y}^b$ per aperture type can be numerically performed as outlined in the next section. The following numerical step, in fact, is to replace all analytical calculations for the internal regions, as stated, e.g., in Equation (4.37b) above.

Numerical Calculation of Y^b in H-DDM

As explained above, field quantities of the internal cavity regions are extracted from CST simulations in the proposed H-DDM framework. This section explains how by having aperture field distributions $\boldsymbol{E}$ and $\boldsymbol{H}$ at hand, one can numerically calculate the aperture input admittance of the internal open cavity structure as follows:

$$Y^b = \frac{I}{V} = \frac{2P^*}{|V|^2} = \frac{1}{|V|^2}\int_S [\boldsymbol{E}^* \times \boldsymbol{H}] \cdot \hat{\boldsymbol{n}}\, \mathrm{d}s. \tag{4.38}$$

Using vector identities, one can rewrite $\hat{\boldsymbol{n}} \cdot (\boldsymbol{E}^* \times \boldsymbol{H}) = \boldsymbol{H} \cdot (\hat{\boldsymbol{n}} \times \boldsymbol{E}^*) = -\boldsymbol{E}^* \cdot (\hat{\boldsymbol{n}} \times \boldsymbol{H})$, simplify the last equivalent term by means of BCs at the aperture's surface, i.e. $\hat{\boldsymbol{n}} \times \boldsymbol{H} = \boldsymbol{J}_s,\ \boldsymbol{E} \times \hat{\boldsymbol{n}} = \boldsymbol{M}_s$, and substitute $-\boldsymbol{E}^* \cdot \boldsymbol{J}_s$ back into the equation as follows

$$Y^b = -\frac{1}{|V|^2}\int_S \boldsymbol{E}^* \cdot \boldsymbol{J}_s\, \mathrm{d}s = -\frac{1}{|V|^2}\int_S \boldsymbol{J}_s \cdot [\hat{\boldsymbol{n}} \times \boldsymbol{M}_s^*]\, \mathrm{d}s. \tag{4.39}$$

Finally, expanding the surface currents in terms of N RWG basis functions $\{\boldsymbol{i}_n,\ \boldsymbol{m}_n\}_{n=1}^N$ as $\boldsymbol{J}_s(\boldsymbol{r}) = \sum_{n=1}^N I_n \boldsymbol{i}_n(\boldsymbol{r})$ and $\boldsymbol{M}_s(\boldsymbol{r}) = \sum_{n=1}^N V_n \boldsymbol{m}_n(\boldsymbol{r})$ and applying Galerkin's testing procedure using the symmetric product, we obtain

$$Y^b = -\frac{1}{|V|^2}\int_S \sum_{m=1}^N I_m \boldsymbol{i}_m \cdot \left[\hat{\boldsymbol{n}} \times \sum_{n=1}^N V_n^* \boldsymbol{m}_n\right] \mathrm{d}s \tag{4.40}$$

which can also be written in the compact vector-matrix multiplication form $Y = -\frac{1}{|V|^2}\mathbf{I}^T\mathbf{G}\mathbf{V}^*$ with $\mathbf{G}$ as an $N \times N$ Gram matrix with elements $G_{mn} = \langle \boldsymbol{i}_m,\ \hat{\boldsymbol{n}} \times \boldsymbol{m}_n \rangle = \int_s (\boldsymbol{i}_m \cdot \hat{\boldsymbol{n}} \times \boldsymbol{m}_n)\, \mathrm{d}s$.

4.3 Mutual Coupling & Subarray Analysis

As discussed earlier, quasi-periodic effects in Reflectarrays and RISs are in general non-negligible and have thus spurred a lot of interest in the research community to investigate and even possibly quantify them. For instance, 'beyond-diagonal RIS' is a term coined in the wireless communication society [215], [216] to refer to a new wave of RIS design methodology which is mutual coupling (MC) aware. When it comes to practical implementations,

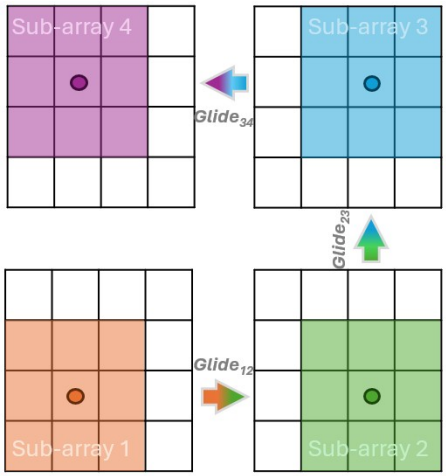

Figure 4.5: Subarray analysis of a 4×4 panel and the idea behind its Convolutional gliding window which is set to 3×3 in this example to capture the mutual coupling effects of only the immediate surrounding neighbors.

non-coherent mutual couplings stemming from these quasi-periodic effects typically manifest themselves in the form of deviations in the measured scattering patterns of the beamformed panels from their predicted and/or desired beamforming goals and objectives. Among a host of different techniques proposed in the literature to investigate the undesirable impact of MCs, sub-array analysis [163], [217] stands out.

Along this line, *Paper E* recasts the formulation of H-DDM into the isolated element-in-array-pattern (EIAP) framework by diagonalizing $\mathbf{Y}^{a}_{\text{tot}}$ matrix in Figure 4.4(b) to analyze the severity of MC effects. Therefore, 1-element sub-array analysis was adopted to show over-the-air mutual coupling impacts in RIS pattern predictions as exemplified through two linear beamforming panels in the next section. Although not investigated in *Paper E* for very huge beamforming panels, other sub-array schemes such as convolutional gliding windows of different sizes, as shown in Figure 4.5 for a 3×3 case, can be envisaged in future studies to strike a balance between accuracy and run-time in an optimized version of H-DDM equipped with translational symmetry and matrix compression.

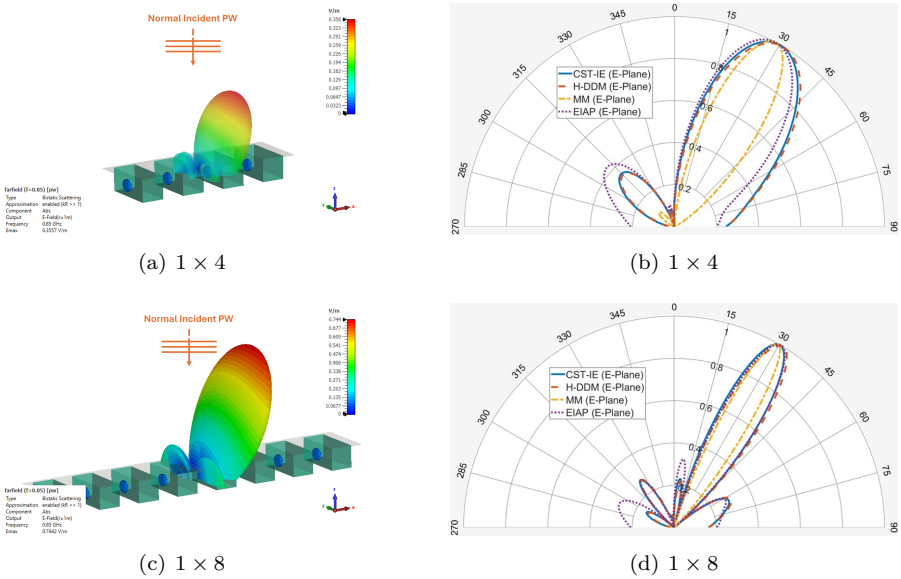

(a) 1×4 (b) 1×4

(c) 1×8 (d) 1×8

Figure 4.6: PinWG 1D array examples of 1×4 and 1×8 synthesized to reflect a normally incident plane wave into $+30°$ in the E-plane.

4.4 PinWG: A Representative Example

As a simple example, this short section provides two linear beamforming panels (1×4 and 1×8) to show the performance of the proposed H-DDM and compare its FF scattering pattern result against FW CST and Macromodeling predictions. Over-the-air MC impact on pattern deviation is also considered in the EIAP framework and the results are reported in Figure 4.6. The Varactors in the panels are set to reflect a normally incident PW towards $+30°$ elevational angle in the X-Z plane. As can be seen from the plots, the H-DDM results show the closest agreement to the IE solver of CST, which is served here as a 'ground truth' prediction of the panels' behavior in the absence of real measurements. All four techniques are successful in predicting the main beam direction although their accuracy in sidelobe predictions varies considerably as evident from the 2D cuts. Further results, discussion, and error quantization for bigger 2D array examples can be found in *Paper E*.

CHAPTER 5

Summary of included papers

This chapter provides a summary of the included papers.

5.1 Paper A

Morteza Ghaderi Aram, Hadi Aliakbarian, Hana Dobšíček Trefná
An Ultra-Wideband Compact Design for Hyperthermia: Open Ridged-Waveguide Antenna
Published in IET Microwaves, Antennas & Propagation,
vol. 16, no. 2, pp. 137–152, Feb. 2022.
 DOI: 10.1049/mia2.12226.

The focus of *Paper A* is to design an element of a phased array applicator, i.e. the antenna. Antennas are the building block of applicators whose design and fabrication require special attention to assure an efficient energy transfer. They are loaded with a patient body located not well into their far-field, and for an efficient transition of waves, they demand a matching medium, known as waterbolus. Important features of a good antenna design for hyperthermic applications are to have a wide frequency band of operation, to be compact

and robust to environmental noise, to have a sufficient penetration depth, and to leave a small EMI footprint. To introduce a new and efficient antenna element, *Paper A* proposes a customized antenna design from the double-ridged horn (DRH) family and names it open ridged-waveguide (ORWG). The design procedure starts with a scaled version of a well-established DRH design which is further tailored and optimized to suit the HT applications. The optimized design is fabricated and its performance is assessed both numerically and experimentally according to the HT quality assurance guidelines. The proposed antenna satisfies all the requirements of the HT guidelines for both superficial and deep hyperthermia. Moreover, the reported results make the design stand out from the previously proposed models in the field by showing that (a) the new antenna model has a wide operational bandwidth, with a fractional bandwidth more than 75% from 400 MHz to 800 MHz (b) the antenna needs no balun or RF matching network, hence avoiding the stray losses associated with balun (c) ORWG is an efficient radiator to deposit energy deeply enough into the body.

M.G.A. contributed to the conceptual development of the study, participated in designing the methodology, carried out the formal analysis, performed the measurements, curated the data, and prepared the visualizations. H.A. was involved in the conceptualization and methodological design, fabricated the prototypes, assisted with data curation, and provided supervisory guidance throughout the project. H.D.T. contributed to the methodological framework, took part in the measurement activities, and secured the funding that supported this work. All authors collaborated in writing and refining the manuscript.

5.2 Paper B

Morteza Ghaderi Aram, Hadi Aliakbarian, Hana Dobšíček Trefná
A Phased Array Applicator based on Open Ridged-Waveguide Antenna for Microwave Hyperthermia
Published in Microwave and Optical Technology Letters,
vol. 63, no. 12, pp. 3086-3091, Sep. 2021.
 DOI: 10.1002/mop.33039.

Paper B is a short communication to demonstrate the feasibility of focusing energy into deep-seated tumors via an elliptical phased array applicator

consisting of 16 ORWG antennas. The focus of *Paper B* is not on the antenna itself but rather on the antenna's function as an element within the phased array applicator, mutual coupling of the adjacent elements, and beamforming for an efficient power deposition. A hybrid, in-house beamforming method based on time reversal (TR) and particle swarm optimization (PSO) to avoid getting trapped in local minima and to have a faster convergence is also introduced. The power deposition capability of the proposed applicator was investigated on a realistic H&N patient model with a relatively large tumor in his tongue. After exporting the power loss densities (PLD) of all 16 antennas simulated in CST, we performed the hybrid TR-PSO beamforming method in MATLAB for the treatment planning of the patient model. Thermal simulation of the scenario was subsequently performed by FEniCS, an open-source FEM-based computational platform. The effectiveness of the proposed applicator, the beamforming method, and the ensuing thermal analysis was quantitatively assessed by the calculation of SAR-based and temperature-based quality metrics such as target coverage 25% ($TC_{25\%}$), T_{90}, T_{50}, and T_{10}. Overall, satisfactory results of this short letter motivate fabrication of the proposed applicator for future studies and eventually for clinical trials.

M.G.A. contributed to the conceptual development of the study, designed the methodology, implemented the software, performed the formal analysis, carried out the measurements, curated the data, and prepared the visualizations. H.A. participated in shaping the methodology, handled the fabrication of the prototypes, and provided supervisory guidance. H.D.T. contributed to the conceptualization of the work, assisted with the measurements, supervised the research activities, and secured the funding that supported the study. All authors were involved in writing and refining the manuscript.

5.3 Paper C

Morteza Ghaderi Aram, Özlem Tuğfe Demir, Tommy Svensson, Emil Björnson
Holographic MIMO and Near-Field-Compliant Channel Modeling
A Book Chapter in *Intelligent Metasurfaces for 6G and Beyond Using Electromagnetic, Signal, and Information Theory*,
Wiley, in press

Book Chapter C surveys holographic MIMO (H-MIMO) from electromagnetic and communications perspectives, establishing a unified theoretical and practical foundation for near-field-compliant channel modeling. It reviews the plane-wave expansion method (PWEM) and spatio-temporal Fourier techniques, develops Floquet/Bloch harmonic expansions for periodic metasurfaces, and connects these EM tools to holographic design procedures that translate desired far-field beams into surface phase/current prescriptions. The chapter contrasts H-MIMO with reconfigurable intelligent surfaces (RIS), emphasizing denser sub-wavelength element spacing, stronger mutual coupling, enlarged virtual apertures, and the resulting need to model radiative near-field propagation. Practical feeding strategies (spatial illumination vs integrated surface-wave launchers), fabrication and reconfigurability mechanisms for metasurfaces, and implications for channel estimation are discussed. Overall, the chapter establishes a framework within the Electromagnetic Signal and Information Theory (ESIT) initiative to fuse electromagnetics (PWEM, Floquet theory, Helmholtz/Maxwell formulations) with communication-oriented channel modeling and estimation, highlighting both the promise of H-MIMO for energy-efficient spatial processing in 6G and the open challenges (mutual coupling, CSI acquisition, and fundamental limits) that remain to be addressed.

M.G.A. conducted the survey on EM background and Holography, used a commercial software package for beamforming examples, and prepared the visualizations of the EM section. Ö.T.D. and E.B. summarized their recent research activities on near-field-compliant channel modeling and estimation. T.S. contributed to the conceptualization of the work and secured the funding that supported the EM part of the study. M.G.A., Ö.T.D., and E.B. were involved in writing and refining the manuscript.

5.4 Paper D

Morteza Ghaderi Aram, Fitim Maxharraj, Rob Maaskant, Tommy Svensson

On RIS Macromodeling of a Large Holographic-Inspired Beamforming Panel

Proceeding of the 20th European Conference on Antennas and Propagation (EuCAP), 2026,

Paper D investigates the Macromodeling (MM) technique for large holographically designed beamforming panels and evaluates its fidelity and runtime trade-offs versus full-wave (FW) simulations. An angle-insensitive unit cell (UC) is taken from the literature and slightly modified to serve as the building block of a 10×14 panel. MM treats each UC under local periodicity as a two-port network (with the S/Z-matrix extracted from one FW UC run). Having the per-cell reflection coefficients calculated in the framework of microwave network analysis, the panel's far-field scattering pattern can then be predicted via the calculation of the array factor and utilization of the pattern multiplication rule. Comparisons at $f_c = 3.1$ GHz show close agreement in UC S-curves and magnitude responses, but phase deviations and errors in sidelobe prediction persist; MM correctly identifies the main beam direction with a slight angular offset, while missing sidelobe details. Computationally, MM is far faster than the FW whole-panel simulation. The paper also documents practical FW solver considerations (such as adaptive mesh refinement to guarantee convergence and its effect on the predicted patterns). The takeaway is that Macromodeling offers an efficient, EM-compliant surrogate model for rapid design and initial analysis of large RIS/H-MIMO panels, but care needs to be taken in interpreting its results for the application areas where high-accuracy sidelobe predictions are a matter of concern.

M.G.A. contributed to the conceptual development of the study, designed the methodology, performed the simulations, curated the data, and wrote the manuscript. R.M. contributed to the conceptualization of the study, participated in shaping the methodology, and provided supervisory guidance. F.M. assisted with part of the simulations and presented the results in the conference venue. T.S. secured the funding that supported this study and supervised the research activity. All authors reviewed and revised the manuscript.

5.5 Paper E

Morteza Ghaderi Aram, Tommy Svensson, Fitim Maxharraj, Rob Maaskant
DDM-Based Accurate and Efficient RIS Modeling for Over-the-Air Mutual Coupling Analysis and Comparison vs Macromodeling
Invited Paper to a Special Section of the *IEEE Open Journal of Antennas and Propagation*, 2026, © IEEE.

Paper E introduces a hybrid domain-decomposition method (H-DDM) tailored for accurate and efficient modeling of open-cavity-based RIS panels and compares it against Macromodeling (MM), element-in-array-pattern (EIAP), and CST full wave reference simulations. The method decomposes each meta-atom into interior and exterior subproblems, enforces field continuity via MFIE/EFIE formulations, and assembles a generalized admittance system; interior admittances are obtained from CST plane-wave characterizations and interfaced with the MoM-based exterior solver (CST-MoM-DDM hybridization). The paper applies H-DDM to Varactor-tunable, open-cavity unit cells and to beamformed panels of sizes 4×4, 4×8, and 4×16 designed to reflect a normal incident plane wave to $+30°$. Numerical results show H-DDM closely matches CST full-wave IE solver solutions, while MM and single-element EIAP correctly predict main beam direction but increasingly deviate in predicting the sidelobe regions: EIAP errors stem from neglecting over-the-air coupling, MM errors from the local-periodicity/PBC and pattern-multiplication assumptions. Practical solver issues are documented, and a quantitative error metric confirms H-DDM's superior fidelity. The paper concludes that H-DDM offers a computationally efficient, high-fidelity tool for RIS analysis of this open-cavity-based family, with future work aimed at further reducing memory/runtime via translational symmetry and low-rank acceleration techniques.

M.G.A. contributed to the conceptual development of the study, participated in shaping the methodology, performed the simulations, extended the comparative study to include other methods from the literature, curated the data, and wrote the manuscript. R.M. conceptualized the study, designed the methodology, participated in simulation setups, assisted in manuscript writing, and supervised the study. F.M. participated in shaping the methodology and assisted with the simulations and manuscript writing. T.S. secured the funding that supported this study and provided supervisory guidance. All authors reviewed and revised the manuscript.

CHAPTER 6

Concluding Remarks and Future Work

Electromagnetic phenomena and the behavior of EM waves as they propagate and interact with biological and engineered materials continue to inspire scientific inquiry, offering far-reaching opportunities across disciplines ranging from life sciences to modern telecommunications. Within this broad landscape, the present thesis has explored advanced EM modeling along two application tracks: Bio-Electromagnetics (BioEM) and surface Electromagnetics (SEM).

The BioEM part examined several aspects of microwave hyperthermia, spanning from antenna and applicator design to full treatment-planning workflows. A new antenna model was introduced and its performance evaluations demonstrated strong potential for use in both phased-array and superficial HT applicators, although its MR compatibility remains an open topic for future investigation. Building on this design, a 16-element elliptical phased-array applicator was proposed and assessed using two realistic head-and-neck patient models. The antenna characteristics and treatment quality metrics were consistently promising, motivating further refinement and eventual clinical translation of the applicator.

The SEM part reviewed state-of-the-art RIS modeling techniques and compared several beamforming approaches commonly used in the communica-

tion society. A unit-cell design from the literature was selected and refined into an open-cavity configuration to serve as the building block for the beamforming panels considered in this work. To address the need for accurate yet computationally efficient EM modeling, a hybrid domain decomposition method (H-DDM) was developed for analyzing over-the-air mutual coupling in this specific class of panels. In the absence of measurement data, full-wave simulations from a commercial solver were used as the reference. H-DDM predictions showed close agreement with these full-wave results and demonstrated superior accuracy compared to surrogate models from the literature, not only in identifying the main beam direction but also in correctly locating sidelobes. Overall, the in-house developed platform shows strong potential for future development. It can be further optimized for speed and memory efficiency by incorporating translational symmetry, accelerated matrix-compression techniques, and other numerical enhancements. Such improvements would open the door to the systematic design and synthesis of very large, massive-MIMO-scale beamforming panels within this open-cavity family, paving the way for next-generation holographic and RIS-based architectures.

References

[1] D. K. Cheng et al., *Field and wave electromagnetics*. Pearson Education India, 1989.

[2] C. A. Balanis, *Advanced engineering electromagnetics*. John Wiley & Sons, 2012.

[3] F. Yang and Y. Rahmat-Samii, *Surface electromagnetics: with applications in antenna, microwave, and optical engineering*. Cambridge University Press, 2019.

[4] R. L. Boylestad and L. Nashelsky, *Electronic devices and circuit theory*. Pearson, 2011.

[5] L. N. Dworsky, "Modern transmission line theory and applications," *Wiley*, 1979.

[6] A. Taflove and S. Hagness, "Computational electrodynamics: The finite-difference time-domain method 3rd edn (norwood, ma: Artech house)," *Wiley*, 2005.

[7] *National cancer institute, NIH,* `https://www.cancer.gov/`, Accessed: 2021-07-29.

[8] *American cancer society*, `https://www.cancer.org/`, Accessed: 2021-07-29.

[9] S. B. Field and C. Franconi, *Physics and technology of hyperthermia*. Springer Science & Business Media, 2012, vol. 127.

[10] W. H. Organization et al., *The global burden of disease: 2004 update*. World Health Organization, 2008.

[11] J. Ferlay, H.-R. Shin, F. Bray, D. Forman, C. Mathers, and D. M. Parkin, "Estimates of worldwide burden of cancer in 2008: Globocan 2008," *International journal of cancer*, vol. 127, no. 12, pp. 2893–2917, 2010.

[12] A. K. Chaturvedi et al., "Worldwide trends in incidence rates for oral cavity and oropharyngeal cancers," *Journal of clinical oncology*, vol. 31, no. 36, p. 4550, 2013.

[13] *Global cancer observatory*, `https://gco.iarc.fr/`, Accessed: 2021-08-1.

[14] H. Sung et al., "Global cancer statistics 2020: Globocan estimates of incidence and mortality worldwide for 36 cancers in 185 countries," *CA: a cancer journal for clinicians*, vol. 71, no. 3, pp. 209–249, 2021.

[15] *The swedish head and neck cancer register (swehncr)*, `https://www.cancercentrum.se/samverkan/`, Accessed: 2021-07-29.

[16] D. W. Ellison, "Childhood medulloblastoma: Novel approaches to the classification of a heterogeneous disease," *Acta neuropathologica*, vol. 120, no. 3, pp. 305–316, 2010.

[17] D. N. Korones, "Treatment of newly diagnosed diffuse brain stem gliomas in children: In search of the holy grail," *Expert review of anticancer therapy*, vol. 7, no. 5, pp. 663–674, 2007.

[18] S. Uday et al., "Endocrine sequelae beyond 10 years in survivors of medulloblastoma," *Clinical endocrinology*, vol. 83, no. 5, pp. 663–670, 2015.

[19] R. L. Mulder et al., "Prevalence and risk factors of radiation-induced growth hormone deficiency in childhood cancer survivors: A systematic review," *Cancer treatment reviews*, vol. 35, no. 7, pp. 616–632, 2009.

[20] P. K. Duffner, "Long-term effects of radiation therapy on cognitive and endocrine function in children with leukemia and brain tumors," *The neurologist*, vol. 10, no. 6, pp. 293–310, 2004.

[21] J. C. Peeken, P. Vaupel, and S. E. Combs, "Integrating hyperthermia into modern radiation oncology: What evidence is necessary?" *Frontiers in oncology*, vol. 7, p. 132, 2017.

[22] P. B. Elming et al., "Hyperthermia: The optimal treatment to overcome radiation resistant hypoxia," *Cancers*, vol. 11, no. 1, p. 60, 2019.

[23] M. W. Dewhirst and T. W. Secomb, "Transport of drugs from blood vessels to tumour tissue," *Nature Reviews Cancer*, vol. 17, no. 12, pp. 738–750, 2017.

[24] B. F. Jordan and P. Sonveaux, "Targeting tumor perfusion and oxygenation to improve the outcome of anticancer therapy1," *Frontiers in pharmacology*, vol. 3, p. 94, 2012.

[25] A. Oei et al., "Molecular and biological rationale of hyperthermia as radio-and chemosensitizer," *Advanced drug delivery reviews*, vol. 163, pp. 84–97, 2020.

[26] H. H. Kampinga, "Cell biological effects of hyperthermia alone or combined with radiation or drugs: A short introduction to newcomers in the field," *International journal of hyperthermia*, vol. 22, no. 3, pp. 191–196, 2006.

[27] N. Datta et al., "Local hyperthermia combined with radiotherapy and-/or chemotherapy: Recent advances and promises for the future," *Cancer treatment reviews*, vol. 41, no. 9, pp. 742–753, 2015.

[28] H. Kok and J. Crezee, "Hyperthermia treatment planning: Clinical application and ongoing developments," *IEEE Journal of Electromagnetics, RF and Microwaves in Medicine and Biology*, 2020.

[29] J. van der Zee, D. González, G. C. van Rhoon, J. D. van Dijk, W. L. van Putten, A. A. Hart, et al., "Comparison of radiotherapy alone with radiotherapy plus hyperthermia in locally advanced pelvic tumours: A prospective, randomised, multicentre trial," *The Lancet*, vol. 355, no. 9210, pp. 1119–1125, 2000.

[30] R. Colombo, A. Salonia, Z. Leib, M. Pavone-Macaluso, and D. Engelstein, "Long-term outcomes of a randomized controlled trial comparing thermochemotherapy with mitomycin-c alone as adjuvant treatment for non-muscle-invasive bladder cancer (nmibc)," *BJU International-British Journal of Urology*, vol. 107, no. 6, p. 912, 2011.

[31] N. G. Huilgol, S. Gupta, C. Sridhar, et al., "Hyperthermia with radiation in the treatment of locally advanced head and neck cancer: A report of randomized trial," *Journal of cancer research and therapeutics*, vol. 6, no. 4, p. 492, 2010.

[32] I. C. H. Group et al., "Radiotherapy with or without hyperthermia in the treatment of superficial localized breast cancer: Results from five randomized controlled trials," *International Journal of Radiation Oncology* Biology* Physics*, vol. 35, no. 4, pp. 731–744, 1996.

[33] J. Overgaard et al., "Randomised trial of hyperthermia as adjuvant to radiotherapy for recurrent or metastatic malignant melanoma," *The Lancet*, vol. 345, no. 8949, pp. 540–543, 1995.

[34] P. Turner, A. Tumeh, and T. Schaefermeyer, "Bsd-2000 approach for deep local and regional hyperthermia: Physics and technology.," *Strahlentherapie und Onkologie: Organ der Deutschen Rontgengesellschaft...[et al]*, vol. 165, no. 10, pp. 738–741, 1989.

[35] M. Paulides et al., "The hypercollar: A novel applicator for hyperthermia in the head and neck," *International Journal of Hyperthermia*, vol. 23, no. 7, pp. 567–576, 2007.

[36] J. Jagannathan et al., "High-intensity focused ultrasound surgery of the brain: Part 1—a historical perspective with modern applications," *Neurosurgery*, vol. 64, no. 2, pp. 201–211, 2009.

[37] G. R. Giammalva et al., "Focused ultrasound in neuroscience. state of the art and future perspectives," *Brain sciences*, vol. 11, no. 1, p. 84, 2021.

[38] B. Behnia, M. Suthar, and A. Webb, "Closed-loop feedback control of phased-array microwave heating using thermal measurements from magnetic resonance imaging," *Concepts in Magnetic Resonance: An Educational Journal*, vol. 15, no. 1, pp. 101–110, 2002.

[39] D. R. Jackson, C. Caloz, and T. Itoh, "Leaky-wave antennas," *Proceedings of the IEEE*, vol. 100, no. 7, pp. 2194–2206, 2012.

[40] A. H. Abdelrahman, F. Yang, A. Z. Elsherbeni, P. Nayeri, and C. A. Balanis, "Analysis and design of transmitarray antennas," 2017.

[41] M. Veysi, C. Guclu, F. Capolino, and Y. Rahmat-Samii, "11 orbital angular momentum beam generation using textured surfaces," *Surface Electromagnetics: With Applications in Antenna, Microwave, and Optical Engineering*, p. 363, 2019.

[42] A. Alù and N. Engheta, "Multifrequency optical invisibility cloak with layered plasmonic shells," *Physical review letters*, vol. 100, no. 11, p. 113 901, 2008.

[43] N. Yu et al., "Light propagation with phase discontinuities: Generalized laws of reflection and refraction," *science*, vol. 334, no. 6054, pp. 333–337, 2011.

[44] B. A. Munk, *Frequency selective surfaces: theory and design*. John Wiley & Sons, 2005.

[45] P.-S. Kildal et al., "Artificially soft and hard surfaces in electromagnetics," *IEEE Transactions on Antennas and Propagation*, vol. 38, no. 10, pp. 1537–1544, 1990.

[46] D. Sievenpiper, L. Zhang, R. F. Broas, N. G. Alexopolous, and E. Yablonovitch, "High-impedance electromagnetic surfaces with a forbidden frequency band," *IEEE Transactions on Microwave Theory and techniques*, vol. 47, no. 11, pp. 2059–2074, 1999.

[47] P. Nayeri, F. Yang, and A. Z. Elsherbeni, "Reflectarray antennas: Theory, designs, and applications," 2018.

[48] N. Engheta and R. W. Ziolkowski, *Metamaterials: physics and engineering explorations*. John Wiley & Sons, 2006.

[49] T. Gong et al., "Holographic mimo communications: Theoretical foundations, enabling technologies, and future directions," *IEEE Communications Surveys & Tutorials*, vol. 26, no. 1, pp. 196–257, 2023.

[50] R. Singh, J. An, A. Kaushik, C. Yuen, A. Zhang, and O. A. Dobre, "Redefining electromagnetic signal and information theory with programmable surfaces: Open critical questions and future horizon," *Authorea Preprints*, 2025.

[51] S. Gabriel, R. Lau, and C. Gabriel, "The dielectric properties of biological tissues: Iii. parametric models for the dielectric spectrum of tissues," *Physics in medicine & biology*, vol. 41, no. 11, p. 2271, 1996.

[52] E. H. Wissler, "Pennes' 1948 paper revisited," *Journal of applied physiology*, vol. 85, no. 1, pp. 35–41, 1998.

[53] J. W. Hand, K. Hynynen, P. Shrivastava, and T. Saylor, *Methods of external hyperthermic heating*. Springer Science & Business Media, 2012.

[54] J. F. Bakker, M. M. Paulides, A. Westra, H. Schippers, and G. Van Rhoon, "Design and test of a 434 mhz multi-channel amplifier system for targeted hyperthermia applicators," *International journal of hyperthermia*, vol. 26, no. 2, pp. 158–170, 2010.

[55] H. Han et al., "Design, implementation, evaluation and application of a 32-channel radio frequency signal generator for thermal magnetic resonance based anti-cancer treatment," *Cancers*, vol. 12, no. 7, p. 1720, 2020.

[56] E. Oberacker et al., "Radiofrequency applicator concepts for thermal magnetic resonance of brain tumors at 297 mhz (7.0 tesla)," *International Journal of Hyperthermia*, vol. 37, no. 1, pp. 549–563, 2020.

[57] E. Oberacker et al., "Patient-specific planning for thermal magnetic resonance of glioblastoma multiforme," *Cancers*, vol. 13, no. 8, p. 1867, 2021.

[58] I. VilasBoas-Ribeiro, S. Curto, G. C. van Rhoon, M. Franckena, and M. M. Paulides, "Mr thermometry accuracy and prospective imaging-based patient selection in mr-guided hyperthermia treatment for locally advanced cervical cancer," *Cancers*, vol. 13, no. 14, p. 3503, 2021.

[59] M. Paulides, H. D. Trefna, S. Curto, and D. Rodrigues, "Recent technological advancements in radiofrequency-andmicrowave-mediated hyperthermia for enhancing drug delivery," *Advanced drug delivery reviews*, vol. 163, pp. 3–18, 2020.

[60] G. Cappiello, "Towards improved treatment planning for head and neck microwave hyperthermia," Ph.D. dissertation, NUI Galway, 2019.

[61] G. Van Rhoon, P. Rietveld, and J. Van der Zee, "A 433 mhz lucite cone waveguide applicator for superficial hyperthermia," *International journal of hyperthermia*, vol. 14, no. 1, pp. 13–27, 1998.

[62] M. de Bruijne, J. Van der Zee, A. Ameziane, and G. C. Van Rhoon, "Quality control of superficial hyperthermia by treatment evaluation," *International Journal of Hyperthermia*, vol. 27, no. 3, pp. 199–213, 2011.

[63] S. Jacobsen, P. R. Stauffer, and D. G. Neuman, "Dual-mode antenna design for microwave heating and noninvasive thermometry of superficial tissue disease," *IEEE Transactions on Biomedical Engineering*, vol. 47, no. 11, pp. 1500–1509, 2000.

[64] P. Wust et al., "Hyperthermia in combined treatment of cancer," *The lancet oncology*, vol. 3, no. 8, pp. 487–497, 2002.

[65] P. Rietveld, M. Lumori, J. van der Zee, and G. Van Rhoon, "Quantitative evaluation of arrays of lucite cone applicators in flat layered phantoms using gaussian-beam-predicted and thermographically measured sar distributions," *Physics in Medicine & Biology*, vol. 43, no. 8, p. 2207, 1998.

[66] P. R. Stauffer et al., "Conformal microwave array (cma) applicators for hyperthermia of diffuse chest wall recurrence," *International Journal of Hyperthermia*, vol. 26, no. 7, pp. 686–698, 2010.

[67] E. A. Gelvich and V. N. Mazokhin, "Contact flexible microstrip applicators (cfma) in a range from microwaves up to short waves," *IEEE Transactions on Biomedical Engineering*, vol. 49, no. 9, pp. 1015–1023, 2002.

[68] H. P. Kok et al., "Fdtd simulations to assess the performance of cfma-434 applicators for superficial hyperthermia," *International Journal of Hyperthermia*, vol. 25, no. 6, pp. 462–476, 2009.

[69] J. Johnson, D. Neuman, P. Maccarini, T. Juang, P. Stauffer, and P. Turner, "Evaluation of a dual-arm archimedean spiral array for microwave hyperthermia," *International Journal of Hyperthermia*, vol. 22, no. 6, pp. 475–490, 2006.

[70] N. R. Datta et al., "Hyperthermia and reirradiation for locoregional recurrences in preirradiated breast cancers: A single institutional experience," *Swiss medical weekly*, vol. 145, w14133, 2015.

[71] J. Crezee et al., "Development of a 70 mhz unit for hyperthermia treatment of deep-seated breast tumors," *International Journal of Microwave and Wireless Technologies*, vol. 9, no. 6, pp. 1317–1324, 2017.

[72] J. Crezee et al., "Improving locoregional hyperthermia delivery using the 3-d controlled amc-8 phased array hyperthermia system: A preclinical study," *International Journal of Hyperthermia*, vol. 25, no. 7, pp. 581–592, 2009.

[73] A. A. De Leeuw and J. J. Lagendijk, "Design of a clinical deep-body hyperthermia system based on the 'coaxial tem'applicator," *International journal of hyperthermia*, vol. 3, no. 5, pp. 413–421, 1987.

[74] P. Raskmark, S. N. Hornsleth, L. N. Salling, J. C. Lindegaard, and J. Overgaard, "Deep heating using a movable applicator phased array hyperthermia system: A preclinical feasibility study," *Acta Oncologica*, vol. 33, no. 4, pp. 451–455, 1994.

[75] P. Togni et al., "Electromagnetic redesign of the hypercollar applicator: Toward improved deep local head-and-neck hyperthermia," *Physics in Medicine & Biology*, vol. 58, no. 17, p. 5997, 2013.

[76] M. M. Paulides et al., "Simulation techniques in hyperthermia treatment planning," *International Journal of Hyperthermia*, vol. 29, no. 4, pp. 346–357, 2013.

[77] H. Kok, P. Wust, P. R. Stauffer, F. Bardati, G. Van Rhoon, and J. Crezee, "Current state of the art of regional hyperthermia treatment planning: A review," *Radiation Oncology*, vol. 10, no. 1, pp. 1–14, 2015.

[78] M. Paulides et al., "Clinical introduction of novel microwave hyperthermia technology: The hypercollar3d applicator for head and neck hyperthermia," in *2015 9th European Conference on Antennas and Propagation (EuCAP)*, IEEE, 2015, pp. 1–4.

[79] P. Takook, M. Shafiemehr, M. Persson, and H. D. Trefná, "Experimental evaluation of uwb applicator prototype for head and neck hyperthermia," in *2017 11th European Conference on Antennas and Propagation (EUCAP)*, IEEE, 2017, pp. 3619–3620.

[80] M. Paulides et al., "The clinical feasibility of deep hyperthermia treatment in the head and neck: New challenges for positioning and temperature measurement," *Physics in Medicine & Biology*, vol. 55, no. 9, p. 2465, 2010.

[81] Z. Rijnen, P. Togni, R. Roskam, S. G. Van De Geer, R. H. Goossens, and M. M. Paulides, "Quality and comfort in head and neck hyperthermia: A redesign according to clinical experience and simulation studies," *International Journal of Hyperthermia*, vol. 31, no. 8, pp. 823–830, 2015.

[82] P. Takook, M. Persson, J. Gellermann, and H. D. Trefná, "Compact self-grounded bow-tie antenna design for an uwb phased-array hyperthermia applicator," *International Journal of Hyperthermia*, vol. 33, no. 4, pp. 387–400, 2017.

[83] S. Curto, "Antenna development for radio frequency hyperthermia applications," 2010.

[84] C. H. Durney and M. F. Iskander, "Antennas for medical applications," in *Antenna Handbook*, Springer, 1993, pp. 596–654.

[85] M. M. Paulides, J. F. Bakker, N. Chavannes, and G. C. Van Rhoon, "A patch antenna design for application in a phased-array head and neck hyperthermia applicator," *IEEE Transactions on Biomedical Engineering*, vol. 54, no. 11, pp. 2057–2063, 2007.

[86] L. Winter et al., "Design and evaluation of a hybrid radiofrequency applicator for magnetic resonance imaging and rf induced hyperthermia: Electromagnetic field simulations up to 14.0 tesla and proof-of-concept at 7.0 tesla," *PloS one*, vol. 8, no. 4, e61661, 2013.

[87] M. Paulides et al., "A printed yagi–uda antenna for application in magnetic resonance thermometry guided microwave hyperthermia applicators," *Physics in Medicine & Biology*, vol. 62, no. 5, p. 1831, 2017.

[88] P. Turner, A. Tumeh, and T. Schaefermeyer, "Bsd-2000 approach for deep local and regional hyperthermia: Physics and technology.," *Strahlentherapie und Onkologie: Organ der Deutschen Rontgengesellschaft...[et al]*, vol. 165, no. 10, pp. 738–741, 1989.

[89] D. Fatehi and G. C. Van Rhoon, "Sar characteristics of the sigma-60-ellipse applicator," *International journal of hyperthermia*, vol. 24, no. 4, pp. 347–356, 2008.

[90] R. Zweije, H. P. Kok, A. Bakker, A. Bel, and J. Crezee, "Technical and clinical evaluation of the alba-4d 70mhz loco-regional hyperthermia system," in *2018 48th European Microwave Conference (EuMC)*, IEEE, 2018, pp. 328–331.

[91] J. Yang and A. Kishk, "A novel low-profile compact directional ultra-wideband antenna: The self-grounded bow-tie antenna," *IEEE Transactions on Antennas and Propagation*, vol. 60, no. 3, pp. 1214–1220, 2011.

[92] A. Kazemipour and X. Begaud, "Calculable dipole antenna for emc measurements with low-loss wide-band balun from 30 mhz to 2 ghz," *Electromagnetics*, vol. 25, no. 3, pp. 187–202, 2005.

[93] R. E. Collin, *Field theory of guided waves*. John Wiley & Sons, 1990, vol. 5.

[94] S. B. Cohn, "Properties of ridge wave guide," *Proceedings of the IRE*, vol. 35, no. 8, pp. 783–788, 1947.

[95] S. Hopfer, "The design of ridged waveguides," *IRE Transactions on Microwave Theory and Techniques*, vol. 3, no. 5, pp. 20–29, 1955.

[96] W. Sun and C. A. Balanis, "Mfie analysis and design of ridged waveguides," *IEEE Transactions on Microwave theory and Techniques*, vol. 41, no. 11, pp. 1965–1971, 1993.

[97] D. O. Rodriguez-Duarte, J. A. T. Vasquez, R. Scapaticci, L. Crocco, and F. Vipiana, "Brick-shaped antenna module for microwave brain imaging systems," *IEEE Antennas and Wireless Propagation Letters*, vol. 19, no. 12, pp. 2057–2061, 2020.

[98] A. R. Mallahzadeh and A. Imani, "Double-ridged antenna for wideband applications," *Progress In Electromagnetics Research*, vol. 91, pp. 273–285, 2009.

[99] H. D. Trefná et al., "Quality assurance guidelines for superficial hyperthermia clinical trials," *Strahlentherapie und Onkologie*, vol. 193, no. 5, pp. 351–366, 2017.

[100] H. D. Trefná et al., "Quality assurance guidelines for superficial hyperthermia clinical trials: I. clinical requirements," *International Journal of Hyperthermia*, vol. 33, no. 4, pp. 471–482, 2017.

[101] H. D. Trefná and A. Ström, "Hydrogels as a water bolus during hyperthermia treatment," *Physics in Medicine & Biology*, vol. 64, no. 11, p. 115 025, 2019.

[102] J. Lee and S. Nam, "Effective area of a receiving antenna in a lossy medium," *IEEE transactions on antennas and propagation*, vol. 57, no. 6, pp. 1843–1845, 2009.

[103] S. M. Aguilar, M. A. Al-Joumayly, M. J. Burfeindt, N. Behdad, and S. C. Hagness, "Multiband miniaturized patch antennas for a compact, shielded microwave breast imaging array," *IEEE transactions on antennas and propagation*, vol. 62, no. 3, pp. 1221–1231, 2013.

[104] G. Bruggmoser et al., "Guideline for the clinical application, documentation and analysis of clinical studies for regional deep hyperthermia," *Strahlentherapie und Onkologie*, vol. 188, no. 2, pp. 198–211, 2012.

[105] M. M. Paulides, S. H. Vossen, A. P. Zwamborn, and G. C. van Rhoon, "Theoretical investigation into the feasibility to deposit rf energy centrally in the head-and-neck region," *International Journal of Radiation Oncology* Biology* Physics*, vol. 63, no. 2, pp. 634–642, 2005.

[106] *Tissue properties database. v3.1. 2016*, `http://itis.swiss/virtual-population/tissue-properties/downloads-v3-1/`, Accessed: 2021-07-29.

[107] A. Christ et al., "The virtual family—development of surface-based anatomical models of two adults and two children for dosimetric simulations," *Physics in Medicine & Biology*, vol. 55, no. 2, N23, 2009.

[108] M.-C. Gosselin et al., "Development of a new generation of high-resolution anatomical models for medical device evaluation: The virtual population 3.0," *Physics in Medicine & Biology*, vol. 59, no. 18, p. 5287, 2014.

[109] S. N. Makarov et al., "Virtual human models for electromagnetic studies and their applications," *IEEE reviews in biomedical engineering*, vol. 10, pp. 95–121, 2017.

[110] T. Rylander, P. Ingelström, and A. Bondeson, *Computational electromagnetics*. Springer Science & Business Media, 2012.

[111] K. Yee, "Numerical solution of initial boundary value problems involving maxwell's equations in isotropic media," *IEEE Transactions on antennas and propagation*, vol. 14, no. 3, pp. 302–307, 1966.

[112] M. Clemens and T. Weiland, "Discrete electromagnetism with the finite integration technique," *Progress In Electromagnetics Research*, vol. 32, pp. 65–87, 2001.

[113] T. Weiland, M. Timm, and I. Munteanu, "A practical guide to 3-d simulation," *IEEE Microwave Magazine*, vol. 9, no. 6, pp. 62–75, 2008.

[114] M. Kozlov and R. Turner, "A comparison of ansoft hfss and cst microwave studio simulation software for multi-channel coil design and sar estimation at 7t mri," *Piers online*, vol. 6, no. 4, pp. 395–399, 2010.

[115] V. Dolean, H. Fahs, L. Fezoui, and S. Lanteri, "Locally implicit discontinuous galerkin method for time domain electromagnetics," *Journal of Computational Physics*, vol. 229, no. 2, pp. 512–526, 2010.

[116] H. Kok, P. Van Haaren, J. Van de Kamer, J. Wiersma, J. Van Dijk, and J. Crezee, "High-resolution temperature-based optimization for hyperthermia treatment planning," *Physics in Medicine & Biology*, vol. 50, no. 13, p. 3127, 2005.

[117] R. Canters, M. Paulides, M. Franckena, J. Mens, and G. Van Rhoon, *Benefit of replacing the sigma-60 by the sigma-eye applicator*, 2013.

[118] H. K. Lee et al., "Superficial hyperthermia and irradiation for recurrent breast carcinoma of the chest wall: Prognostic factors in 196 tumors.," *International journal of radiation oncology, biology, physics*, vol. 40, no. 2, pp. 365–375, 1998.

[119] T. Köhler, P. Maass, P. Wust, and M. Seebass, "A fast algorithm to find optimal controls of multiantenna applicators in regional hyperthermia," *Physics in Medicine & Biology*, vol. 46, no. 9, p. 2503, 2001.

[120] H. D. Trefná, J. Vrba, and M. Persson, "Time-reversal focusing in microwave hyperthermia for deep-seated tumors," *Physics in Medicine & Biology*, vol. 55, no. 8, p. 2167, 2010.

[121] P. T. Nguyen, A. M. Abbosh, and S. Crozier, "3-d focused microwave hyperthermia for breast cancer treatment with experimental validation," *IEEE Transactions on Antennas and Propagation*, vol. 65, no. 7, pp. 3489–3500, 2017.

[122] D. A. Iero, T. Isernia, A. F. Morabito, I. Catapano, and L. Crocco, "Optimal constrained field focusing for hyperthermia cancer therapy: A feasibility assessment on realistic phantoms," *Progress In Electromagnetics Research*, vol. 102, pp. 125–141, 2010.

[123] G. G. Bellizzi, T. Drizdal, G. C. van Rhoon, L. Crocco, T. Isernia, and M. M. Paulides, "The potential of constrained sar focusing for hyperthermia treatment planning: Analysis for the head & neck region," *Physics in Medicine & Biology*, vol. 64, no. 1, p. 015 013, 2018.

[124] A. Kuehne, E. Oberacker, H. Waiczies, and T. Niendorf, "Solving the time-and frequency-multiplexed problem of constrained radiofrequency induced hyperthermia," *Cancers*, vol. 12, no. 5, p. 1072, 2020.

[125] Z. Rijnen et al., "Clinical integration of software tool vedo for adaptive and quantitative application of phased array hyperthermia in the head and neck," *International journal of Hyperthermia*, vol. 29, no. 3, pp. 181–193, 2013.

[126] J. Robinson and Y. Rahmat-Samii, "Particle swarm optimization in electromagnetics," *IEEE transactions on antennas and propagation*, vol. 52, no. 2, pp. 397–407, 2004.

[127] H. H. Pennes, "Analysis of tissue and arterial blood temperatures in the resting human forearm," *Journal of applied physiology*, vol. 1, no. 2, pp. 93–122, 1948.

[128] C. A. Van den Berg et al., "Towards patient specific thermal modelling of the prostate," *Physics in Medicine & Biology*, vol. 51, no. 4, p. 809, 2006.

[129] H. P. Kok, J. Gellermann, C. A. Van Den Berg, P. R. Stauffer, J. W. Hand, and J. Crezee, "Thermal modelling using discrete vasculature for thermal therapy: A review," *international Journal of Hyperthermia*, vol. 29, no. 4, pp. 336–345, 2013.

[130] H. Gothäll, "How to use interpolated material data to model irregular geometries," *Comsol Blog*, 2018.

[131] R. Gaffoglio, G. Vecchi, M. Righero, G. Giordanengo, and M. Zucchi, "Impact of different modeling approaches in field focusing predictions of hyperthermia cancer therapy," *Skin (wet)*, vol. 1109, pp. 0–681,

[132] M. G. Aram, "Differential least-square microwave thermometry: A feasibility study on a realistic patient model," *Technical Report*, 2023.

[133] M. Alnæs et al., "The fenics project version 1.5," *Archive of Numerical Software*, vol. 3, no. 100, 2015.

[134] J.-M. Jin, *The finite element method in electromagnetics*. John Wiley & Sons, 2015.

[135] H. P. Langtangen and K.-A. Mardal, *Introduction to numerical methods for variational problems*. Springer Nature, 2019, vol. 21.

[136] H. P. Langtangen and A. Logg, *Solving PDEs in python: the FEniCS tutorial I*. Springer Nature, 2017.

[137] V. Asadchy, A. Díaz-Rubio, D. H. Kwon, and S. Tretyakov, "Analytical modeling of electromagnetic surfaces," in *Surface Electromagnetics: With Applications in Antenna, Microwave, and Optical Engineering*, Cambridge University Press, 2019, pp. 30–65.

[138] K. Achouri, Y. Vahabzadeh, and C. Caloz, "4 electromagnetic metasurface synthesis, analysis, and applications," *Surface Electromagnetics: With Applications in Antenna, Microwave, and Optical Engineering*, p. 124, 2019.

[139] M. Idemen, "Straightforward derivation of boundary conditions on sheet simulating an anisotropic thin layer," *Electronics Letters*, vol. 24, no. 11, pp. 663–665, 1988.

[140] E. F. Kuester, M. A. Mohamed, M. Piket-May, and C. L. Holloway, "Averaged transition conditions for electromagnetic fields at a metafilm," *IEEE Transactions on Antennas and Propagation*, vol. 51, no. 10, pp. 2641–2651, 2003.

[141] O. Luukkonen et al., "Simple and accurate analytical model of planar grids and high-impedance surfaces comprising metal strips or patches," *IEEE transactions on antennas and propagation*, vol. 56, no. 6, pp. 1624–1632, 2008.

[142] F. Costa, "A simple effective permittivity model for metasurfaces within multilayer stratified media," *IEEE Transactions on Antennas and Propagation*, vol. 69, no. 8, pp. 5148–5153, 2021.

[143] F. Costa and M. Borgese, "Electromagnetic model of reflective intelligent surfaces," *IEEE Open Journal of the Communications Society*, vol. 2, pp. 1577–1589, 2021.

[144] B. E. Saleh and M. C. Teich, *Fundamentals of photonics, 2 volume set*. john Wiley & sons, 2019.

[145] S. V. Hum and J. Perruisseau-Carrier, "Reconfigurable reflectarrays and array lenses for dynamic antenna beam control: A review," *IEEE transactions on antennas and propagation*, vol. 62, no. 1, pp. 183–198, 2013.

[146] D. Ramaccia et al., "Reconfigurability in electromagnetic metasurfaces and metamaterials for antenna systems: State-of-the-art technical approaches, limitations, and applications.[electromagnetic metamaterials]," *IEEE Antennas and Propagation Magazine*, vol. 67, no. 4, pp. 42–54, 2025.

[147] L. Zhang et al., "Space-time-coding digital metasurfaces," *Nature communications*, vol. 9, no. 1, p. 4334, 2018.

[148] S. Taravati and A. A. Kishk, "Space-time modulation: Principles and applications," *IEEE microwave magazine*, vol. 21, no. 4, pp. 30–56, 2020.

[149] M. Rossanese, P. Mursia, A. Garcia-Saavedra, V. Sciancalepore, A. Asadi, and X. Costa-Perez, "Designing, building, and characterizing rf switch-based reconfigurable intelligent surfaces," in *Proceedings of the 16th ACM Workshop on Wireless Network Testbeds, Experimental evaluation & CHaracterization*, 2022, pp. 69–76.

[150] M. Rossanese, "A study on reconfigurable intelligent surface technology," *PhD Thesis*, 2024.

[151] Y. Zeng and R. Zhang, "Millimeter wave mimo with lens antenna array: A new path division multiplexing paradigm," *IEEE Transactions on Communications*, vol. 64, no. 4, pp. 1557–1571, 2016.

[152] E. Björnson, L. Sanguinetti, H. Wymeersch, J. Hoydis, and T. L. Marzetta, "Massive mimo is a reality—what is next?: Five promising research directions for antenna arrays," *Digital Signal Processing*, vol. 94, pp. 3–20, 2019.

[153] I. F. Akyildiz, C. Han, and S. Nie, "Combating the distance problem in the millimeter wave and terahertz frequency bands," *IEEE Communications Magazine*, vol. 56, no. 6, pp. 102–108, 2018.

[154] C. Han, J. M. Jornet, and I. Akyildiz, "Ultra-massive mimo channel modeling for graphene-enabled terahertz-band communications," in *2018 IEEE 87th vehicular technology conference (VTC Spring)*, IEEE, 2018, pp. 1–5.

[155] E. Björnson, F. Kara, N. Kolomvakis, A. Kosasih, P. Ramezani, and M. B. Salman, "Enabling 6g performance in the upper mid-band by transitioning from massive to gigantic mimo," *IEEE Open Journal of the Communications Society*, 2025.

[156] Z. Zhang et al., "6g wireless networks: Vision, requirements, architecture, and key technologies," *IEEE vehicular technology magazine*, vol. 14, no. 3, pp. 28–41, 2019.

[157] A. Araghi et al., "Reconfigurable intelligent surface (ris) in the sub-6 ghz band: Design, implementation, and real-world demonstration," *IEEE Access*, vol. 10, pp. 2646–2655, 2022.

[158] Q. Ma, Q. Xiao, Q. R. Hong, X. Gao, V. Galdi, and T. J. Cui, "Digital coding metasurfaces: From theory to applications," *IEEE Antennas and Propagation Magazine*, vol. 64, no. 4, pp. 96–109, 2022.

[159] T. J. Cui et al., "Information metamaterial systems," *Iscience*, vol. 23, no. 8, 2020.

[160] M. Khalily, O. Yurduseven, T. J. Cui, Y. Hao, and G. V. Eleftheriades, "Engineered electromagnetic metasurfaces in wireless communications: Applications, research frontiers and future directions," *IEEE communications magazine*, vol. 60, no. 10, pp. 88–94, 2022.

[161] P. Nayeri, A. Z. Elsherbeni, and F. Yang, "Radiation analysis approaches for reflectarray antennas [antenna designer's notebook]," *IEEE Antennas and Propagation Magazine*, vol. 55, no. 1, pp. 127–134, 2013.

[162] H. Li and B. Clerckx, "Non-reciprocal beyond diagonal ris: Multi-port network models and performance benefits in full-duplex systems," *IEEE Transactions on Communications*, 2025.

[163] Y. Ma, J. F. Kolb, A. A. Ihalage, A. S. Andy, and Y. Hao, "Incorporating meta-atom interactions in rapid optimization of large-scale disordered metasurfaces based on deep interactive learning," *Advanced Photonics Research*, vol. 4, no. 4, p. 2 200 099, 2023.

[164] Z. Zhang et al., "Macromodeling of reconfigurable intelligent surface based on microwave network theory," *IEEE Transactions on Antennas and Propagation*, vol. 70, no. 10, pp. 8707–8717, 2022.

[165] E. Baladi and S. V. Hum, "Equivalent circuit models for metasurfaces using floquet modal expansion of surface current distributions," *IEEE Transactions on Antennas and Propagation*, vol. 69, no. 9, pp. 5691–5703, 2021.

[166] J. W. Zhang et al., "A novel two-stage optimization framework for designing active metasurfaces based on multiport microwave network theory," *IEEE Transactions on Antennas and Propagation*, vol. 72, no. 2, pp. 1603–1616, 2023.

[167] J. Budhu and A. Grbic, "Aperiodic metasurface synthesis techniques and designs," in *Metamaterials-by-Design*, Elsevier, 2024, pp. 75–114.

[168] M. Almunif, F. Alsolamy, and A. Grbic, "Network-based design of reactive beamforming metasurfaces," *IEEE Transactions on Antennas and Propagation*, 2025.

[169] K. Konno, S. Terranova, Q. Chen, and G. Gradoni, "Generalized impedance model of wireless links assisted by reconfigurable intelligent surfaces," *IEEE Transactions on Antennas and Propagation*, vol. 72, no. 10, pp. 7691–7699, 2024.

[170] J. W. Wallace and M. A. Jensen, "Mutual coupling in mimo wireless systems: A rigorous network theory analysis," *IEEE transactions on wireless communications*, vol. 3, no. 4, pp. 1317–1325, 2004.

[171] B. K. Lau, J. B. Andersen, G. Kristensson, and A. F. Molisch, "Impact of matching network on bandwidth of compact antenna arrays," *IEEE Transactions on Antennas and Propagation*, vol. 54, no. 11, pp. 3225–3238, 2006.

[172] S. Shen, B. Clerckx, and R. Murch, "Modeling and architecture design of reconfigurable intelligent surfaces using scattering parameter network analysis," *IEEE Transactions on Wireless Communications*, vol. 21, no. 2, pp. 1229–1243, 2021.

[173] A. Abrardo, A. Toccafondi, and M. Di Renzo, "Design of reconfigurable intelligent surfaces by using s-parameter multiport network theory–optimization and full-wave validation," *IEEE Transactions on Wireless Communications*, 2024.

[174] D. M. Pozar, *Microwave engineering: theory and techniques*. John wiley & sons, 2021.

[175] C. A. Balanis, *Antenna theory: analysis and design*. John wiley & sons, 2016.

[176] P.-S. Kildal, *Foundations of antenna engineering: a unified approach for line-of-sight and multipath*. Artech House, 2015.

[177] Y. Liu and C. D. Sarris, "Efficient propagation modeling for communication channels with reconfigurable intelligent surfaces," *IEEE Antennas and Wireless Propagation Letters*, vol. 21, no. 10, pp. 2120–2124, 2022.

[178] Y. Liu and C. D. Sarris, "Efficient computation of scattered fields from reconfigurable intelligent surfaces for propagation modeling," *IEEE Transactions on Antennas and Propagation*, vol. 72, no. 2, pp. 1817–1826, 2024.

[179] Z. Yun and M. F. Iskander, "Ray tracing for radio propagation modeling: Principles and applications," *IEEE access*, vol. 3, pp. 1089–1100, 2015.

[180] C. Pan et al., "Multicell mimo communications relying on intelligent reflecting surfaces," *IEEE transactions on wireless communications*, vol. 19, no. 8, pp. 5218–5233, 2020.

[181] H. T. Friis, "A note on a simple transmission formula," *proc. IRE*, vol. 34, no. 5, pp. 254–256, 1946.

[182] W. Tang et al., "Wireless communications with reconfigurable intelligent surface: Path loss modeling and experimental measurement," *IEEE transactions on wireless communications*, vol. 20, no. 1, pp. 421–439, 2020.

[183] Y. Cui, H. Yin, L. Tan, and M. Di Renzo, "A 3d positioning-based channel estimation method for ris-aided mmwave communications," *arXiv preprint arXiv:2203.14636*, 2022.

[184] S. Y. Seidel and T. S. Rappaport, "Site-specific propagation prediction for wireless in-building personal communication system design," *IEEE transactions on Vehicular Technology*, vol. 43, no. 4, pp. 879–891, 1994.

[185] K. Zhao et al., "Channel characteristics and user body effects in an outdoor urban scenario at 15 and 28 ghz," *IEEE Transactions on Antennas and Propagation*, vol. 65, no. 12, pp. 6534–6548, 2017.

[186] M. G. Aram, H. Guo, M. Yin, and T. Svensson, "Site-specific outdoor propagation assessment and ray-tracing analysis for wireless digital twins," in *2025 19th European Conference on Antennas and Propagation (EuCAP)*, IEEE, 2025, pp. 1–5.

[187] L. Hao, S. K. Vuyyuru, S. A. Tretyakov, A. Salihu, M. Rupp, and R. Valkonen, "Modeling ris from electromagnetic principles to communication systems–part ii: System-level simulation, ray tracing, and measurement," *IEEE Transactions on Antennas and Propagation*, 2025.

[188] Z. Liu and S. V. Hum, "Channel-informed ris analysis and optimization using hybrid ray-tracing and full-wave simulation framework," *IEEE Transactions on Antennas and Propagation*, vol. 74, no. 1, pp. 909–921, 2025.

[189] X. Pei et al., "Ris-aided wireless communications: Prototyping, adaptive beamforming, and indoor/outdoor field trials," *IEEE Transactions on Communications*, vol. 69, no. 12, pp. 8627–8640, 2021.

[190] J. An et al., "Codebook-based solutions for reconfigurable intelligent surfaces and their open challenges," *IEEE Wireless Communications*, vol. 31, no. 2, pp. 134–141, 2022.

[191] B. H. Fong, J. S. Colburn, J. J. Ottusch, J. L. Visher, and D. F. Sievenpiper, "Scalar and tensor holographic artificial impedance surfaces," *IEEE transactions on antennas and propagation*, vol. 58, no. 10, pp. 3212–3221, 2010.

[192] A. Araghi, M. Khalily, P. Xiao, and R. Tafazolli, "Holographic-based leaky-wave structures: Transformation of guided waves to leaky waves," *IEEE Microwave Magazine*, vol. 22, no. 6, pp. 49–63, 2021.

[193] Z. R. Omam et al., "Holographic metasurfaces enabling wave computing for 6g: Status overview, challenges, and future research trends," *arXiv preprint arXiv:2501.05173*, 2025.

[194] J. C. Liang et al., "An angle-insensitive 3-bit reconfigurable intelligent surface," *IEEE Transactions on Antennas and Propagation*, vol. 70, no. 10, pp. 8798–8808, 2021.

[195] R. Maaskant and et al., "Domain decomposition analysis of open-cavity-based array elements — roadmap toward analyzing large-scale reflectarrays and reconfigurable intelligent surfaces," in *26th International Conference on Electromagnetics in Advanced Applications (ICEAA)*, IEEE, 2025, pp. 1–6.

[196] G. Huang, J. M. Purushothama, Y. Ding, X. Li, and W. Gong, "Synthesis-free backscatter directional modulation communication using van-atta arrays," *IET Microwaves, Antennas & Propagation*, vol. 16, no. 10, pp. 654–659, 2022.

[197] A. V. Diebold, D. Pande, C. Gregg, and D. R. Smith, "Reflectarray design using a discrete dipole framework," *IEEE Open Journal of Antennas and Propagation*, vol. 4, pp. 216–228, 2023.

[198] T. J. Cui, M. Q. Qi, X. Wan, J. Zhao, and Q. Cheng, "Coding metamaterials, digital metamaterials and programmable metamaterials," *Light: science & applications*, vol. 3, no. 10, e218–e218, 2014.

[199] G. D. Bai et al., "Manipulation of electromagnetic and acoustic wave behaviors via shared digital coding metallic metasurfaces," *Advanced Intelligent Systems*, vol. 1, no. 5, p. 1 900 038, 2019.

[200] L. Li et al., "Electromagnetic reprogrammable coding-metasurface holograms," *Nature communications*, vol. 8, no. 1, p. 197, 2017.

[201] R. W. Shao et al., "Dual-channel near-field holographic mimo communications based on programmable digital coding metasurface and electromagnetic theory," *Nature Communications*, vol. 16, no. 1, p. 915, 2025.

[202] Q. Xiao et al., "Orbital-angular-momentum-encrypted holography based on coding information metasurface," *Advanced Optical Materials*, vol. 9, no. 11, p. 2 002 155, 2021.

[203] D. Berry, R. Malech, and W. Kennedy, "The reflectarray antenna," *IEEE Transactions on Antennas and Propagation*, vol. 11, no. 6, pp. 645–651, 1963.

[204] F. Venneri, G. Angiulli, and G. Di Massa, "Design of microstrip reflect array using data from isolated patch analysis," *Microwave and Optical Technology Letters*, vol. 34, no. 6, pp. 411–414, 2002.

[205] D. Pozar and T. Metzler, "Analysis of a reflectarray antenna using microstrip patches of variable size," *Electronics Letters*, vol. 29, no. 8, pp. 657–658, 1993.

[206] J. A. Encinar, "Design of two-layer printed reflectarrays using patches of variable size," *IEEE Transactions on Antennas and Propagation*, vol. 49, no. 10, pp. 1403–1410, 2002.

[207] R. F. Harrington and J. R. Mautz, "Electromagnetic coupling through apertures by the generalized admittance approach," *Computer physics communications*, vol. 68, no. 1-3, pp. 19–42, 1991.

[208] W. C. Gibson, *The method of moments in electromagnetics*. Chapman and Hall/CRC, 2021.

[209] R. F. Harrington, *Field computation by moment methods*. Wiley-IEEE Press, 1993.

[210] R. Harrington, "Origin and development of the method of moments for field computation," *IEEE Antennas and Propagation Magazine*, vol. 32, no. 3, pp. 31–35, 2002.

[211] J. R. Mosig, "Arbitrarily shaped microstrip structures and their analysis with a mixed potential integral equation," *IEEE Transactions on Microwave theory and Techniques*, vol. 36, no. 2, pp. 314–323, 2002.

[212] S. Rao, D. Wilton, and A. Glisson, "Electromagnetic scattering by surfaces of arbitrary shape," *IEEE Transactions on antennas and propagation*, vol. 30, no. 3, pp. 409–418, 1982.

[213] T. Wang, R. Harrington, and J. Mautz, "Electromagnetic scattering from and transmission through arbitrary apertures in conducting bodies," *IEEE Transactions on Antennas and Propagation*, vol. 38, no. 11, pp. 1805–1814, 1990.

[214] M. Jiang et al., "Efficient and accurate simulations of metamaterials based on domain decomposition and unit feature database," *IEEE Transactions on Antennas and Propagation*, 2024.

[215] J. Shabanpour, X. Wang, S. Kosulnikov, and C. Simovski, "Advancing ris beamforming efficiency: Moving beyond diagonal matrix techniques," *IEEE Transactions on Vehicular Technology*, pp. 1–14, 2025.

[216] J. Tapie, M. Nerini, B. Clerckx, and P. d. Hougne, "Beyond-diagonal ris prototype and performance evaluation," *IEEE Wireless Communications Letters*, vol. 15, pp. 1–5, 2026.

[217] H. Li, B.-Z. Wang, L. Guo, W. Shaoand, and P. Du, "A far field pattern analysis technique for reflectarrays including mutual coupling between elements," *Journal of Electromagnetic Waves and Applications*, vol. 23, no. 1, pp. 87–95, 2009.